Title
Multiferroic Applications of Nanoarchitectured, Solution-Processed Materials

Author
Buditama, Abraham

Publication Date
2017

Peer reviewed|Thesis/dissertation

UNIVERSITY OF CALIFORNIA

Los Angeles

Multiferroic Applications of Nanoarchitectured, Solution-Processed Materials

A dissertation submitted in partial satisfaction

of the requirements for the degree Doctor of Philosophy

in Chemistry

by

Abraham Nataniel Buditama

2017

ABSTRACT OF THE DISSERTATION

Multiferroic Applications of

Nanoarchitectured, Solution-Processed Materials

by

Abraham Nataniel Buditama

Doctor of Philosophy in Chemistry

University of California, Los Angeles, 2017

Prof. Sarah H. Tolbert, Chair

This dissertation compiles work on sol-gel syntheses of multiferroic materials and applications thereof. Multiferroics, or materials that simultaneously exhibit multiple order parameters such as ferromagnetism, ferroelectricity, or ferroelasticity, may be fabricated by solution processing techniques. Specifically, these techniques may be used to control both the atomic and the nanoscale structures of piezoelectric lead zirconate titanate ($PbZr_xTi_{1-x}O_3$ or PZT) and magnetostrictive cobalt ferrite ($CoFe_2O_4$ or CFO).

The first part of this work focuses on strain-coupling PZT and CFO into a magnetoelectric composite. A mesoporous CFO framework was synthesized using block copolymer templating, which was subsequently conformally filled by PZT by atomic layer deposition (ALD). The final porosity of the film is controlled by the ALD PZT layer, and we show that this porosity influences the magnetoelectric coupling of the composite. An *ex situ* external electric field is applied to the composite, and samples with the greatest porosity, and thus greatest mechanical flexibility, were able to accommodate strain transfer to the CFO, resulting in a greater reduction of the sample saturation magnetization.

The second part of this work focuses on using solution processing to control domain-level contributions to the material's ferroic properties. An iterative spin coating process can be used to create PZT films of arbitrary thickness. Electric domains are generally pinned in nanoscale PZT

thin films, but models of PZT films on the mesoscale must consider domain reorientation. As for CFO, solution processing may be used to control the CFO grain size, which in turn limits the size of its magnetic domains, and subsequently its static magnetic properties.

The dissertation of Abraham N. Buditama is approved.

Jeffrey I. Zink

Christopher S. Lynch

Sarah H. Tolbert, Committee Chair

University of California, Los Angeles

2017

Contents

List of Figures

List of Tables

Acknowledgments

Chapter 2 is a version of *Applied Physics Letters* **109**, 112904 (2016), by Diana Chien, Abraham N. Buditama, Laura T. Schelhas, Hye Yeon Kang, Shauna Robbennolt, Jane P. Chang, and Sarah H. Tolbert, DOI 10.1063/1.4962536. Diana and I wrote the manuscript, Laura assisted with CFO synthesis, Hyeyeon assisted with ellipsometric porosimetry, and Shauna assisted with electron diffraction. Profs. Chang and Tolbert directed the project and edited the manuscripts.

Chapter 3 is to be submitted for publication at *Applied Physics Letters*. I wrote the manuscript, Kevin and Diana assisted with PZT deposition, Ty assisted with XRD, Hyeyeon assisted with ellipsometric porosimetry, and Shauna assisted with electron diffraction. Profs. Chang and Tolbert directed the project and edited the manuscripts.

Chapter 4 is not published. It is a compilation of PZT syntheses and characterizations, which was used in a number of other projects. Prof. Tolbert directed these research efforts.

Chapter 5 is a version of *Journal of Applied Physics* **117**, 174107 (2015), by Kun Liang, Abraham N. Buditama, Diana Chien, Jizhai Cui, Pui Lam Cheung, Sam Goljahi, Sarah H. Tolbert, Jane P. Chang, and Christopher S. Lynch, DOI 10.1063/1.4919431. Kun wrote the manuscript, I assisted with PZT synthesis, and Diana, Jizhai, Cyrus, and Sam assisted with the characterization and the modeling. Profs. Tolbert, Chang, and Lynch directed the project and edited the manuscripts.

Chapter 6 is, at the time of this writing, not yet published. Shauna wrote the manuscript, Hyeyeon assisted with ellipsometric porosimetry, I assisted with CFO thin film synthesis, and Paul assisted with the measurements. Profs. Carman and Tolbert directed the project and edited the manuscripts.

I would firstly like to thank my family and my elders. To my parents, Irwan Buditama and Tina Nataniel, for supporting me in my academic pursuits and for their continued love and prayers. To John Skidmore, who had been like a secondary father to me until his passing. To my uncle and aunt David and Julie Young, for caring for me as if they were my tertiary set of parents during all the years I have lived in southern California.

I would also like to acknowledge my mentors in graduate school, Tom Quickel and Laura Schelhas, for teaching me and for being patient with me. Diana Chien was an excellent collaborator and deserves a special mention, especially for struggling together with me since the early days of these projects. Also from the Chang lab, Kevin Fitzell, Jeffrey Chang, and Cyrus Cheung have been of great help. Additionally, SEM, SQUID, and XRD would have been impossible without the support of Drs. Ignacio Martini and Saeed Khan. Finally, this research would not have been possible without the TANMS center and everyone in it, and so Prof. Greg Carman and Tsai-Tsai O-Lee deserve my thanks, as well as Prof. Jane Chang, Scott Keller, Paul Nordeen, Jizhai Cui, Wei-Yang Sun, and numerous others who have contributed in their own way.

Thank you to my committee members Prof. Jeff Zink, whose group theory class was the most fun to me personally, Prof. Chris Lynch, whose valor is an inspiration, and last but not least, Prof. Sarah Tolbert, whose guidance and support are unmatched. I would also like to acknowldge Prof. Ric Kaner, whose solid-state chemistry class was the most useful in my graduate career, for serving on my oral committee.

To the Tolbies, thank you for demonstrating to me more than I've ever wanted to know about social group dynamics. Thanks in particular to David Watts, Shauna Robbennolt, Erick Harr, Terri Lin, Ty Karaba, Hyeyeon Kang, Ben Lesel, and Stephen Sasaki for your friendships.

Finally, I would like to acknowledge my Dungeons & Dragons crew, for being that cliché group of true friends, who also occasionally teaches very useful things about data analysis and presentation. Michael Yeung, Jordan Aguirre, Robert Boutelle, Devin Brandt, Erik Farr, Matthew Voss, Renato Aguilera, Taylor Aubry-Komin, David Reilley, Logan Stewart, and Harsharn Auluck, I will always treasure our adventures.

Vīta

2005	Prairie State Achievement Award.
2006	National Merit Scholarship.
	Robert C. Byrd Scholarship.
2007	Summer Undergraduate Research Fellowship, Caltech.
2009	Undergraduate Student Researcher, Caltech.
2010	B.S. Chemistry, California Institute of Technology.
2012–2016	Collaborative Learning Workshop Facilitator, UCLA.
2013	M.S. Chemistry, University of California, Los Angeles.
2013–2015	President of the Student Leadership Council, TANMS ERC.

Publications

- Buditama, A. N.; Chien, D.; Fitzell, K.; Karaba, C. T.; Kang, H. Y.; Robbennolt, S.; Chang, J. P.; Tolbert, S. H. Strain transfer in porous multiferroic composites of $CoFe_2O_4$ and $PbZr_xTi_{1-x}O_3$. In preparation.

- Li, X.; Fitzell, K.; Wu, D.; Karaba, C. T.; Buditama, A. N.; Yu, G.; Wong, K. L.; Altieri, N.; Grezes, C.; Kioussis, N.; Tolbert, S. H.; Zhang, Z.; Chang, J. P.; Khalili Amiri, P.; Wang, K. L. Enhancement of voltage-controlled magnetic anisotropy through precise control of Mg insertion thickness at CoFeB|MgO interface. Accepted in *Appl. Phys. Lett.*

- Robbennolt, S.; Kang, H. Y.; Buditama, A. N.; Nordeen, P.; Carman, G. P.; Tolbert, S. H. Fine tuning the magnetic properties of cobalt ferrite thin films by controlling nanoscale structure. In preparation.

- Chien, D.; Buditama, A. N.; Schelhas, L. T.; Kang, H. Y.; Chang, J. P.; Tolbert, S. H. Tuning magnetoelectric coupling using porosity in multiferroic nanocomposites of ALD-grown $Pb(Zr,Ti)O_3$ and templated mesoporous $CoFe_2O_4$. *Appl. Phys. Lett.* **109**, 112904 (2016).

- Liang, K.; Buditama, A. N.; Chien, D.; Cui, J.; Cheung, P. L.; Goljahi, S.; Tolbert, S. H.; Chang, J. P.; Lynch, C. S. The conductivity mechanism and an improved C–V model of ferroelectric PZT thin film. *J. Appl. Phys.* **117**, 174107 (2015).

Presentations

- Buditama, A. N.; Chien, D.; Chang, J. P.; Tolbert, S. H. Polymer-templated mesoporous frameworks for strain-coupled magnetoelectric composites. Oral presentation at the 251st ACS National Meeting & Exposition, San Diego, CA, March 13–17, 2016.

- Buditama, A. N.; Chien, D.; Chang, J. P.; Tolbert, S. H. Polymer-templated mesoporous frameworks for TANMS strain-coupled magnetoelectric composites. Oral presentation at the XXIV IMRC, Cancún, Mexico, August 17–20, 2015.

- Buditama, A. N.; Schelhas, L. T.; Chien, D.; Chang, J. P.; Tolbert, S. H. Nanoarchitectural control of electric and magnetic domains via solution-phase self-assembly. Poster presentation at the XXIII (IMRC), Cancún, Mexico, August 17–21, 2014.

- Buditama, A. N.; Schelhas, L. T.; Chien, D.; Chang, J. P.; Tolbert, S. H. Nanoarchitectural control of electric and magnetic moments via solution-phase self-assembly. Poster presentation at the INC10, Gaithersburg, MD, May 13–15, 2014.

Chapter 1

Introduction

The field of multiferroics began in April 21, 1820, when Hans Christian Ørsted discovered the link between electricity and magnetism. Since then, virtually all magnetic devices have generated their magnetic fields by the same method, by passing current through a wire. However, this mechanism fails to scale as physical dimensions decrease because current flow is proportional to conductor diameter. Thus, as electromagnetic devices become smaller, they also become more inefficient. Nanoscale multiferroics, however, attempt to circumvent this problem in a different way.

A multiferroic is a material that simultaneously exhibits multiple ferroic order parameters, such as ferromagnetism, ferroelectricity, or ferroelasticity. While multiple combinations of these ferroic order parameters can exist (e.g. piezoelectricity or magnetostriction), here we are largely concerned with the coupling between electricity and magnetism, that is, magnetoelectric multiferroics. Intrinsic magnetoelectric multiferroics such as bismuth ferrite ($BiFeO_3$ or BFO) are rare,[1] but composite magnetoelectric multiferroics have been developed by strain-coupling a piezoelectric material with a magnetostrictive material.[2–7]

A commonly used piezoelectric material is lead zirconate titanate ($PbZr_xTi_{1-x}O_3$ or PZT), which exists in the perovskite crystal structure and is a solid solution between isostructural lead titanate ($PbTiO_3$) and lead zirconate ($PbZrO_3$). Below its Curie temperature, PZT spontaneously distorts into a tetragonal, rhombohedral, or monoclinic crystal structure, depending Zr:Ti ratio and temperature.[8,9] Its piezoelectric properties arise from this distortion, which involves a separation

of charges in the material, resulting in an overall electric polarization along the {100} directions for tetragonal PZT and along the {111} for rhombohedral PZT.[10–13]

A commonly used magnetostrictive material is cobalt ferrite ($CoFe_2O_4$ or CFO), which is a ferrimagnetic, (mostly) inverse spinel. Fe^{3+} ions occupy both tetrahedral and octahedral sites, and their spins are antialigned through superexchange, the dominant exchange interaction in the material. Thus, to the degree that it is an inverse spinel, CFO's magnetization results from its Co^{2+} ions.[14,15] CFO's magnetostrictive properties arise because straining the material necessarily modifies the bonding orbitals and alters the energy landscape of the spin states through spin–orbit coupling.[16,17]

The first part of this thesis deals with magnetoelectric, multiferroic composites of PZT and CFO, and the second deals with controlling domain-level properties of these materials using solution processing. Though thin film composites of these materials exist in the literature, there is little control over the nanoarchitecture of the material. In contrast, these samples are made by creating a mesoporous framework of CFO, then conformally filling the framework with PZT. The mesoporous framework is synthesized by a polymer-templated sol-gel process, while the conformal filling is done by atomic layer deposition (ALD). Chapter 2 explores the first of these systems, a porous framework of CFO filled with a thin layer of PZT. It was found that the composites displayed a reduction in magnetization saturation as measured by SQUID magnetometry upon *ex situ* electrical poling, and this change is increased for more porous samples, suggesting that porosity serves to enhance magnetoelectric coupling in these composites.

Chapter 3 more fully explores this strain coupling. Composites with a range of PZT thicknesses are prepared and poled in the same way as the samples of the previous chapter. X-ray diffraction is used to probe the strain states of both the CFO and PZT. We found that the out-of-plane strain of the CFO increases with increasing porosity, demonstrating increased strain transfer from the PZT upon electrical poling. This strain corresponds with a greater change in saturation magnetization as measured by Superconducting Quantum Interference Device (SQUID) magnetometry, thus leading to the aforementioned improved magnetoelectric coupling.

Whereas the previous chapters focused on composites with a porous CFO framework, chapter 4 explores syntheses of PZT thin films, including that of a porous PZT framework. PZT solutions were deposited by either dip coating or spin coating onto platinized silicon substrates. The thickness, nanoarchitecture, and orientation can be controlled by a combination of parameters including block copolymer templating, pre-crystallization heating conditions, and solution stoichiometry. Orientation of the film is propagated throughout the porous network, allowing the synthesis of a textured, mesoporous PZT thin film to achieve ideal piezoelectric properties suitable for multiferroic applications.

Chapter 5 explores the modeling of PZT films of thicknesses around 10^{-7} m. Bulk PZT has been thoroughly examined in the literature, and ultrathin PZT films (less than 10 nm) have been explored in the recent past.[18,19] Mesoscale PZT, is large enough to allow for domain reorientation, and modeling of PZT on this scale requires consideration of interactions absent in both the macro- and nanoscale. PZT films were here synthesized using the iterative spin coating process described in chapter 4, and they were used to experimentally confirm new models of mesoscale PZT films.

Chapter 6 explores the material and magnetic properties of nanocrystal-based and sol-gel-derived CFO thin films. We have found that the static magnetic properties of these films may be tuned by the nanoarchitecture, with nanocrystal-based films reaching the lowest coercivities. As the grain size of the CFO decreases, the magnetic domain size becomes limited, which correspondingly reduces the the coercivity. This can be achieved by using nanocrystal-based films or by incorporating porosity into sol-gel-derived films. Control over these static magnetic properties come with no loss to the dynamic magnetic properties, as confirmed by ferromagnetic resonance (FMR) measurements.

Finally, chapter 7 summarizes this work. Supplementary information is provided in the appendix, which covers sol-gel syntheses, electrical poling methods, and XRD peak fitting methods.

References

(1) Hill, N. A. *The Journal of Physical Chemistry B* **July 2000**, *104*, 6694–6709.

(2) Wan, J. G.; Wang, X. W.; Wu, Y. J.; Zeng, M.; Wang, Y.; Jiang, H.; Zhou, W. Q.; Wang, G. H.; Liu, J.-M. *Applied Physics Letters* **2005**, *86*, 122501.

(3) Zhou, J.-p.; He, H.-c.; Shi, Z.; Liu, G.; Nan, C.-W. *Journal of Applied Physics* **Nov. 2006**, *100*, 094106.

(4) Ortega, N.; Bhattacharya, P.; Katiyar, R. S.; Dutta, P.; Manivannan, A.; Seehra, M. S.; Takeuchi, I.; Majumder, S. B. *Journal of Applied Physics* **2006**, *100*, 126105.

(5) Tahmasebi, K.; Barzegar, A.; Ding, J.; Herng, T. S.; Huang, A.; Shannigrahi, S. *Materials and Design* **2011**, *32*, 2370–2373.

(6) Wang, J.; Li, Z.; Wang, J.; He, H.; Nan, C. *Journal of Applied Physics* **2015**, *117*, 044101.

(7) Chien, D.; Buditama, A. N.; Schelhas, L. T.; Kang, H. Y.; Robbennolt, S.; Chang, J. P.; Tolbert, S. H. *Applied Physics Letters* **2016**, *109*, 112904.

(8) Noheda, B.; Cox, D. E.; Shirane, G.; Gonzalo, J. A.; Cross, L. E.; Park, S.-E. *Applied Physics Letters* **1999**, *74*, 2059.

(9) Noheda, B.; Gonzalo, J. A.; Cross, L. E.; Guo, R.; Park, S.-E.; Cox, D. E.; Shirane, G. *Physical Review B* **Apr. 2000**, *61*, 8687–8695.

(10) Warren, W. L.; Robertson, J.; Dimos, D.; Tuttle, B. A.; Pike, G. E.; Payne, D. A. *Physical Review B* **Mar. 1996**, *53*, 3080–3087.

(11) Guo, R.; Cross, L. E.; Park, S.-E.; Noheda, B.; Cox, D. E.; Shirane, G. *Physical review letters* **June 2000**, *84*, 5423–6.

(12) Gong, W.; Li, J.-F.; Chu, X.; Gui, Z.; Li, L. *Journal of Applied Physics* **2004**, *96*, 590.

(13) Schönau, K. A.; Knapp, M.; Kungl, H.; Hoffmann, M. J.; Fuess, H. *Physical Review B* **Oct. 2007**, *76*, 1–12.

(14) Sawatzky, G. A.; Van Der Woude, F.; Morrish, A. H. *Journal of Applied Physics* **1968**, *39*, 1204–1205.

(15) Slonczewski, J. C. *Physical Review* **June 1958**, *110*, 1341–1348.

(16) Slonczewski, J. C. *Journal of Applied Physics* **1961**, *32*, S253.

(17) Suzuki, Y.; Hu, G.; van Dover, R. B.; Cava, R. J. *Journal of Magnetism and Magnetic Materials* **1999**, *191*, 1–8.

(18) Shaw, T. M.; Trolier-McKinstry, S.; McIntyre, P. C. *Annual Review of Materials Science* **Aug. 2000**, *30*, 263–298.

(19) Tayebi, N.; Kim, S.; Chen, R. J.; Tran, Q.; Franklin, N.; Nishi, Y.; Ma, Q.; Rao, V. *Nano Letters* **2012**, *12*, 5455–5463.

Chapter 2

Tuning magnetoelectric coupling using porosity in multiferroic nanocomposites of ALD-grown lead zirconate titanate and templated mesoporous cobalt ferrite

Abraham N. Buditama, Diana Chien, Laura T. Schelhas, Hye Yeon Kang, Shauna Robbennolt, Jane P. Chang, and Sarah H. Tolbert

Abstract

In this manuscript, we examine ways to create multiferroic composites with controlled nanoscale architecture. We accomplished this by uniformly depositing piezoelectric lead zirconate titanate (PZT) into templated mesoporous, magnetostrictive cobalt ferrite (CFO) thin films to form nanocomposites in which strain can be transferred at the interface between the two materials. To study the magnetoelectric coupling, the nanostructure was electrically poled *ex situ* prior to magnetic measurements. No samples showed a change in in-plane magnetization as a function of voltage due to substrate clamping. Out-of-plane changes were observed, but contrary to expectations based on total PZT volume fraction, mesoporous CFO samples partially filled with PZT showed more change in out-of-plane magnetization than the sample with fully filled pores. This

result suggests that residual porosity in the composite adds mechanical flexibility and results in greater magnetoelectric coupling.

Introduction

Multiferroic composites, which are materials that simultaneously exhibit at least two ferroic order parameters, are of particular interest due to their potential application in nanoscale devices.[1–6] Magnetoelectric multiferroics, in specific, couple ferroelectric and (anti)ferromagnetic responses. One path to such materials is through strain-coupling of a piezoelectric and a magnetostrictive material.[7–11] When an external electric field is applied to such a composite, the ferroelectric is strained, and this strain is transferred to the magnetostrictive to induce a change in magnetization. Thus, magnetization can be controlled using an electric field, and conversely, electric polarization using a magnetic field. This phenomenon relies on strain transfer at the interface of the two materials and has been demonstrated to show higher magnetoelectric coupling than single-phase multiferroics.[8] To maximize strain-coupling, a large interface area is desirable, and popular techniques for achieving this include, but are not limited to, spontaneous nanoscale phase-separation during sputter co-deposition to create columnar structures in a matrix,[12,13] sol-gel methods to create nanoparticles embedded in a matrix,[14–16] and multilayer depositions to create alternating sheets.[17,18]

In this work, our goal was to achieve more controlled three-dimensional nanoscale structures by first producing a well-defined nanoporous network using polymer templating of sol-gel derived thin films, followed by conformal filling of the pores using atomic layer deposition (ALD). The two materials chosen for these nanocomposites are piezoelectric lead zirconate titanate ($PbZr_{0.52}Ti_{0.48}O_3$ or PZT) and negative magnetostrictive cobalt ferrite ($CoFe_2O_4$ or CFO). Both materials have extensive literature documenting their respective ferroic properties, and composite structures using the two materials have also generated significant interest.[19–26] However, these previously synthesized composites are all dense structures, and like all dense thin films, they

suffer from substrate clamping, which hinders in-plane strain and limits magnetoelectric coupling. To alleviate this problem, here mechanical flexibility was introduced by creating a composite with nanoscale porosity.

The composite is composed of a mesoporous CFO framework into which a thin layer of PZT is deposited. The CFO framework was fabricated using block-copolymer templating of sol-gel-derived films; this technique has been used to produce many metal oxides with a variety of three-dimensional nanoarchitectures.[27–33] During the synthesis, polymer micelles formed periodic organic domains within the film, which could be converted to a homogeneous network of interconnected pores upon pyrolysis of the polymer template. The pores could then be coated with secondary materials using ALD, translating the original polymer architecture into the inorganic composite. This control over morphology is of particular interest to ferroic materials, as structure effects on mechanical flexibility can drastically alter strain states in materials, and subsequently, the overall ferroic properties.[33,34]

Atomic layer deposition is a type of chemical vapor deposition based on alternating, self-limiting surface reactions to obtain layer-by-layer growth. Here ALD allowed for homogeneous, conformal deposition throughout the porous CFO framework. In ALD, alternating pulses of gaseous precursors react with all active surface sites until saturation is reached. Due to the self-limiting nature of the reactions, less than a monolayer of material is deposited during each pulse, which provides excellent control over stoichiometry and thickness.[35] This technique allows for conformal, ultra-thin deposition of PZT onto a surface of any shape, and was used to create a PZT/CFO composite with high interfacial area. Depending on how much PZT was deposited, the porous network could either be completely or partially filled, providing fine control over the final porosity of the material.

In this work, we therefore examine magnetoelectric coupling in composites with different pore structures. By controlling the degree to which the pores are filled, the mechanical flexibility of the films can be tuned, directly affecting the amount of strain that can be expressed in the material.

Here we examine the effect of that strain by measuring the magnetization of the composite films after *ex situ* application of an electric field.

Experimental

The synthesis of the mesoporous CFO framework has been outlined previously.[34] Further details can be found in the experimental section of the supplementary material. The ALD process has also been presented previously.[36,37] For this work, some different heating conditions were used: $Pb(TMHD)_2$, $Ti(O\text{-}i\text{-}Pr)_2(TMHD)_2$, and $Zr(TMHD)_4$ were heated up to 115 °C, 95 °C, and 180 °C, respectively, during the deposition.

PZT/CFO nanocomposites were synthesized by depositing ALD PZT thin film with thicknesses of 3 nm and 6 nm into 100 nm–thick templated mesoporous CFO samples. Composites were rapidly thermally annealed (RTA) at 700 °C for 1 min in an oxygen environment to crystallize the PZT thin films. The morphology of the nanocomposites was confirmed using a JEOL JSM-6700F field-emission scanning electron microscope (FE-SEM). The crystalline structures were investigated using a combination of electron diffraction, collected on an FEI Titan S/TEM operating at 300 kV and selected area aperture at 50 µm, and grazing incidence wide angle X-ray scattering (GIWAXS), collected at the Stanford Synchrotron Radiation Lightsource (SSRL) using beamline 11-3. Elemental analyses were performed using a Kratos AXIS X-ray photoelectron spectroscopy (XPS) and an FEI Titan scanning transmission electron microscopy (STEM). Ellipsometric porosimetry was performed on a Semilab PS-1100 in the spectral range of 1.24 eV to 4.5 eV. Contact-mode piezoforce microscopy (PFM) was performed on a Bruker Dimensions FastScan Scanning Probe Microscope. More details on all equipment used can be found in the experimental section of the supplementary material.

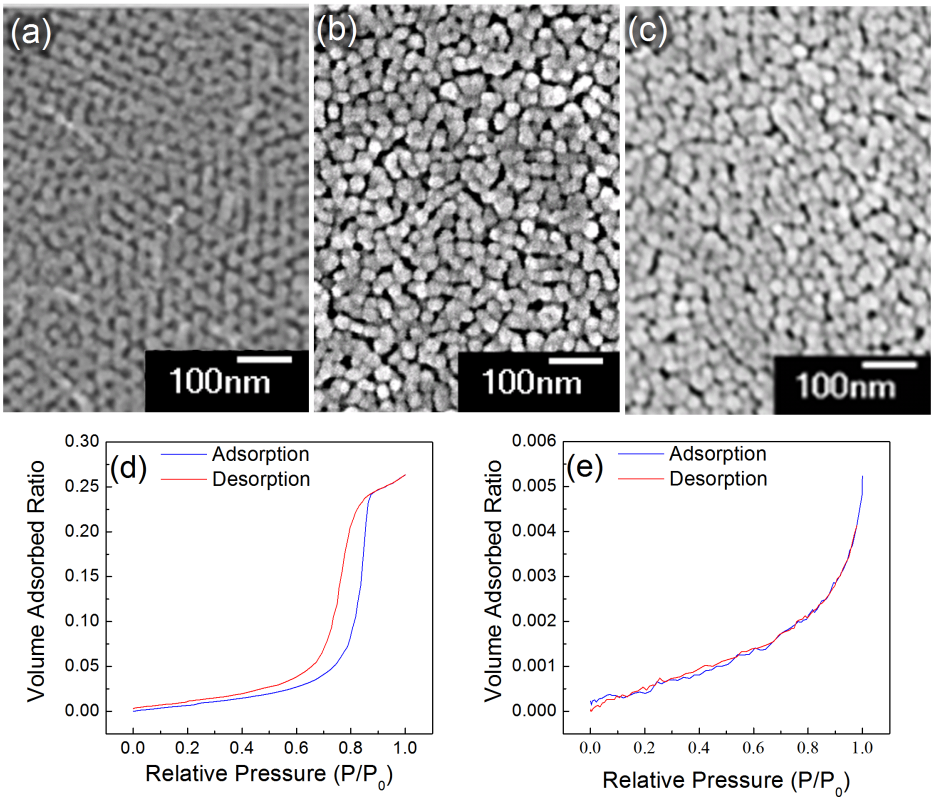

Figure 2.1: (a–c) Tilted top view SEM images show unfilled pores in the mesoporous CFO matrix (a), pores filled with as-deposited 3 nm ALD PZT (b), and pores filled with as-deposited 6 nm ALD PZT (c). (d–e) Ellipsometric porosimetry isotherms for unfilled mesoporous CFO (d) and mesoporous CFO filled with 6 nm of ALD PZT and annealed at 700 °C (e). Unfilled pores show 30% porosity, while filled materials have less than 1% accessible pore volume.

Results and discussion

The first goal of this work is to fully characterize both the nanoporous host and the final composite material. The mesoporous CFO is shown to have ordered pores, as seen through SEM (figure 2.1a). The pore radius is 9 nm and neck radius is 6 nm, confirmed by TEM and SEM. After synthesis, 3 nm or 6 nm of ALD PZT were deposited onto the neck and pore walls of the CFO framework, as confirmed via SEM and shown in figures 2.1b,c, respectively. The thicknesses of ALD PZT thin film were chosen based on the mesoporous CFO architecture: the 3 nm PZT was chosen so that the neck and pore walls were not fully coated, allowing more porosity and presumably more flexibility in the mesoporous CFO when compared to the 6 nm–thick PZT film. The 6 nm ALD PZT film should fully fill all necks, so 6 nm was chosen as the thickest film we could utilize without depositing an undesired overlayer of PZT on top of the mesoporous CFO matrix. Note that the neck size would be completely filled with 6 nm of PZT, impeding gas flow through the network, but the pores themselves should not be completely filled. Once the necks were filled, however, the gas reactants for PZT would not have access into the pores, so PZT would deposit only on top of the mesoporous CFO matrix.

ALD PZT thin films were deposited as an amorphous layer, so samples were crystallized by rapid thermal annealing (RTA) at 700 °C for 1 min in an oxygen environment. Electron diffraction confirms that the CFO and PZT both have the correct crystalline structure, as shown in figure 2.2. Because of the small thickness of the ALD PZT layer, the PZT peaks are weaker than the CFO peaks, and some of the PZT peaks are convoluted with CFO peaks. The PZT{210} peak, however, is unobstructed. GIWAXS shows similar trends (see figure 2.6). XPS further shows a Zr:Ti ratio of 60:40 (figure 2.7). This ratio is expected for a sample with a 52:48 Zr:Ti ratio because XPS is highly surface sensitive and PZT surfaces tend to be Zr-rich.[38] Finally, PFM confirms that the ALD PZT displays piezoelectric characteristics, both on a flat Pt electrode and inside the CFO framework (figure 2.8).

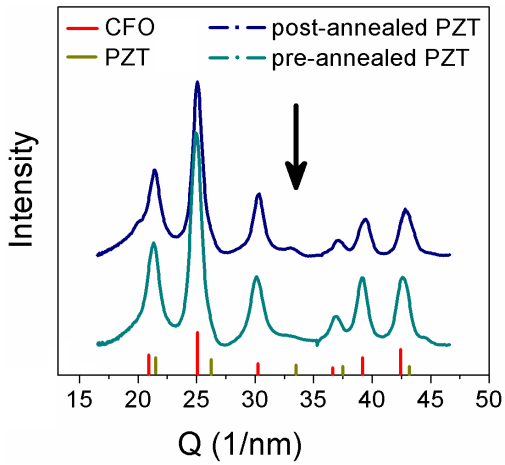

Figure 2.2: Electron diffraction shows that the CFO and PZT are polycrystalline, and the CFO exhibits no preferred orientation. All CFO peaks can be indexed to the cubic spinel structure (JCPDS card 00-022-1086). Many PZT peaks (JCPDS card 00-033-0784) overlap CFO peaks, but the PZT(102) peak is visible and marked with an arrow.

The mesoporosity of the CFO and PZT/CFO composite films was studied by ellipsometric porosimetry using toluene gas vapor as adsorbate.[39] A typical type IV behavior isotherm is obtained from the CFO film showing 30% porosity (figure 2.1d).[40] A distinctive hysteresis loop at relative higher pressure indicates that the CFO film possesses an interconnected mesoporous network. After ALD deposition and RTA, the porosity was reduced to less than 1% (figure 2.1e), confirming that the deposition and annealing of 6 nm–thick PZT has filled the accessible pores in the CFO framework.

Finally, cross-sectional TEM images of a mesoporous CFO film filled with 3 nm–thick PZT and over-coated with Pt (figure 2.3a) show the expected nanoscale structure. To better confirm the conformal nature of the ALD-PZT layers, energy-dispersive X-ray spectroscopy (EDS) was used on this sample to do elemental mapping on a $39 \times 38\,\mathrm{nm}^2$ area, as shown in figure 2.3b–d. Part (b) shows the PZT rich domain, part (c) the CFO rich regions, and part (d) is an overlay, indicating that the PZT and CFO locations are mostly mutually exclusive. The EDS map confirms that PZT was deposited in a thin layer and that the PZT coats the pores all the way through the 100 nm–thick mesoporous CFO.

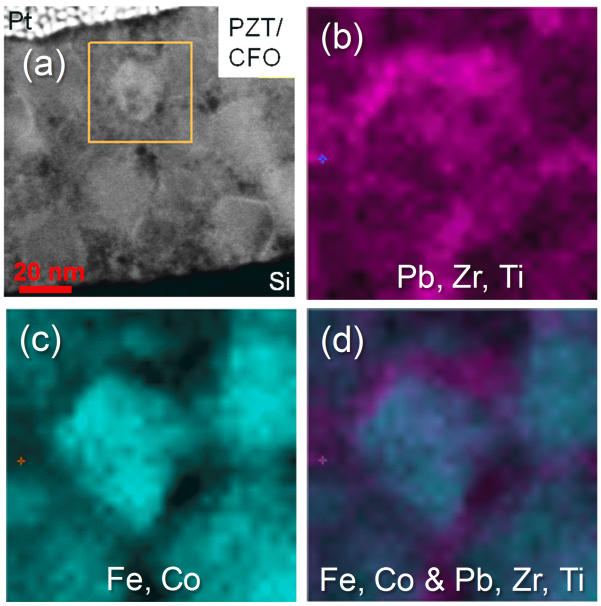

Figure 2.3: Cross-sectional TEM of a porous CFO sample coated with 3 nm PZT. The box shows the $39 \times 38\,\mathrm{nm}^2$ region used for EDS mapping, shown in (b–d). Mapping of Pb, Zr, and Ti is shown in (b), Fe and Co in (c), and panel (d) shows an overlay of the data from (b) and (c). In (d), the pink PZT can be seen as a thin layer, coating the blue CFO.

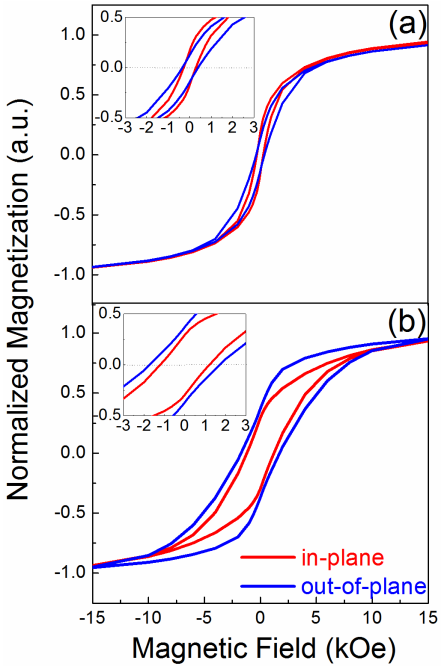

Figure 2.4: SQUID magnetometry collected on mesoporous CFO filled with ALD PZT as-deposited (a) and annealed at 700 °C (b). Depositing ALD PZT into the pores did not affect the magnetic properties of the mesoporous CFO, but RTA annealing induced some out-of-plane magnetic anisotropy.

In synthesizing magnetoelectric nanocomposites, it is important to determine the effect of depositing the ALD PZT film on the magnetic properties of the mesoporous CFO. The magnetization was measured using a Quantum Design MPMS superconducting quantum interference device (SQUID) magnetometer both in-plane (i.e. with the magnetic field parallel to the sample surface) and out-of-plane (i.e. with the magnetic field perpendicular to the sample surface) using magnetic fields up to ±2 T. As shown in figure 2.4, the as-deposited PZT/CFO nanocomposite were fairly magnetically soft with little in-plane/out-of-plane magnetic anisotropy. After annealing the nanocomposite at 700 °C, however, it became magnetically harder and more anisotropic, with a preference for out-of-plane magnetization. The coercivity increase is similar to that observed in unfilled porous CFO upon RTA annealing (see figure 2.9), and likely results from thermally induced grain growth. Changes in magnetic anisotropy are not observed in pure porous CFO, and thus likely stem from strain at the PZT/CFO interface. As shown previously,[34] mesoporous CFO is mechanically flexible, but the pores can only flex out-of-plane because the CFO thin film is covalently bound to the Si substrate (i.e. clamped), limiting in-plane strain in the CFO layer. Because of this clamping, we expect to see dominantly out-of-plane magnetization changes. CFO is negative magnetostrictive, so PZT crystallization and the associated volume decrease should result in in-plane tension combined with relaxed bonding out-of-plane, producing an out-of-plane easy magnetic axis.[34]

In order to observe the effect of magnetoelectric coupling in the PZT/CFO nanocomposite, the samples were poled *ex situ* with the electric field perpendicular to the sample surface. A 300 nm–thick titanium layer was deposited as a back electrode on the backside of a PZT/CFO nanocomposite sample grown on conductive silicon using a CVC 601 sputtering system. The 5×5 mm^2 PZT/CFO nanocomposite samples was then covered with a 12.7 µm–thick polyvinylidene chloride spacer and physically sandwiched between two aluminum electrodes, 1.28 cm in diameter. The nanocomposite was electrically poled for 10 min with applied electric fields E_{eff} ranging from 0 $\mathrm{MV\,m^{-1}}$ to 1.42 $\mathrm{MV\,m^{-1}}$. E_{eff} was calculated by dividing the voltage drop across the sample and dividing by the total thickness of the PZT/CFO nanocomposite (usually 100 nm). It is expected

that much of the polarization will be lost from the PZT after the field is removed. This polarization loss is initially fast and then stabilizes; indeed, after the initial few milliseconds, polarization loss has been shown to be logarithmic in time.[41,42] Given the hours-long measurement time, it is safe to assume that there will be no significant change in the remanent polarization after the initial decay. Samples can be depoled, however, by heating to 200 °C.

The strain from the remanent polarization in the piezoelectric PZT is transferred to the magnetostrictive CFO and should result in a change in magnetization. To measure this change, sample magnetization was subsequently measured by SQUID magnetometry. In-plane and out-of-plane magnetization data for both the 3 nm–thick and 6 nm–thick PZT composites are shown in figure 2.5. In both nanocomposites, the in-plane results (figures 2.5a and 2.5c) show that there is no significant change in magnetization (1.2–3.6%) as a function of electric field. This result is expected due to the effect of substrate clamping.

On the other hand, the out-of-plane magnetization (figures 2.5b and 2.5d) is not subject to substrate clamping, and so changes should be visible. Because the polarization of ultrathin PZT has been shown to decrease with decreasing thickness,[43,44] we expected that the composite with the thicker PZT layer would be able to generate a greater strain in the CFO framework, producing a larger change in magnetization. Instead, the mesoporous CFO coated with the thinner 3 nm–thick PZT film shows a greater change, with the saturation magnetization increasing 15.4% compared to 10.3% for the 6 nm–thick PZT film. We explain this result by the fact that the 3 nm–PZT system with its pores only partially filled retains more mechanical flexibility compared to the 6 nm–PZT composite. This pore flexing should allow for more bond distortion in the PZT and in turn more bond distortion in the covalently coupled CFO; this in turn should result in more changes in the magnetic properties of the CFO. The result is enhanced magnetoelectric coupling. We can calculate the magnetoelectric coefficient $\alpha = \mu_0 \frac{\mathrm{d}M}{\mathrm{d}E}$ by using the difference in saturation magnetization. At the point of switching, $\alpha = 1.0 \times 10^{-7}\,\mathrm{s\,m^{-1}}$, which is comparable to PZT/CFO structures synthesized by co-sputtering[45] and by pulsed laser deposition[46] which show α values in the range of $10 \times 10^{-8}\,\mathrm{s\,m^{-1}}$ to $10 \times 10^{-6}\,\mathrm{s\,m^{-1}}$.[45,46]

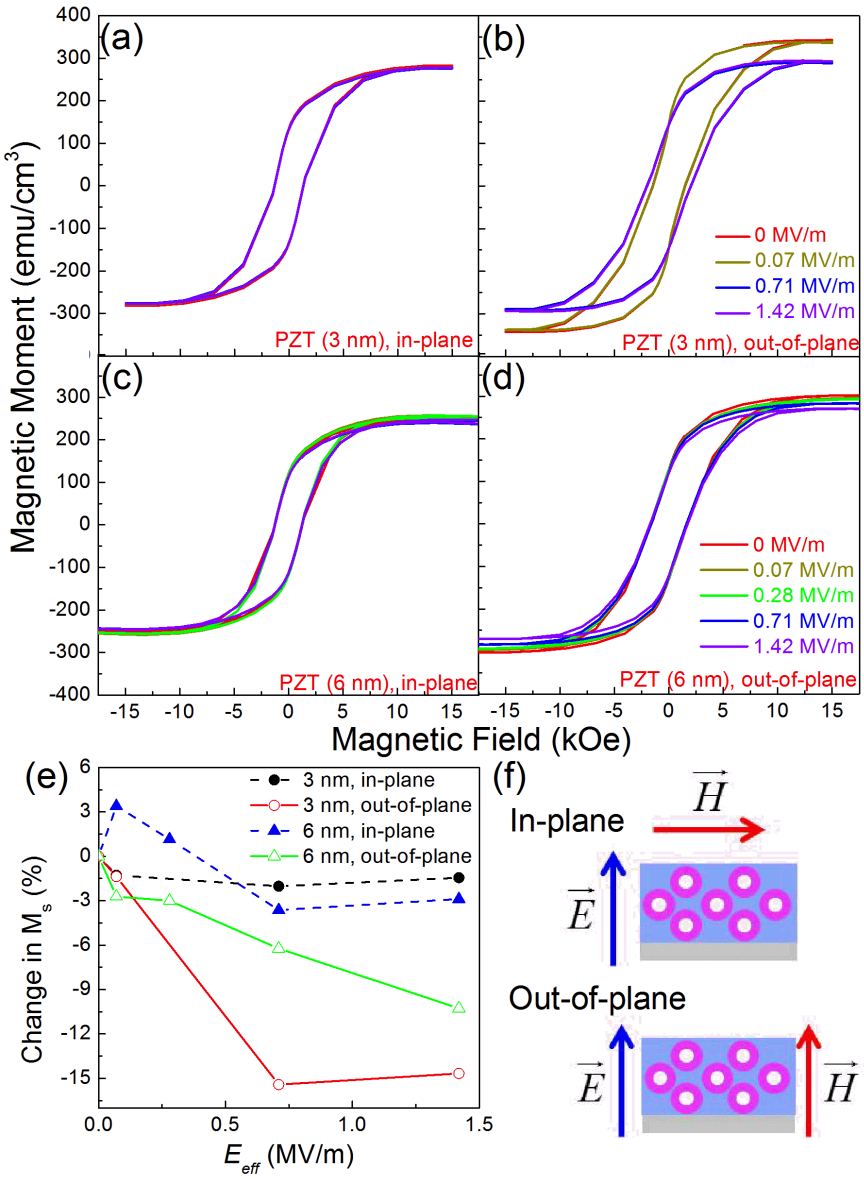

Figure 2.5: Magnetic properties of porous CFO filled with 3 nm (a–b) and 6 nm (c–d) ALD PZT, annealed at 700 °C. The samples were *ex situ* poled between 0 and 1.42 MV m^{-1} and the magnetic moment was measured with the applied field parallel to the plane of the sample (a, c) or perpendicular to the substrate (b, d). Part (e) shows the percentage change in M_s (relative to M_s at 0 V) versus E_{eff}. Part (f) is a schematic showing the direction of applied external fields with respect to the sample surface.

Conclusion

While both sol-gel and CVD based gas-phase deposition methods have been used previously to synthesize multiferroic nanocomposites, here we combine these two methods to produce multiferroic nanostructures with residual porosity. Although further studies are clearly needed, this work shows that combining ALD and wet chemistry techniques provides unique capability for synthesizing nanocomposites with complex three-dimensional architectures that include porosity and demonstrate significant magnetoelectric coupling. This method thus allows us to add an additional parameter (i.e. porosity) to our nanocomposite architectural toolbox.

Overall, these experiments indicate that magnetoelectric coupling can be facilitated in a nanostructured film made by depositing ALD PZT into a templated mesoporous CFO matrix. Because of the precise control of the ALD method, both fully filled pores (here limited by the 6 nm neck size) and partially filled pores (here chosen to be 3 nm) can be produced. A broad range of experimental methods are then needed to characterize such composites across length scales, including SEM, XPS, XRD, and TEM. Characterizing magnetoelectric coupling using *ex situ* electrical poling coupled with SQUID magnetometry shows surprising results. While there was no change in-plane magnetization due to substrate clamping, the out-of-plane magnetization exhibited significant changes. Interestingly, the samples with mostly filled pores that contained more PZT showed weaker coupling than the samples with partially filled CFO pores and a smaller PZT volume fraction, suggesting that residual porosity allows mechanical flexibility, which in turn enhances magnetoelectric coupling. This work thus emphasizes the importance of porosity as a structural design parameter in the fabrication of composite multiferroic materials. While excessive porosity can cause shorting in piezoelectric materials, sealed porosity, like that employed here, appears to be highly beneficial for strain mediated magnetoelectric coupling.

See supplementary material for additional figures and complete experimental and instrumentation methods.

Acknowledgments

This work was supported by the NSF Nanosystems Engineering Research Center for Translational Applications of Nanoscale Multiferroic Systems (TANMS) under Cooperative Agreement Award EEC-1160504. The authors thank Noah Bodzin for FIB, Sergey Prikhodko for TEM and EDS, and Rachel Huber and Amy Ferreira for help with X-ray diffraction. This work made use of the UCLA Nanoelectronics Research Facility (NRF), the Electron Imaging Center for NanoMachines (EICN) supported by NIH (1S10RR23057 to ZHZ) at the California NanoSystems Institute (CNSI), and the UCLA Molecular Instrumentation Center (MIC). This manuscript contains data collected at the Stanford Synchrotron Radiation Lightsource (SSRL), experimental station 11-3. SSRL and the SLAC National Accelerator Laboratory, is supported by the U.S. Department of Energy, Office of Science, Office of Basic Energy Sciences under Contract No. DE-AC02-76SF00515.

Supplementary Material

The amphiphilic diblock copolymer used to template the CFO films was synthesized for this work using published methods.[47,48] The polymer was poly((ethylene-*co*-propylene)-*block*-poly-(ethylene oxide), with a mass ratio of PEP(3900)-*b*-PEO(4000), a block ratio of PEP_{56}-*b*-PEO_{91}, and a PDI = 1.05. In a typical porous CFO synthesis, PEP-*b*-PEO (0.04 g) was dissolved in 1 ml of EtOH and stirred for at least one day.[34] $Fe(NO_3)_3 \cdot 9\,H_2O$ (0.31 g) and $Co(NO_3)_2 \cdot 6\,H_2O$ (0.11 g) were then dissolved in 1 ml of 2-methoxyethanol, 1 ml of EtOH, and 0.02 ml of glacial acetic acid. Both iron and cobalt precursors were purchased from Sigma-Aldrich at 99.999% purity. Once the solution was homogeneous, the PEP-*b*-PEO solution was added, for a total sol volume of roughly 3.2 ml. The solution was then allowed to clarify by magnetic stirring for 1 h. Films were dip coated from the solution onto Si wafers in a humidity-controlled chamber set to 10–20% relative humidity. The withdrawal rate was usually near 2 mm s^{-1} but was varied, depending on desired thickness.

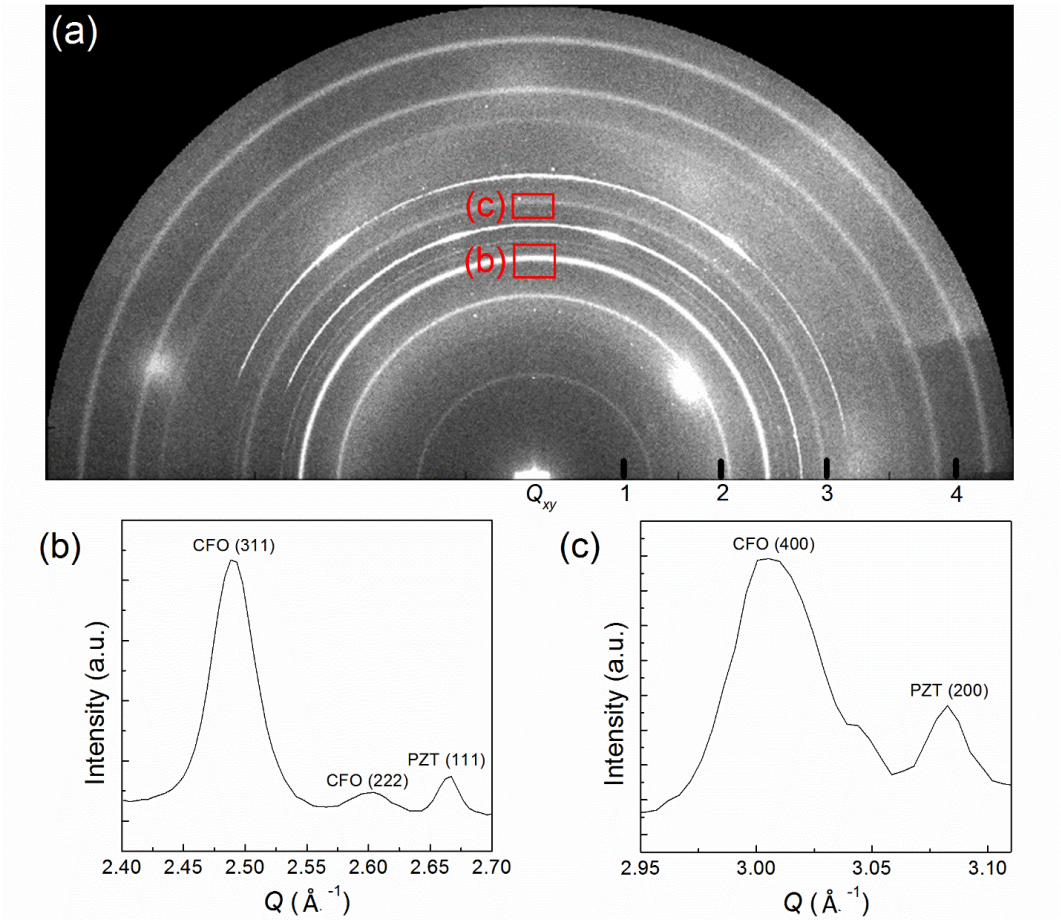

Figure 2.6: 2D-GIWAXS shows that the CFO and PZT are polycrystalline and exhibit no preferred orientation. Insets (b) and (c) show integration over selected CFO and PZT peaks.

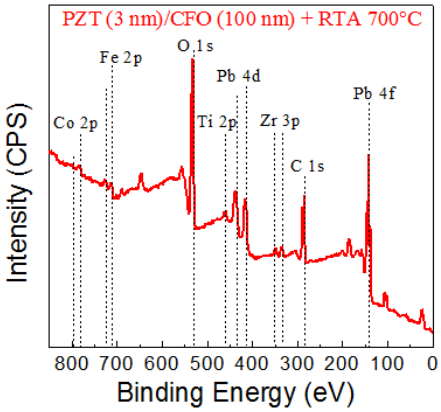

Figure 2.7: XPS survey of annealed 3 nm PZT deposited on 100 nm porous CFO shows that the expected elements are present in the sample.

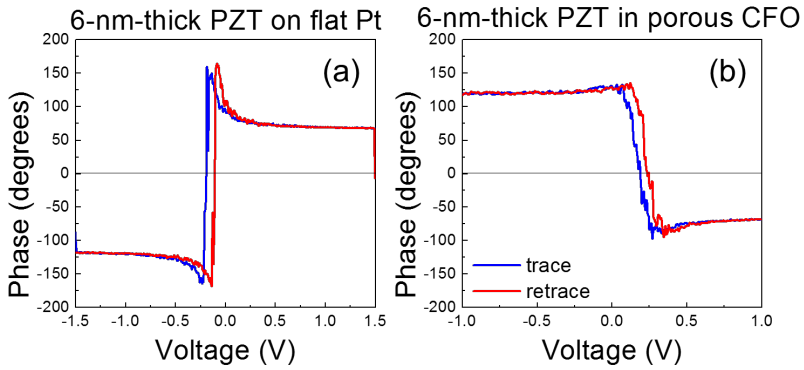

Figure 2.8: PFM data collected on 6 nm–thick ALD PZT films deposited directly onto a flat Pt electrode (a), and into our porous CFO on conductive Si (b). Similar data is observed for both samples, although the coercivity of the composite sample is lower, likely due to reduced substrate clamping in the flexible porous matrix.

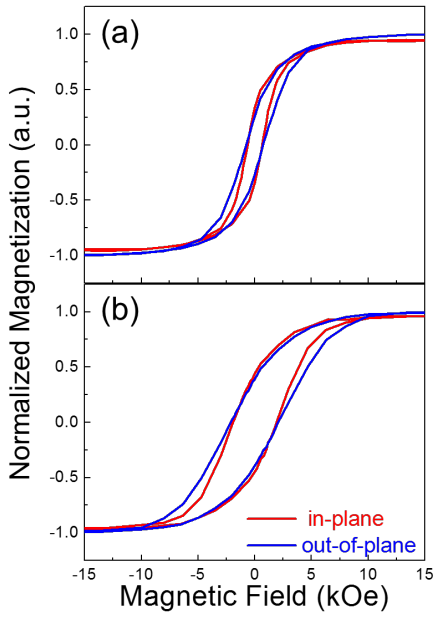

Figure 2.9: SQUID magnetometry collected on unfilled mesoporous CFO after crystallization at 550 °C (a) and after subsequent rapid thermal annealing (RTA) at 700 °C (b). Magnetization is similar to that of pre-annealed and post-annealed CFO in the PZT/CFO composite (figure 4), indicating that the PZT deposition process does not have a significant effect on the magnetization. There is a slightly larger increase in coercivity in the pure CFO sample upon RTA annealing, however, likely because the PZT prevents some grain growth. The PZT/CFO sample also shows slightly more out-of-plane magnetic anisotropy, possibly due to strain at the PZT/CFO interface.

To form rigid inorganic/organic structures, the films were calcined in air at 80 °C for 6 h, at 130 °C for 8 h, and at 180 °C for 6 h for a total heating time of 24 h including temperature ramps.

The morphology and thickness of the nanocomposites was confirmed using a JEOL JSM-6700F field-emission scanning electron microscopy (FE-SEM). Crystalline structures were investigated using a combination of electron and X-ray diffraction. Electron diffraction was collected on an FEI Titan scanning transmission electron microscope (S/TEM) operating at 300 kV and selected area aperture at 50 µm. Grazing incidence wide angle X-ray scattering (GIWAXS) was collected at the Stanford Synchrotron Radiation Laboratory (SSRL) using beamline 11-3 at a wavelength of $\lambda = 0.9744$ Å. Elemental analyses were performed using the aforementioned FEI Titan S/TEM and X-ray photoelectron spectroscopy (XPS). XPS studies made use of a Kratos AXIS Ultra DLD with a monochromatic (Al K_α) source. Contact-mode piezoforce microscopy (PFM) was performed on a Bruker Dimensions FastScan Scanning Probe Microscope with a rotated silicon tip with a height of 2.5 µm to 8 µm, a nominal radius of 5 nm, and a maximum radius of 12 nm. Ellipsometric porosimetry was performed on a Semilab PS-1100 in the spectral range of 1.24 eV to 4.5 eV. A UV-vis CCD detector adapted to a grating spectrograph analyzes the signals reflected by the sample from a 75 W Hamamatsu Xenon lamp. Data analysis was performed using the associated SEA software. Magnetic measurements were carried out on a Quantum Design MPMS 5T SQUID magnetometer with RSO detection.

References

(1) Spaldin, N. A.; Fiebig, M. *Science* **July 2005**, *309*, 391–2.

(2) Nan, C.-W.; Bichurin, M. I.; Dong, S.; Viehland, D.; Srinivasan, G. *Journal of Applied Physics* **2008**, *103*, 031101.

(3) Vaz, C. A. F.; Hoffman, J.; Ahn, C. H.; Ramesh, R. *Advanced Materials* **Apr. 2010**, *22*, 2900–2918.

(4) Hwang, H. Y.; Iwasa, Y.; Kawasaki, M.; Keimer, B.; Nagaosa, N.; Tokura, Y. *Nature Materials* **Jan. 2012**, *11*, 103–113.

(5) Bibes, M.; Villegas, J. E.; Barthélémy, A. *Advances in Physics* **Feb. 2011**, *60*, 5–84.

(6) Wang, Y.; Hu, J.; Lin, Y.; Nan, C.-W. *NPG Asia Materials* **Apr. 2010**, *2*, 61–68.

(7) Ramesh, R.; Spaldin, N. A. *Nature materials* **Jan. 2007**, *6*, 21–9.

(8) Lawes, G.; Srinivasan, G. *Journal of Physics D: Applied Physics* **June 2011**, *44*, 243001.

(9) Martin, L. W.; Chu, Y.-H.; Ramesh, R. *Materials Science and Engineering: R: Reports* **May 2010**, *68*, 89–133.

(10) Martin, L. W.; Crane, S. P.; Chu, Y.-H.; Holcomb, M. B.; Gajek, M.; Huijben, M.; Yang, C.-H.; Balke, N.; Ramesh, R. *Journal of Physics: Condensed Matter* **Oct. 2008**, *20*, 434220.

(11) Eerenstein, W.; Mathur, N. D.; Scott, J. F. *Nature* **Aug. 2006**, *442*, 759–765.

(12) Zheng, H. et al. *Science* **Jan. 2004**, *303*, 661–3.

(13) Aimon, N. M.; Choi, H. K.; Sun, X. Y.; Kim, D. H.; Ross, C. A. *Advanced Materials* **May 2014**, *26*, 3063–3067.

(14) Zhong, X. L.; Wang, J. B.; Liao, M.; Huang, G. J.; Xie, S. H.; Zhou, Y. C.; Qiao, Y.; He, J. P. *Applied Physics Letters* **2007**, *90*, 152903.

(15) Ryu, H.; Murugavel, P.; Lee, J. H.; Chae, S. C.; Noh, T. W.; Oh, Y. S.; Kim, H. J.; Kim, K. H.; Jang, J. H.; Kim, M.; Bae, C.; Park, J.-G. *Applied Physics Letters* **2006**, *89*, 102907.

(16) Wan, J. G.; Wang, X. W.; Wu, Y. J.; Zeng, M.; Wang, Y.; Jiang, H.; Zhou, W. Q.; Wang, G. H.; Liu, J.-M. *Applied Physics Letters* **2005**, *86*, 122501.

(17) Ma, Y. G.; Cheng, W. N.; Ning, M.; Ong, C. K. *Applied Physics Letters* **2007**, *90*, 152911.

(18) Wu, T.; Zurbuchen, M. A.; Saha, S.; Wang, R.-V.; Streiffer, S. K.; Mitchell, J. F. *Physical Review B* **Apr. 2006**, *73*, 134416.

(19) Li, Z.; Gao, Y.; Yang, B.; Lin, Y.; Yu, R.; Nan, C.-W. *Journal of the American Ceramic Society* **Apr. 2011**, *94*, 1060–1066.

(20) Chen, W.; Zhu, W.; Chen, X.; Wang, Z. *Journal of the American Ceramic Society* **Mar. 2010**, *93*, 796–799.

(21) Ding, L.-Y.; Wu, F.-X.; Chen, Y.-B.; Gu, Z.-B.; Zhang, S.-T. *Applied Surface Science* **Feb. 2011**, *257*, 3840–3842.

(22) Tahmasebi, K.; Barzegar, A.; Ding, J.; Herng, T. S.; Huang, L.; Huang, A.; Shannigrahi, S. *Thin Solid Films* **June 2013**, *537*, 76–79.

(23) Basu, S.; Babu, K. R.; Choudhary, R. N. P. *Materials Chemistry and Physics* **Feb. 2012**, *132*, 570–580.

(24) Ortega, N.; Bhattacharya, P.; Katiyar, R. S.; Dutta, P.; Manivannan, A.; Seehra, M. S.; Takeuchi, I.; Majumder, S. B. *Journal of Applied Physics* **2006**, *100*, 126105.

(25) Liu, M.; Li, X.; Lou, J.; Zheng, S.; Du, K.; Sun, N. X. *Journal of Applied Physics* **2007**, *102*, 083911.

(26) Wan, J.-g.; Zhang, H.; Wang, X.; Pan, D.; Liu, J.-m.; Wang, G. *Applied Physics Letters* **2006**, *89*, 122914.

(27) Ogawa, M. *Journal of the American Chemical Society* **Aug. 1994**, *116*, 7941–7942.

(28) Brinker, C. J.; Lu, Y.; Sellinger, A.; Fan, H. *Advanced Materials* **May 1999**, *11*, 579–585.

(29) Brezesinski, T.; Groenewolt, M.; Gibaud, A.; Pinna, N.; Antonietti, M.; Smarsly, B. *Advanced Materials* **Sept. 2006**, *18*, 2260–2263.

(30) Mamak, M.; Coombs, N.; Ozin, G. *Advanced Materials* **Feb. 2000**, *12*, 198–202.

(31) Yang, P. *Science* **Dec. 1998**, *282*, 2244–2246.

(32) Fattakhova-Rohlfing, D.; Brezesinski, T.; Rathouský, J.; Feldhoff, A.; Oekermann, T.; Wark, M.; Smarsly, B. M. *Advanced Materials* **Nov. 2006**, *18*, 2980–2983.

(33) Quickel, T. E.; Schelhas, L. T.; Farrell, R. A.; Petkov, N.; Le, V. H.; Tolbert, S. H. *Nature Communications* **2015**, *6*, 6562.

(34) Quickel, T. E.; Le, V. H.; Brezesinski, T.; Tolbert, S. H. *Nano letters* **Aug. 2010**, *10*, 2982–8.

(35) George, S. M. *Chemical Reviews* **Jan. 2010**, *110*, 111–131.

(36) Choi, J. H.; Zhang, F.; Perng, Y.-C.; Chang, J. P. *Journal of Vacuum Science & Technology B: Microelectronics and Nanometer Structures* **2013**, *31*, 012207.

(37) Zhang, F.; Perng, Y.-C.; Choi, J. H.; Wu, T.; Chung, T.-K.; Carman, G. P.; Locke, C.; Thomas, S.; Saddow, S. E.; Chang, J. P. *Journal of Applied Physics* **2011**, *109*, 124109.

(38) Sugiyama, O.; Murakami, K.; Kaneko, S. *Journal of the European Ceramic Society.* **2004**, *24*, 1157–1160.

(39) Baklanov, M. R.; Mogilnikov, K. P.; Polovinkin, V. G.; Dultsev, F. N. *Journal of Vacuum Science & Technology B: Microelectronics and Nanometer Structures* **2000**, *18*, 1385.

(40) Gregg, S. J.; Sing, K. S. W., *Adsorption, Surface Area, and Porosity*, 2nd ed.; Academic Press: London, New York, 1982.

(41) Benedetto, J. M.; Moore, R. A.; McLean, F. B. *Journal of Applied Physics* **1994**, *75*, 460.

(42) Jenkins, I. G.; Song, T. K.; Madhukar, S.; Prakash, A. S.; Aggarwal, S.; Ramesh, R. *Applied Physics Letters* **1998**, *72*, 3300–3302.

(43) Dunn, S. *Integrated Ferroelectrics* **Sept. 2003**, *59*, 1505–1512.

(44) Choi, T.; Kim, J.-S.; Park, B. H.; Shin, H.; Lee, J. *Ferroelectrics* **July 2006**, *336*, 271–277.

(45) Zhang, S. et al. *Physical Review Letters* **Mar. 2012**, *108*, 137203.

(46) Yang, J. J.; Zhao, Y. G.; Tian, H. F.; Luo, L. B.; Zhang, H. Y.; He, Y. J.; Luo, H. S. *Applied Physics Letters* **2009**, *94*, 212504.

(47) Allgaier, J.; Poppe, A.; Willner, L.; Richter, D. *Macromolecules* **Mar. 1997**, *30*, 1582–1586.

(48) Hillmyer, M. A.; Bates, F. S. *Macromolecules* **Jan. 1996**, *29*, 6994–7002.

Chapter 3

Strain transfer in porous multiferroic composites of cobalt ferrite and lead zirconate titanate

Abraham N. Buditama, Kevin Fitzell, Diana Chien, C. Ty Karaba, Hye Yeon Kang, Shauna Robbennolt, Jane P. Chang, and Sarah H. Tolbert

Abstract

This manuscript examines the mechanism of strain-coupling in a multiferroic composite of mesoporous cobalt ferrite (CFO), conformally filled with lead zirconate titanate (PZT). We find that when the composites are electrically poled, remanent strain from the piezoelectric PZT layer can be transferred to the magnetostrictive CFO layer. X-ray diffraction shows that this strain transfer is greatest in the most porous samples, in agreement with magnetometry measurements, which show the greatest change in sample saturation magnetization in the most porous samples. Strain analysis shows that porosity both accommodates greater lattice strain and mitigates the effects of substrate clamping in thin film strain-coupled composites.

Introduction

Multiferroics are materials that simultaneously exhibit more than one ferroic order parameter such as ferromagnetism or ferroelectricity; they are of interest because of their potential nanoscale

applications in a wide range of nanoscale devices.[1–3] In particular, magnetoelectric multiferroic materials couple a magnetic and an electric polarization, but single-phase materials that show this property are rare.[4] Composite materials, however, offer another route to magnetoelectric behavior. Such materials generally use strain-coupling and typically consist of layers of piezoelectric and magnetostrictive materials. As an electric field is applied to the composite, the piezoelectric is strained, and this strain is transferred to the magnetostrictive material, which in turn affects the magnetization. This coupling allows the magnetization to be controlled by applied electric fields, and vice versa.[5–13] Because this technique requires intimate coupling between the two phases, numerous synthetic methods and architectures of strain-coupled multiferroics have been investigated in the literature, including sequentially deposited two-dimensional stacks, spontaneously phase-separated nanopillar arrays, and other three-dimensional arrangements.[7–16]

We have recently shown that porosity is an important control parameter in the synthesis of multiferroic composites.[13] In our previous work, a mesoporous, magnetostrictive cobalt ferrite ($CoFe_2O_4$ or CFO) film was filled using atomic layer deposition (ALD) with piezoelectric lead zirconate titanate ($PbZr_xTi_{1-x}O_3$ or PZT). The result was an interconnected, three-dimensional network containing both CFO and PZT. The final porosity in such a composite can be controlled by the initial pore size, which is determined by the polymer template used in the synthesis of the initial mesoporous CFO, and the thickness of the deposited PZT layer. Our results showed that the final composite porosity was correlated to a change in magnetic saturation that could be achieved upon electrical poling. It was hypothesized that this correlation was due to a link between porosity and mechanical flexibility of the composite, but no direct evidence for that hypothesis was obtained. Here we examine the mechanism of magnetoelectricity in these thin film composites by depositing a range of thicknesses of PZT in the mesoporous CFO framework and measuring the resultant strain in the CFO framework.

The mesoporous CFO framework was synthesized using block copolymer–templating of sol-gel films, a technique that has been used to produce a wide range of metal oxide materials of varying nanoarchitectures.[17–26] The CFO sol was templated with an amphiphilic diblock copolymer that

forms micelles in solution. As the solution is deposited, the micelles self-assemble into periodic structures within the film. Upon pyrolysis, the polymer is removed, leaving a stable porous network of CFO.

This porous film is then conformally coated with PZT using ALD, which grants uniformity over the entire structure because this technique obtains layer-by-layer growth through a self-limiting surface reaction. Alternating pulses of gaseous precursors completely saturate all available surface sites, allowing conformal deposition over the entire porous network. ALD also allows for fine control over the thickness deposited, and thus over the final porosity of the composite material. This method thus provides new functionality compared to composites in the literature, which thus far have been dense structures that lack porosity. Here we aim to use high-resolution X-ray diffraction on films as a function of *ex situ* poling field to explore the mechanisms of strain coupling in this porous composite.

Experimental

Synthetic details for both CFO and PZT have been discussed previously.[13,17] Briefly, poly((ethylene-*co*-propylene)-*block*-poly(ethylene oxide) with a mass ratio of PEP(3900)-*b*-PEO(4000) was used to template a sol based on nitrate salts of Co and Fe. PZT was deposited via ALD using $Pb(TMHD)_2$, $Ti(O\text{-}i\text{-}Pr)_2(TMHD)_2$, and $Zr(TMHD)_4$ as precursors. PZT was deposited at no more than 180 °C in an amorphous form and then crystallized into tetragonal PZT by rapid thermal annealing at 700 °C. Here the PZT layer thicknesses range from 3 nm to 10 nm.

The morphology and thickness of the nanocomposites was confirmed using a JEOL JSM-6700F field-emission scanning electron microscopy (FE-SEM). Ellipsometric porosimetry (EP) was performed on a Semilab PS-1100 in the spectral range of 1.24 eV to 4.5 eV. A UV-vis CCD detector adapted to a grating spectrograph analyzes the signals reflected by the sample from a 75 W Hamamatsu Xe lamp. Toluene was used as the adsorbent, and EP analysis was performed using the associated SEA software. Angular-dependent X-ray diffraction (XRD) was collected

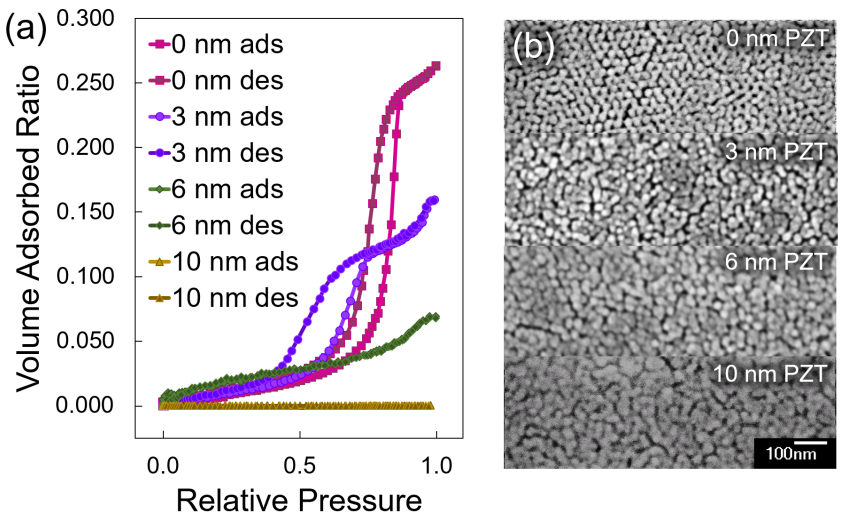

Figure 3.1: Ellipsometric porosimetry adsorption/desorption curves (a) show reduced porosity with increasing PZT thickness. Calculated porosity values are 26.0%, 15.3%, 6.6%, and 0.03%, respectively. SEM images (b) show gradual filling of the CFO framework. From the top, the CFO layer is filled with 0 nm, 3 nm, 6 nm, and 10 nm of PZT.

at the Stanford Synchrotron Radiation Laboratory (SSRL) using beamline 7-2 at wavelength of $\lambda = 0.9919$ Å and 1.0332 Å. Magnetic measurements were carried out on a Quantum Design MPMS 5T SQUID magnetometer with RSO detection.

Results and discussion

Because our previous work indicated the importance of residual porosity in multiferroic composites, we first characterized that porosity using ellipsometric porosimetry. EP adsorption/desorption curves for samples with various PZT layers (figure 3.1a) show that as thicker PZT layers are deposited, less toluene vapor is adsorbed. The samples with 0 nm and 3 nm of PZT show a distinct type IV isotherm, which signifies an interconnected porous network. The calculated porosity values are 26.0% for the 0 nm PZT sample, 15.3% for 3 nm, 6.6% for 6 nm, and 0.03% for 10 nm. The PZT in these as-deposited films are amorphous, but previous work[13] has shown that the PZT can be crystallized to the ferroelectric tetragonal phase. We find that redistribution of PZT in the pores can block the small necks in the structure, impeding toluene access to the pores. As a result,

SEM was used to characterize the samples after crystallization. SEM images of the samples with crystallized PZT layers (figure 3.1b), from top to bottom, show reduced porosity as thicker PZT layers are deposited. The unfilled CFO framework exhibits ordered porosity, which is distorted by grain growth upon annealing of the PZT layer. For this reason, the 10 nm sample still appears to be somewhat porous by SEM, even though access into the porous interior is stopped by pore necks that had been completely stoppered by PZT, as evidenced by the EP adsorption/desorption curves.

To determine the magnetoelectric coupling of these thin film composites, they were electrically poled ex situ with the electric field applied perpendicular to the sample surface (henceforth referred to as out-of-plane). The films were covered with a polyvinylidene chloride spacer with a thickness of 13 μm and physically sandwiched between two Al electrodes 1.28 cm in diameter. The nanocomposite was electrically poled for 10 min with applied electric fields ranging from 0 MV m^{-1} to 1.42 MV m^{-1}. As such, the strains and polarizations explored in this paper are remanent ones. While it is true that much of the strains and polarizations will be lost upon removal of the applied field, the remanent polarization stabilizes within milliseconds and can be assumed to be constant throughout the measurement.[27,28]

Magnetization measurements show a decrease in out-of-plane saturation magnetization upon electrical poling that is correlated with porosity of the composite (figure 3.2). The sample with the thinnest PZT layer shows the largest change in saturation magnetization, and the sample with the thickest PZT shows hardly any change. Because polarization in ultrathin PZT is known to decrease with thickness,[29,30] this trend is likely due to the mechanical properties of the porous composite, rather than any favorable change in the PZT itself. The films with the thinnest PZT are also the ones with the highest porosity and therefore the greatest mechanical flexibility, as pore flexion accommodates significant strain changes in the material.[17,18,31]

The role of porosity in magnetoelectric coupling is corroborated by strain analysis of the CFO layer. Synchrotron XRD was used to probe the differences in both out-of-plane and in-plane (parallel to the substrate) lattice spacings. The CFO{311} and PZT{200} peaks were relatively well resolved and were treated as representative of overall strain changes in both materials. Because

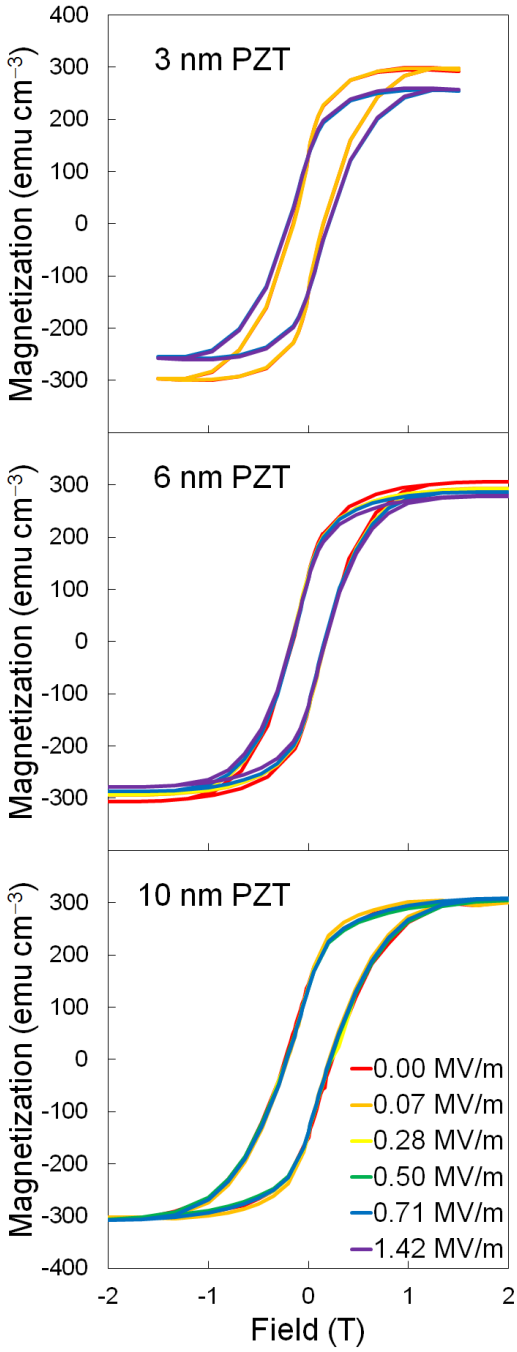

Figure 3.2: M–H loops of the CFO/PZT composites show a reduced change in magnetization saturation upon application of an electric field in less porous samples. The direction of the applied electric field and the measured magnetization were both out-of-plane (perpendicular to the sample substrate).

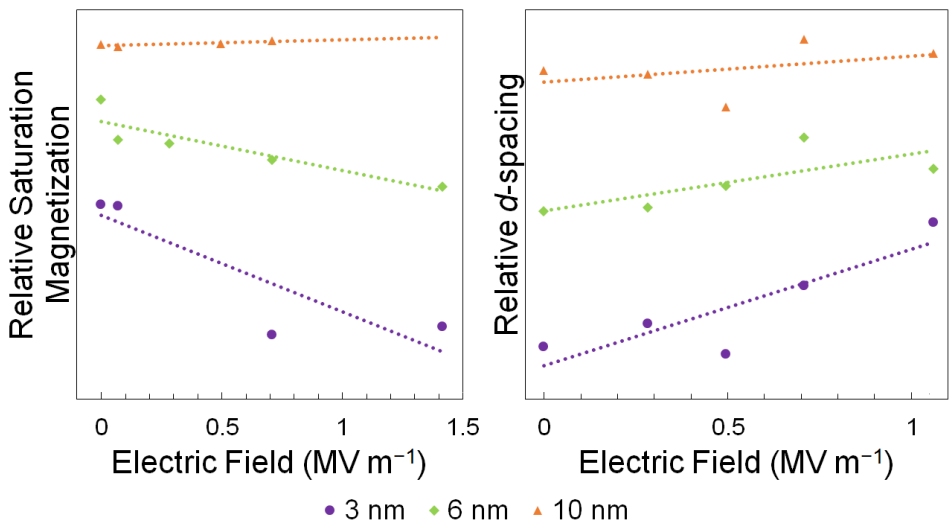

Figure 3.3: Samples with less PZT and thus greater porosity show greater change for both CFO out-of-plane saturation magnetization (a) and strain (b). The saturation magnetization is obtained from the data shown in figure 2. The strain is calculated by measuring the peak shifts in the XRD spectra of the CFO{311} peak positions. In both cases, the y-axes have been offset to show the difference between the samples.

these films consist of polycrystalline CFO and PZT with no preferred orientation with respect to the substrate, any lattice plane can be used to report on the overall strain state of the material. As shown in figure 3.3 and expected based on the magnetization data, the CFO{311} out-of-plane lattice spacing increased upon *ex situ* electrical poling, and the magnitude of the change was directly correlated to the porosity of the composite: as the porosity decreased, the strain transferred upon electrical poling also decreased (figure 3.3). CFO exhibits negative magnetostriction, and so the decrease in out-of-plane tension directly corresponds to the reduced magnitude of change in out-of-plane magnetization saturation.

Even though CFO is not a piezoelectric, it is strain-coupled to one, and so we can calculate the strains when $1\,\mathrm{MV\,m^{-1}}$ has been applied and then removed from the sample. While this strain is not a real piezoelectric coefficient, it relates a remanent strain to an *ex situ* electric field, and so we give it the symbol d'_{33}. Values of d'_{33} range from $d'_{33} = 590 \times 10^{-12}\,\mathrm{m\,V^{-1}}$ for the composite with the highest porosity (3 nm PZT), to $d'_{33} = 130 \times 10^{-12}\,\mathrm{m\,V^{-1}}$ for the composite with lowest porosity (10 nm PZT), which is comparable to true piezoelectric coefficients of PZT.[32,33] These

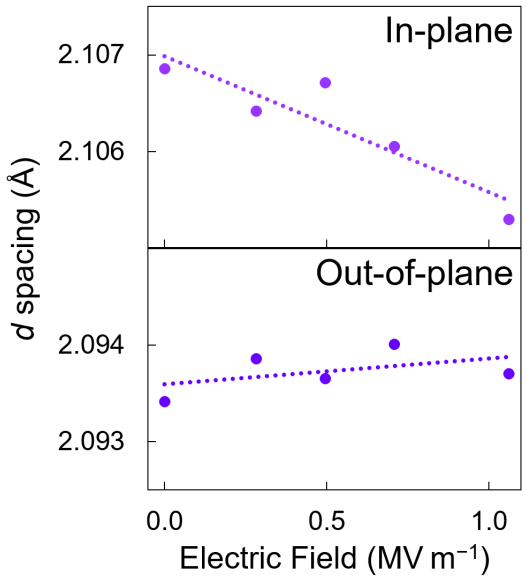

Figure 3.4: The magnitudes of the in-plane and out-of-plane PZT strains are comparable to those of the CFO. PZT strains are calculated by measuring the shifts in the XRD spectra of the PZT200 peak positions.

values demonstrate more than a fourfold reduction of strain transferred when porosity is removed from the sample. Again, we emphasize that these calculated values are not true piezoelectric coefficients because they relate the remanent strain to an *ex situ* applied field instead of the instantaneous strain to an *in situ* field; the instantaneous piezoelectric coefficient should be higher indeed.

No significant change upon electrical poling was found in the in-plane saturation magnetization nor in the CFO in-plane strain. The CFO framework is covalently bound to a Si wafer and is unable to move because of substrate clamping. Because its strain is unchanged, the CFO in-plane magnetization is also unchanged. However, the PZT layer is deposited onto the CFO framework itself, and as such is not constrained by the substrate. As the PZT deforms due to the out-of-plane electric field, strain can be expressed as out-of-plane tension or in-plane compression. This strain is transferred to the clamped CFO framework and can be expressed only as the aforementioned out-of-plane tension. Interestingly, analysis of PZT strain reveals contribution from both in-plane compression and out-of-plane tension. Similar d' coefficients calculated for PZT show comparable

strains to the CFO, but with more noise because the diffraction is weaker. The greatest PZT strains are in the most porous sample (3 nm PZT) and are shown in figure 3.4. The data show changes in both in-plane and out-of-plane lattice constants and demonstrate that the PZT is not at all substrate clamped. The strains are calculated to be $d'_{31} = -670 \times 10^{-12}\,\mathrm{m\,V^{-1}}$ in-plane and $d'_{33} = 130 \times 10^{-12}\,\mathrm{m\,V^{-1}}$ out-of-plane, values that are comparable to that of the CFO, suggesting that much of the strain had indeed been transferred. Thus, from strain analysis of this free PZT layer, we see that three-dimensional porosity has an advantage over traditional two-dimensional structures where multiple layers are clamped together to the substrate. In a three-dimensional structure like this one, the pore-filling material can remain unclamped if sufficient residual porosity is retained.

Conclusion

Overall, these experiments have allowed us to explore the mechanism of strain-coupling in porous magnetoelectric CFO/PZT composites. These thin films are composed of a templated mesoporous CFO framework, which is subsequently filled by ALD PZT of varying thicknesses. As the samples are electrically poled out-of-plane, X-ray diffraction shows that the piezoelectric PZT layer may exhibit both out-of-plane tension and in-plane compression. This strain is transferred to the magnetostrictive CFO layer, which results in decreased out-of-plane saturation magnetization as measured by SQUID magnetometry. The strain transfer is greatest in samples with the greatest porosity, as pore flexion accommodates greater strains in the material. This porous architecture thus offers not only greater mechanical flexibility than traditional composite architectures, but also mitigates the effects of substrate clamping for the ALD layer. Perhaps more importantly, the observation of in-plane compression in what could have been a clamped PZT layer provides insight into the use of porosity in the design of future porous multiferroic composites.

Acknowledgments

This work was supported by the NSF Nanosystems Engineering Research Center for Translational Applications of Nanoscale Multiferroic Systems (TANMS) under Cooperative Agreement Award EEC-1160504. This work made use of the UCLA Molecular Instrumentation Center (MIC). This manuscript contains data collected at the Stanford Synchrotron Radiation Lightsource (SSRL), experimental station 7-2. SSRL and the SLAC National Accelerator Laboratory are supported by the U.S. Department of Energy, Office of Science, Office of Basic Energy Sciences under Contract No. DE-AC02-76SF00515.

References

(1) Spaldin, N. A.; Fiebig, M. *Science* **July 2005**, *309*, 391–2.

(2) Nan, C.-W.; Bichurin, M. I.; Dong, S.; Viehland, D.; Srinivasan, G. *Journal of Applied Physics* **2008**, *103*, 031101.

(3) Vaz, C. A. F.; Hoffman, J.; Ahn, C. H.; Ramesh, R. *Advanced Materials* **Apr. 2010**, *22*, 2900–2918.

(4) Hill, N. A. *The Journal of Physical Chemistry B* **July 2000**, *104*, 6694–6709.

(5) Zhou, J.-p.; He, H.-c.; Shi, Z.; Liu, G.; Nan, C.-W. *Journal of Applied Physics* **Nov. 2006**, *100*, 094106.

(6) Chen, W.; Zhu, W.; Chen, X.; Wang, Z. *Journal of the American Ceramic Society* **Mar. 2010**, *93*, 796–799.

(7) Wan, J. G.; Wang, X. W.; Wu, Y. J.; Zeng, M.; Wang, Y.; Jiang, H.; Zhou, W. Q.; Wang, G. H.; Liu, J.-M. *Applied Physics Letters* **2005**, *86*, 122501.

(8) Sim, C. H.; Pan, A. Z. Z.; Wang, J. *Journal of Applied Physics* **2008**, *103*, 124109.

(9) Ding, L.-Y.; Wu, F.-X.; Chen, Y.-B.; Gu, Z.-B.; Zhang, S.-T. *Applied Surface Science* **Feb. 2011**, *257*, 3840–3842.

(10) Xie, S.; Ma, F.; Liu, Y.; Li, J. *Nanoscale* **Aug. 2011**, *3*, 3152–8.

(11) Tahmasebi, K.; Barzegar, A.; Ding, J.; Herng, T. S.; Huang, A.; Shannigrahi, S. *Materials and Design* **2011**, *32*, 2370–2373.

(12) Tahmasebi, K.; Barzegar, A.; Ding, J.; Herng, T. S.; Huang, L.; Huang, A.; Shannigrahi, S. *Thin Solid Films* **June 2013**, *537*, 76–79.

(13) Chien, D.; Buditama, A. N.; Schelhas, L. T.; Kang, H. Y.; Robbennolt, S.; Chang, J. P.; Tolbert, S. H. *Applied Physics Letters* **2016**, *109*, 112904.

(14) Zheng, H. et al. *Science* **Jan. 2004**, *303*, 661–3.

(15) Ortega, N.; Bhattacharya, P.; Katiyar, R. S.; Dutta, P.; Manivannan, A.; Seehra, M. S.; Takeuchi, I.; Majumder, S. B. *Journal of Applied Physics* **2006**, *100*, 126105.

(16) Aimon, N. M.; Choi, H. K.; Sun, X. Y.; Kim, D. H.; Ross, C. A. *Advanced Materials* **May 2014**, *26*, 3063–3067.

(17) Quickel, T. E.; Le, V. H.; Brezesinski, T.; Tolbert, S. H. *Nano letters* **Aug. 2010**, *10*, 2982–8.

(18) Quickel, T. E.; Schelhas, L. T.; Farrell, R. A.; Petkov, N.; Le, V. H.; Tolbert, S. H. *Nature Communications* **2015**, *6*, 6562.

(19) Ortel, E.; Reier, T.; Strasser, P.; Kraehnert, R. *Chemistry of Materials* **July 2011**, *23*, 3201–3209.

(20) Fang, J.; Kang, C. B.; Huang, Y.; Tolbert, S. H.; Pilon, L. *The Journal of Physical Chemistry C* **June 2012**, *116*, 12926–12933.

(21) Rauda, I. E.; Buonsanti, R.; Saldarriaga-Lopez, L. C.; Benjauthrit, K.; Schelhas, L. T.; Stefik, M.; Augustyn, V.; Ko, J.; Dunn, B.; Wiesner, U.; Milliron, D. J.; Tolbert, S. H. *ACS Nano* **2012**, *6*, 6386–6399.

(22) Hsueh, H.-Y.; Yao, C.-T.; Ho, R.-M. *Chem. Soc. Rev.* **2015**, *44*, 1974–2018.

(23) Brinker, C. J.; Lu, Y.; Sellinger, A.; Fan, H. *Advanced Materials* **May 1999**, *11*, 579–585.

(24) Brezesinski, T.; Groenewolt, M.; Gibaud, A.; Pinna, N.; Antonietti, M.; Smarsly, B. *Advanced Materials* **Sept. 2006**, *18*, 2260–2263.

(25) Yang, P. *Science* **Dec. 1998**, *282*, 2244–2246.

(26) Fattakhova-Rohlfing, D.; Brezesinski, T.; Rathouský, J.; Feldhoff, A.; Oekermann, T.; Wark, M.; Smarsly, B. M. *Advanced Materials* **Nov. 2006**, *18*, 2980–2983.

(27) Benedetto, J. M.; Moore, R. A.; McLean, F. B. *Journal of Applied Physics* **1994**, *75*, 460.

(28) Jenkins, I. G.; Song, T. K.; Madhukar, S.; Prakash, A. S.; Aggarwal, S.; Ramesh, R. *Applied Physics Letters* **1998**, *72*, 3300–3302.

(29) Dunn, S. *Integrated Ferroelectrics* **Sept. 2003**, *59*, 1505–1512.

(30) Choi, T.; Kim, J.-S.; Park, B. H.; Shin, H.; Lee, J. *Ferroelectrics* **July 2006**, *336*, 271–277.

(31) Kirsch, B. L.; Chen, X.; Richman, E. K.; Gupta, V.; Tolbert, S. H. *Advanced Functional Materials* **Aug. 2005**, *15*, 1319–1327.

(32) Jaffe, H.; Berlincourt, D. A. *Proceedings of the IEEE* **1965**, *53*, 1372–1386.

(33) Guo, R.; Cross, L. E.; Park, S.-E.; Noheda, B.; Cox, D. E.; Shirane, G. *Physical review letters* **June 2000**, *84*, 5423–6.

Chapter 4

Structure and morphology of lead zirconate titanate thin films prepared by sol-gel methods

Abraham N. Buditama and Sarah H. Tolbert

Abstract

Sol-gel processing is a cost-effective and scalable method to produce piezoelectric thin films of lead zirconate titanate ($PbZr_xTi_{1-x}O_3$ or PZT). PZT precursor solutions are deposited onto platinized silicon substrates via dip coating or spin coating. Final thicknesses of the films are controlled by the speeds of the solution deposition process and by iterating. Sol-gel processing additionally allows for block copolymer templating, where polymer micelles self-assemble into an ordered nanoarchitecture within the PZT film, leaving a mesoporous structure after pyrolysis. Finally, orientation of the PZT films can be controlled by pre-crystallization heating conditions. Each of these parameters are tunable and allow control over the final structure and morphology of the film, allowing reliable fabrication of PZT thin films via sol-gel processing.

Introduction

Piezoelectric thin films find much use in memory, micro-electro-mechanical systems (MEMS), and other devices,[1–4] and of these materials, lead zirconate titanate ($PbZr_xTi_{1-x}O_3$ or PZT) is one of the

highest-performing and most well-studied. Despite incorporating toxic Pb, PZT enjoys continued interest in the literature due to its significant room-temperature piezoelectric properties. A solid solution of lead titanate ($PbTiO_3$ or PT) and lead zirconate ($PbZrO_3$ or PZ), PZT's piezoelectric coefficient, permittivity, and a host of other factors reach their maximum at the morphotropic phase boundary (MPB), a composition of Zr : Ti = 52 : 48 that exists at a phase transition between PT's preferred tetragonal structure and PZ's rhombohedral.[4–6]

In addition to stoichiometric considerations, the piezoelectric coefficient and permittivity is known to be influenced by crystal orientation of the PZT films, with the longitudinal piezoelectric coefficient d_{33} greatest along the ⟨100⟩ directions.[6–10] (Miller indices in this work given according to the cubic perovskite structure.) Because of this, control over orientation of the PZT thin films is desired. These films are typically grown on platinized silicon substrates ($Si/SiO_2/Ti/Pt$), and they exhibit texturing generally either in the ⟨100⟩ or ⟨111⟩ directions. Control over orientation on these substrates have been attributed to various factors including Pb valence states,[11,12] the Zr : Ti ratio,[4,12] Ti content of the Pt layer,[13,14] heating conditions for crystallization,[14–16] the orientation of the Pt layer itself,[9] and the presence of oriented seed layers.[10]

Solution processing of materials is considerably cheaper and more scalable than other deposition techniques. Furthermore, solutions may be templated by amphiphilic block copolymers to produce porous films. The polymers form micelles in solution, which self-assemble into an ordered structure upon evaporation of the solvent. As the film is pyrolyzed, the inorganic materials form a rigid framework, while the polymer is pyrolyzed and removed, leaving a porous architecture that is tunable according to the properties of the polymer template.[17] Porosity enhances the mechanical flexibility of the film, and oxide thin films such as PZT often experience significant tension in the plane parallel to the substrate (in-plane) due to volume reduction upon material crystallization, limiting potential strains in the material. Porosity, however, has been shown to alleviate this tension, and in multiferroic materials like PZT, where the strain is coupled to an electric or magnetic polarization, porosity has even enhanced those properties.[18–20] In this work,

Temperature (°C)	60	80	130	180
Ramp/soak time (h)	init.	1 / 6	2 / 8	1 / 6

Table 4.1: A typical heating ramp for the calcination of block copolymer–templated thin films. The films are placed into the furnace at an initial 60 °C. Note that the last soak step may be extended indefinitely.

we report the structures and morphologies of dense and mesoporous PZT thin films synthesized by a dip coating method, as well dense, multilayer PZT films by a spin coating method.

Experimental

The amphiphilic diblock polymer used to template the PZT films was poly(butadiene (1,4 rich))-*block*-poly-(ethylene oxide), with a mass ratio of PBd(5500)-*b*-PEO(7500), purchased from Polymer Source. PZT solution may be templated by other block copolymers such as PEP-*b*-PEO, but templating by PBd-*b*-PEO leads to a more stable pore structure due to the polymer's higher pyrolyzation temperature.

A typical PZT precursor solution contains stoichiometric amounts of lead(II) acetate trihydrate ($Pb(CH_3CO_2)_2 \cdot 3\,H_2O$), zirconium(IV) propoxide ($Zr(OCH_2CH_2CH_3)_4$), and titanium(IV) ethoxide ($Ti(OC_2H_5)_4$), dissolved in 2-methoxyethanol to a concentration of 0.4 M. To account for PbO volatilization during annealing, an additional 10 mol% of Pb precursor is added,[21] along with 0.1 ml of glacial acetic acid per 0.15 g of PZT as a chelating agent.[22] Note that the Pb precursor is less soluble in 2-methoxyethanol compared to the Zr and the Ti, and so should be dissolved first. Additionally, the Zr and Ti precursors are quite viscous, and large batches of solution may minimize measurement errors.

For mesoporous thin films, once the PZT solution is homogeneous, a solution of 0.040 g of PBd-*b*-PEO in 1 ml of warm ethanol is added and allowed to clarify by magnetic stirring for 1 h. Films were dip coated from the solution onto Si wafers in a humidity-controlled chamber set at 10% to 20% relative humidity. A low humidity is ideal throughout the entirety of the process, from dip

coating to calcination. The withdrawal rate was usually near 2 mm s^{-1} but was varied depending on desired thickness. To form rigid inorganic/organic structures, the films were calcined in air according to table 4.1. Finally, the PZT is crystallized at 700 °C in air. A relatively fast heating ramp is preferred to limit grain growth, but a ramp that is too steep may result in thermal shock, causing µm-sized cracks. A typical ramp is approximately 60 s to 80 s.

The PZT solution used for multilayer depositions is identical to that used for the mesoporous films except for the addition of the block copolymer solution and the increase of the excess Pb precursor to 20 mol% to account for repeated firings. Spin coating is preferred for the fabrication of multilayer films because the films produced by the spin coating process are relatively flat. Uneven thicknesses from the dip coating process are magnified in an iterative process, resulting in poor control over the final thickness. However, dip coating offers much greater control over evaporation rates, which are essential for the polymer templating process.[17]

For multilayer films, the PZT precursor solution was spin coated with a SCS G3 spin coater (Specialty Coating Systems, Inc.) on the Pt/Ti/SiO_2/Si substrates at 4000 RPM for 60 s, followed by pyrolysis at 300°C for 1 min on a hot plate in air. After every four layers, a rapid thermal process was performed at 700°C for 1 min in air. Solution coating and firing were repeated to produce PZT thin films with 12 layers.[23,24] Dust contamination is a greater issue here compared to the dip coating process due to the iterative nature of this procedure, and so fabrication in clean rooms are especially recommended.

A JEOL JSM-6700F field emission scanning electron microscope (FE-SEM) was used to characterize the sample morphology. Grazing incidence wide angle X-ray scattering (GIWAXS) was collected at the Stanford Synchrotron Radiation Laboratory (SSRL) using beamline 11-3. P–E and I–V measurements were performed using a Radiant Technology Precision LC Materials Analyzer.

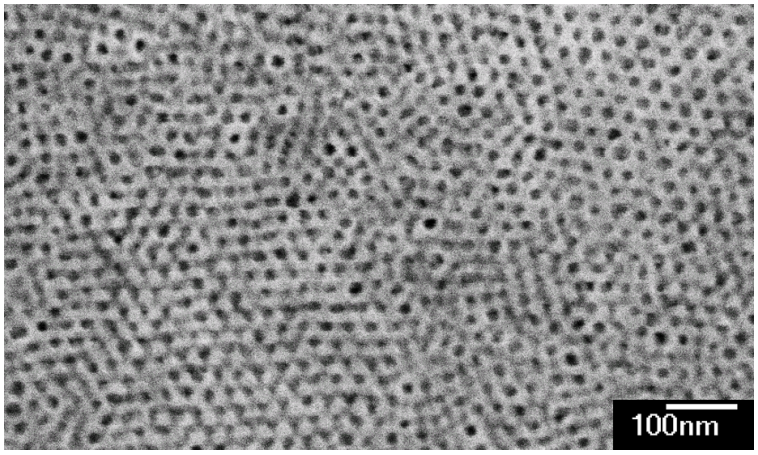

Figure 4.1: SEM shows ordered porosity in the PZT thin film.

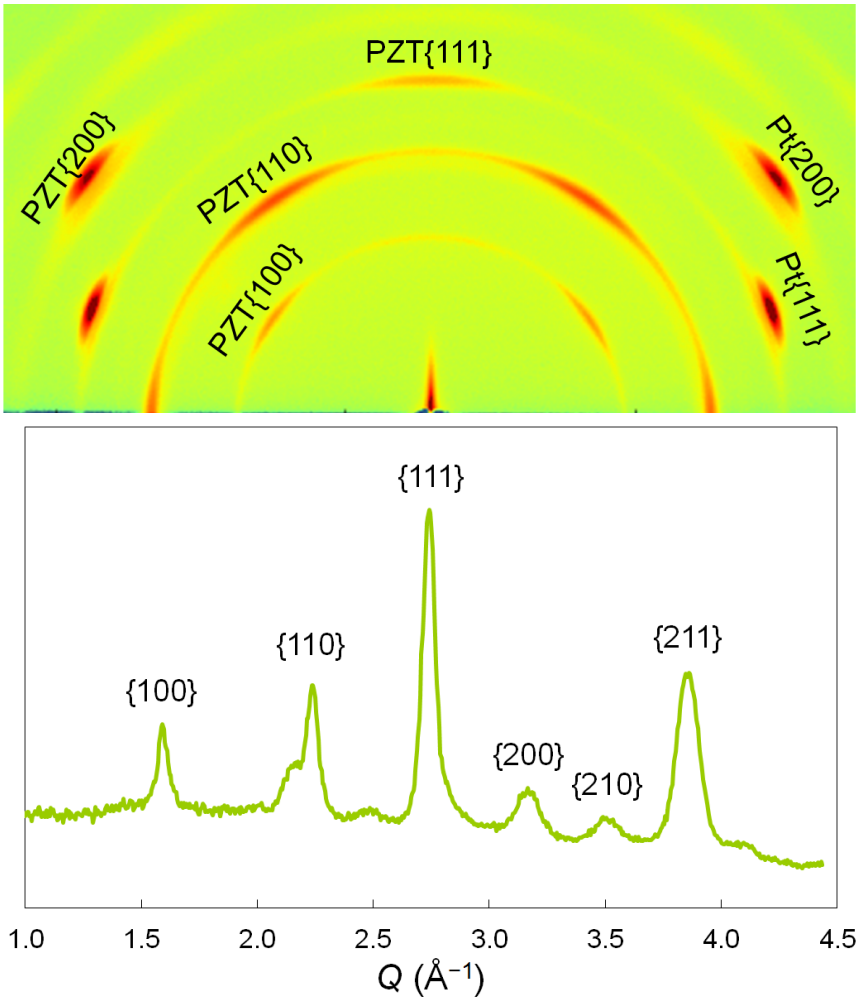

Figure 4.2: 2D GIWAXS and out-of-plane integration of the mesoporous PZT film show that the thin film is textured largely in the ⟨111⟩ direction.

Results and discussion

The nanoarchitecture of the porous PZT is shown by SEM (figure 4.1). The pore sizes range from 10 nm to 15 nm and are well-ordered, with a repeat distance of approximately 20 nm to 25 nm. The pore structure extends throughout the entire thickness of the film. X-ray diffraction confirms the crystallinity of the mesoporous PZT (figure 4.2). The small shoulder ($Q \approx 2.1$) to the left of the PZT{110} peak betrays a pyrochlore phase, but the sample is largely of the desired perovskite structure. The mesoporous PZT is textured along the the $\langle 111 \rangle$ directions, indicating that crystal orientation is propagated throughout the entire porous network. In the two-dimensional diffractogram, it can be seen that the $\{hhh\}$ peaks reach a maximum at azimuthal angle $\chi \approx 19^\circ, 90^\circ$, and 161°, the $\{hh0\}$ peaks at $\chi \approx 55^\circ$ and 125°, and the $\{h00\}$ peaks at $\chi \approx 35^\circ$ and 145°, as is expected from a $\langle 111 \rangle$-oriented cubic structure.

We note that the (111) peak of the PZT, and even of the much more strongly oriented Pt substrate, at $\chi = 90^\circ$ is less intense than other peaks at their maximal χ, which are angled further away from the out-of-plane direction. The geometry of a GIWAXS experiment is ideal for thin film characterization precisely because here the Bragg condition is met for lattice planes that are not parallel to the substrate, the number of which is not limited by the thin film geometry. This experiment was performed using a grazing incidence angle $\alpha = 3^\circ$, and as a result, the out-of-plane measurement here does not truly reflect the direction perpendicular from the substrate, but is tilted by an angle of $\theta - \alpha$, where θ is the Bragg angle. This tilt becomes trivial as $\chi \to n\pi, n \in \mathbb{Z}$, and as a result, very little of the strongly oriented Pt(111) is visible, and the out-of-plane PZT(111) peak appears less intense compared to other PZT peaks.

Porosity does not appear to impact the orientation of the film. Dense PZT films prepared by the same dip coating process show similar texturing in the $\langle 111 \rangle$ direction as the mesoporous films (figure 4.3). It is worth noting that in neither the dense nor the mesoporous films is the texturing perfectly epitaxial, as evidenced by the presence of rings in the two-dimensional diffractogram. Despite the PZT{111} matching perfectly with the Pt{111} substrate, the $\{h00\}$ faces are still

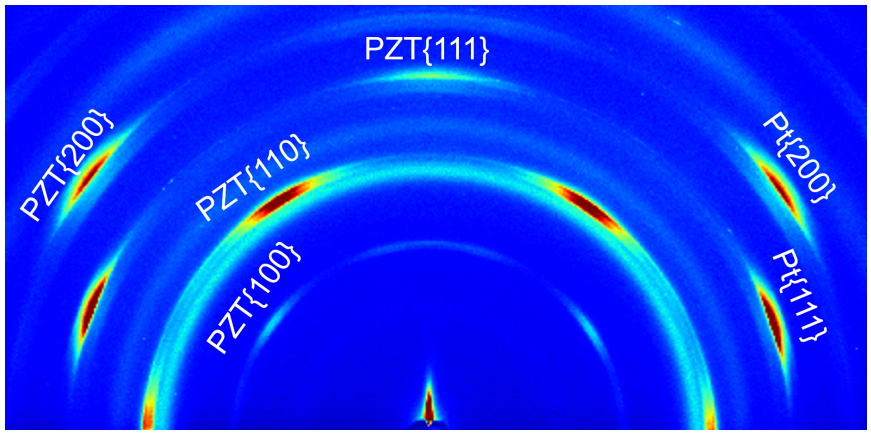

Figure 4.3: 2D GIWAXS and out-of-plane integration of the dense PZT film show that the thin film is textured largely in the ⟨111⟩ direction.

kinetically most favorable,[11,12,14] and this appeared to have disrupted the epitaxy enough to create some randomly oriented grains throughout the film.

On the other hand, multilayer films prepared by the spin coating process tend to be oriented along the ⟨100⟩ direction (figure 4.4). The two-dimensional diffractogram depicts the $\{h00\}$ peaks reaching a maximum at $\chi = 90^\circ$, the $\{hh0\}$ peaks at $\chi = 45^\circ$ and 135°, and the $\{hhh\}$ peaks at $\chi \approx 35^\circ$ and 145°, as is expected from a ⟨100⟩-oriented cubic structure. Like the dip coated films, the texturing is not fully epitaxial, as evidenced by rings in the two-dimensional diffractogram. The difference in orientation between the two synthetic methods is attributed to the difference in pre-crystallization heating conditions between the two methods. The dip coated films were exposed to low heat over a long period of time because polymer-templated films require time for the polymer micelles to self-assemble into ordered structures. In contrast, the spin coated films, which were never templated, are quickly calcined at 300 °C, giving enough energy for PZT crystals to nucleate along ⟨100⟩ directions. Altering the Pb content, humidity, or thickness of Pt layer appear to have minimal effects on PZT orientation.

The PZT films demonstrate reasonable ferroelectric properties (figure 4.5). The dense films tend to be less leaky than the porous films, which have greater surface area and thus greater conductivity along surface sites.[25] Even so, PZT films with high surface area exhibit greater flexibility and

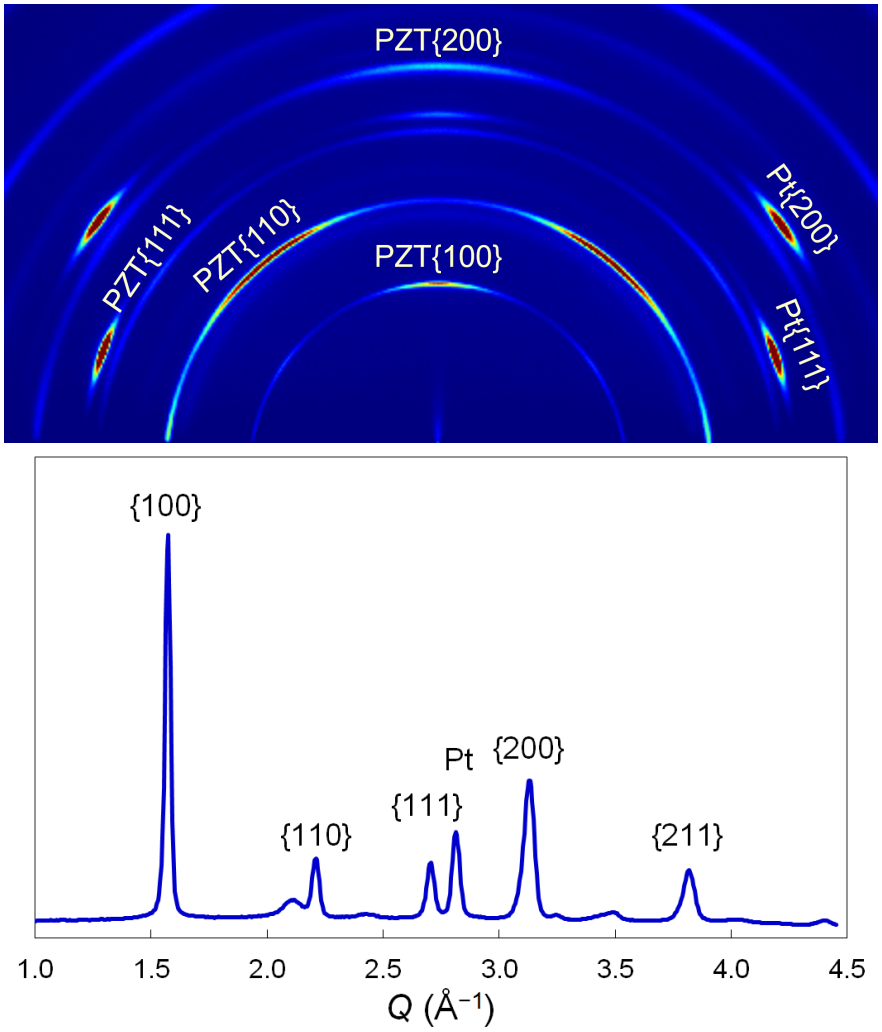

Figure 4.4: 2D GIWAXS and out-of-plane integration of dense, multilayer PZT show that the thin film is textured largely in the ⟨100⟩ direction.

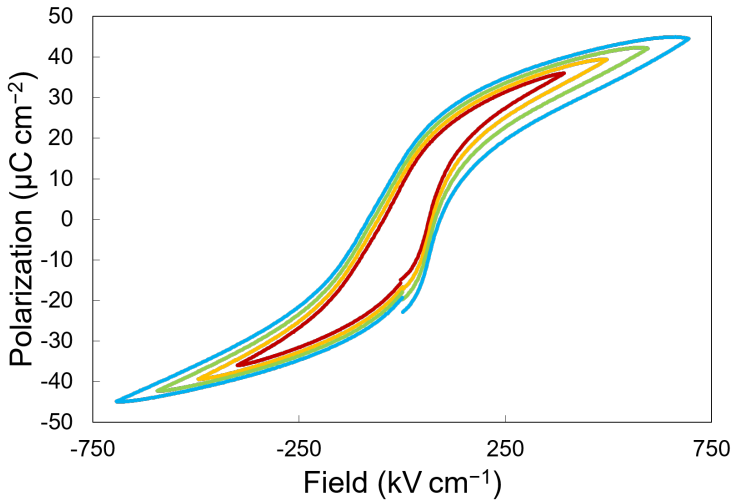

Figure 4.5: P–E measurements of dense PZT film show ferroelectric character.

thus better piezoelectric capability when complemented with high-dielectric materials such as magnetic oxides.[20] Thus, PZT thin films are excellent candidates for materials in strain-coupled magnetoelectric composites.

Conclusion

Sol-gel methods remain a cost-effective and scalable method to produce PZT thin films of varying thicknesses, morphologies, and orientation. High-quality films with thicknesses of 10^{-7} m are fabricated by an iterative spin coating method, whereas films with controlled nanoarchitectures are produced by a dip coating method. The orientation of these films may be controlled by their pre-crystallization heating conditions, with ⟨100⟩-oriented films requiring quick exposures to relatively high temperatures. Texturing of these films propagate through the nanoarchitecture, resulting in porous, oriented thin films. The parameters given here are highly tunable, allowing great control over the final structure and morphology of the PZT thin films.

References

(1) Scott, J. F. *Science* **Feb. 2007**, *315*, 954–959.

(2) Dawber, M.; Rabe, K. M.; Scott, J. F. *Reviews of Modern Physics* **Oct. 2005**, *77*, 1083–1130.

(3) Tsymbal, E. Y.; Gruverman, A. *Nature Materials* **May 2013**, *12*, 602–604.

(4) Kim, S.-H.; Yang, J.-S.; Koo, C. Y.; Yeom, J.-H.; Yoon, E.; Hwang, C. S.; Park, J.-S.; Kang, S.-G.; Kim, D.-J.; Ha, J. *Japanese Journal of Applied Physics* **Sept. 2003**, *42*, 5952–5955.

(5) Guo, R.; Cross, L. E.; Park, S.-E.; Noheda, B.; Cox, D. E.; Shirane, G. *Physical review letters* **June 2000**, *84*, 5423–6.

(6) Du, X.-h.; Zheng, J.; Belegundu, U.; Uchino, K. *Applied Physics Letters* **1998**, *72*, 2421.

(7) Du, X.-h.; Belegundu, U.; Uchino, K. *Japanese Journal of Applied Physics* **Sept. 1997**, *36*, 5580–5587.

(8) Lian, L.; Sottos, N. R. *Journal of Applied Physics* **2000**, *87*, 3941.

(9) Kim, S.-h.; Park, D.-Y.; Woo, H.-J.; Lee, D.-S.; Ha, J.; Seong Hwang, C.; Shim, I.-B.; Kingon, A. *Thin Solid Films* **Sept. 2002**, *416*, 264–270.

(10) Gong, W.; Li, J.-F.; Chu, X.; Gui, Z.; Li, L. *Journal of Applied Physics* **2004**, *96*, 590.

(11) Brooks, K. G.; Reaney, I. M.; Klissurska, R.; Huang, Y.; Bursill, L.; Setter, N. *Journal of Materials Research* **Oct. 1994**, *9*, 2540–2553.

(12) Cheng, J.; Luo, L.; Meng, Z. In *Proceedings of the 6th International Conference on Properties and Applications of Dielectric Materials*, IEEE: 2000; Vol. 2, pp 930–934.

(13) Muralt, P.; Maeder, T.; Sagalowicz, L.; Hiboux, S.; Scalese, S.; Naumovic, D.; Agostino, R. G.; Xanthopoulos, N.; Mathieu, H. J.; Patthey, L.; Bullock, E. L. *Journal of Applied Physics* **1998**, *83*, 3835.

(14) Willems, G. J.; Wouters, D. J.; Maes, H. E.; Nouwen, R. *Integrated Ferroelectrics* **Feb. 1997**, *15*, 19–28.

(15) Law, C. W.; Tong, K. Y.; Li, J. H.; Li, K. *Thin Solid Films* **1998**, *335*, 220–224.

(16) Huang, Z.; Zhang, Q.; Whatmore, R. W. *Journal of Materials Science Letters* **1998**, *7*, 1157–1159.

(17) Brinker, C. J.; Lu, Y.; Sellinger, A.; Fan, H. *Advanced Materials* **May 1999**, *11*, 579–585.

(18) Quickel, T. E.; Le, V. H.; Brezesinski, T.; Tolbert, S. H. *Nano letters* **Aug. 2010**, *10*, 2982–8.

(19) Reitz, C.; Leufke, P. M.; Hahn, H.; Brezesinski, T. *Chemistry of Materials* **Mar. 2014**, *26*, 2195–2202.

(20) Chien, D.; Buditama, A. N.; Schelhas, L. T.; Kang, H. Y.; Robbennolt, S.; Chang, J. P.; Tolbert, S. H. *Applied Physics Letters* **2016**, *109*, 112904.

(21) Zhu, C.; Yong, Z.; Chentao, Y.; Bangchao, Y. *Applied Surface Science* **Nov. 2006**, *253*, 1500–1505.

(22) Schwartz, R. W. *Chemistry of Materials* **Nov. 1997**, *9*, 2325–2340.

(23) Bastani, Y.; Schmitz-Kempen, T.; Roelofs, A.; Bassiri-Gharb, N. *Journal of Applied Physics* **2011**, *109*, 014115.

(24) Bastani, Y.; Bassiri-Gharb, N. *Acta Materialia* **Feb. 2012**, *60*, 1346–1352.

(25) Scott, J. F.; Araujo, C. A.; Melnick, B. M.; McMillan, L. D.; Zuleeg, R. *Journal of Applied Physics* **2009**, *70*, 382–388.

Chapter 5

The conductivity mechanism and an improved C–V model of ferroelectric PZT thin film

K. Liang, A. Buditama, D. Chien, J. Cui, P. L. Cheung, S. Goljahi, S. H. Tolbert, J. P. Chang, and C. S. Lynch

Abstract

A dense, homogeneous, and crack-free ferroelectric PZT thin film with ⟨100⟩-preferred orientation was produced using the sol-gel method. The volume fraction $\alpha_{(100)}$ of ⟨100⟩-oriented grains in the PZT film was calculated [$\alpha_{(100)} \approx 80\%$] from XRD of the PZT thin film and powder. The PZT thin film exhibits an open polarization vs. electric field loop and a low leakage current density from $10 \times 10^{-8}\,\mathrm{A\,cm^{-2}}$ to $10 \times 10^{-7}\,\mathrm{A\,cm^{-2}}$. The electrical conduction data were fit to a Schottky-emission model with deep traps from $100\,\mathrm{kV\,cm^{-1}}$ to $250\,\mathrm{kV\,cm^{-1}}$. A modified capacitance model was introduced that adds electrical domain capacitance based on a metal-ferroelectric-metal (MFM) system with Schottky contacts. The model reproduces the observed non-linear capacitance vs. voltage behavior of the film.

Introduction

Thin film ferroelectrics with the perovskite structure have applications in nonvolatile memory, piezoelectric devices, electro-optics, and micro-mechanical systems.[1–4] The control of bistable and switchable polarization states in ferroelectrics underlies many of these applications. The fast and electrically switchable polarization of lead zirconate titanate [$Pb(Zr_{1-x}Ti_x)O_3$, PZT] has been extensively investigated.[5–8] Ferroelectric PZT thin films with compositions close to the morphotropic phase boundary (MPB) [$Pb(Zr_{0.52}Ti_{0.48})O_3$] exhibit enhanced properties.[9,10] The current vs. voltage (I–V) and capacitance vs. voltage (C–V) characteristics provide fundamental information about the polarization switching behavior and the conduction mechanism. Several models have been established to interpret the I–V and C–V characteristics.[11–13] However, the effect of electric field magnitude on the MFM structure has not received much attention, and the contribution of the effect of domain capacitance has not, to our knowledge, been included in a capacitive equivalent circuit model for ferroelectric thin films. In this work, a $Pb(Zr_{0.52}Ti_{0.48})O_3$ thin film was prepared using the sol-gel method and the I–V and C–V characteristics were measured. A capacitance model that includes the effect of MFM interfaces and domain capacitance was used to model the observed behavior.

Experimental

The chemical reagents used in this work were lead(II) acetate trihydrate [$Pb(CH_3COO)_2 \cdot 3\,H_2O$], 2-methoxyethanol [$CH_3OCH_2CH_2OH$], zirconium(IV) propoxide [$Zr(CH_2CH_2CH_3)_4$], and titanium(IV) ethoxide [$Ti(CH_3CH_2O)_4$]. All chemicals were analytical grade purity of 99.99% and were used as received without further purification.

$Pb(Zr_{0.52}Ti_{0.48})O_3$ thin films were deposited on Pt(111)/Ti/SiO_2/Si(100) substrate using a sol-gel process. The precursor solution for the coating was prepared by a modified 2-methoxyethanol (2MOE) synthesis method:[14,15] dissolving appropriate amounts of $Pb(CH_3COO)_2 \cdot 3\,H_2O$ into 2MOE

solution by magnetic stirring for 2 h, followed by stoichiometric addition of $Zr(CH_2CH_2CH_3)_4$ and $Ti(CH_3CH_2O)_4$ into the solution with further magnetic stirring over 12 h. 10 mol% excess $Pb(CH_3COO)_2 \cdot 3\,H_2O$ was added to compensate the Pb loss during annealing. The PZT precursor solution was spin coated with a SCS G3 spin coater (Specialty Coating Systems, Inc.) on the $Pt/Ti/SiO_2/Si$ substrates at 4000 RPM for 60 s, followed by pyrolysis at 300°C for 1 min on a hot plate in air. After every four layers, a rapid thermal process was performed at 700°C for 1 min in air. Solution coating and firing were repeated to produce PZT thin films with 12 layers. In addition, dried gel was prepared from the coating solution, and PZT powders were obtained by sintering the dried gel at 600°C for 2 h in air. Au top electrodes were deposited by means of sputtering using a shadow mask with the size of 1 mm × 1 mm for each point to create parallel plate capacitors in PZT thin films. A typical thickness of the top electrodes was 200 nm. The crystal structures of the PZT film and powder were examined using X-ray diffraction (XRD, Bruker D8) with Cu K_α radiation ($\lambda = 1.541\,76$ Å) at the scanning rate of 5°/min from 20° to 55°. A Field-Emission Scanning Electron Microscope (FESEM, JSM-6700F) was used to observe the surface and cross-section of the PZT film. P–E and I–V measurements were performed on the PZT capacitors using a ferroelectric test system (Radiant Technology Precision LC Materials Analyzer). A low-frequency impedance analyzer (HP-4284A) was employed to measure the C–V characteristics of the PZT capacitor.

Results and discussion

Figures 5.1(a) and 5.1(b) show the XRD patterns of the PZT thin film and powder. The {110} reflection is the strongest peak in figure 5.1(b) for the powder sample of random orientation. But the {100} reflections are much higher than the {110} peak in figure 5.1(a); the reflection {100} is the strongest peak. This indicates that the PZT film corresponding to figure 5.1(a) is of ⟨100⟩-preferred orientation. For a Zr/Ti ratio of 52/48, the growth planes with the lowest activation energy are {100} planes.[16] This results in the formation of PZT thin film with ⟨100⟩-preferred orientation. In order to determine the degree of preferred orientation, the volume fraction $\alpha_{(h00)}$ of [h00]-oriented

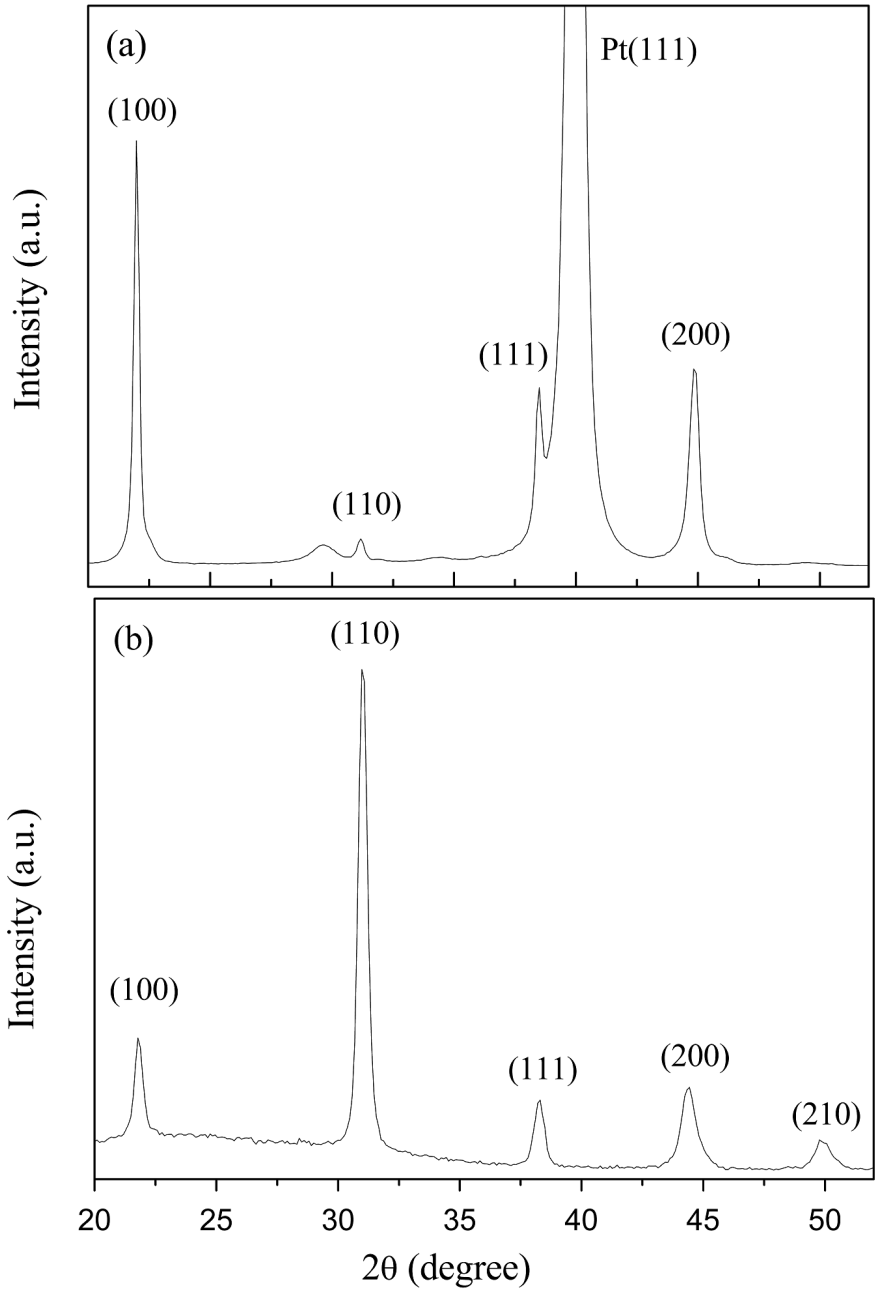

Figure 5.1: XRD patterns of (a) PZT thin film and (b) PZT powder.

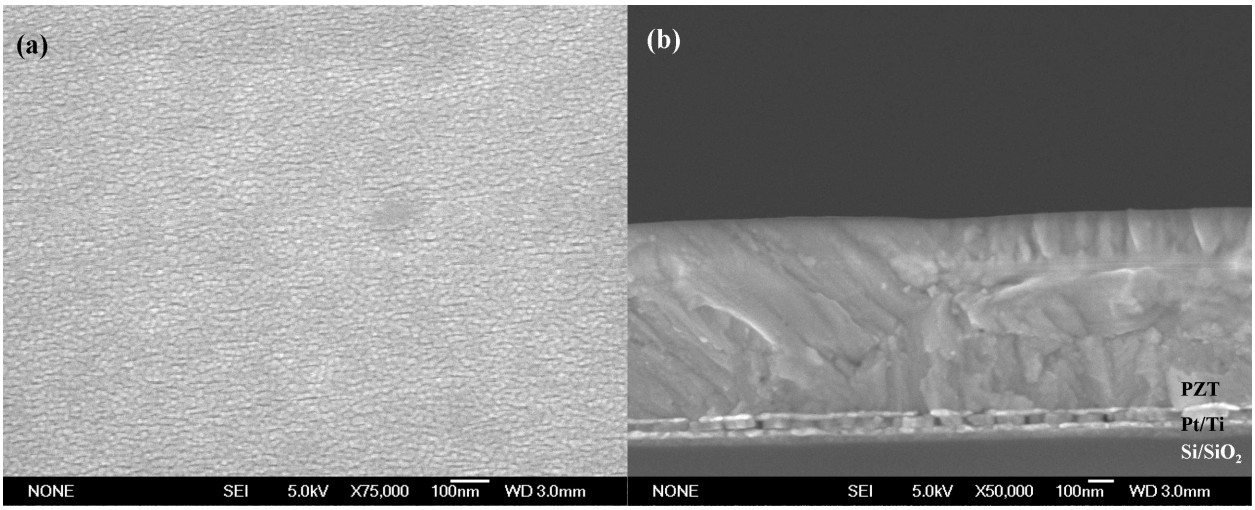

Figure 5.2: (a) Surface and (b) cross-section of SEM images of PZT thin film.

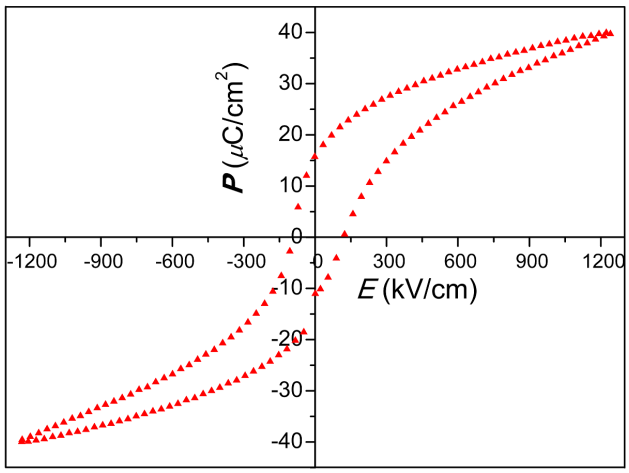

Figure 5.3: Ferroelectric hysteresis loops of PZT thin film.

grains in PZT film was approximated as[17]

$$\alpha_{(h00)} = \frac{\sum \frac{I_{n00}}{I^*_{n00}}}{\sum \frac{I_{hkl}}{I^*_{hkl}}}, \tag{5.1}$$

where I_{hkl} is the measured intensity of the (hkl) peak for the film, I^*_{hkl} is the intensity for powder, and n is the number of reflections. The α value for the PZT thin film is $\alpha_{(h00)} \approx 80\%$.

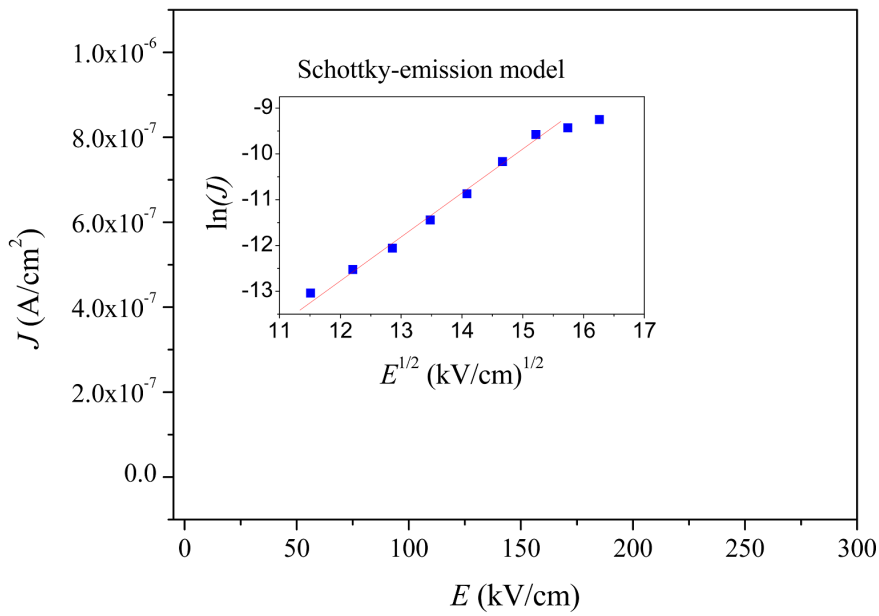

Figure 5.4: J–E characteristic of PZT thin film. Inset shows the data plotted based on Schottky-emission model that produces a linear $\ln J$–$E^{\frac{1}{2}}$ curve.

Figure 5.2 shows SEM micrographs of surface and cross-section of the PZT film. A dense, homogeneous, and crack-free PZT thin film is observed in figure 5.2(a), and the average width of grains in the columnar structure is approximately 30 nm. The thickness of the PZT film is about 750 nm based on the cross-sectional SEM image in figure 5.2(b). This value was used to determine the coercive field from the ferroelectric measurement. The polarization–field loop of the PZT thin film measured at room temperature with the frequency of 1 kHz is shown in figure 5.3. The $2P_r$ and $2E_c$ of the PZT thin film are 28 μC cm^{-2} and 240 kV cm^{-1}, respectively, which are similar to the results reported by Bassiri-Gharb et al.[18] and Nguyen et al.[19]

Figure 5.4 illustrates the leakage current density as a function of electric field of the ferroelectric PZT thin film (J–E curve, based on the I–V behavior measured at a DC bias from 0 V to 20 V). The initial linear part of the J–E curve appears ohmic up to about 100 kV cm^{-1}. A linear $\ln J$–$E^{\frac{1}{2}}$ plot is obtained (see the inset of figure 5.4), which is characteristic of the Schottky-emission model

with deep traps. In the Schottky-emission model, the current is given by[20]

$$J = A^{**}T^2 \exp\left[\frac{-q\left(\phi_{\mathrm{B}} - \sqrt{\frac{qE}{4\pi\varepsilon_0\varepsilon_{\mathrm{r}}}}\right)}{K_{\mathrm{B}}T}\right], \tag{5.2}$$

where A^{**}, T, q, ϕ_{B}, K_{B}, ε_0, ε_{r}, and E are the effective Richardson constant, absolute temperature, the electron charge, Schottky potential barrier, the Boltzmann constant, the permittivity of free space, dielectric constant (relative permittivity), and the electrical field, respectively.

Pb has a high partial pressure and can readily evaporate from lattice sites during thermal processes, leaving vacancies behind. Lead vacancies act as acceptor impurities and are considered to be one of the main sources for the leakage current in PZT thin films.[21] The defect reaction can be written as

$$\mathrm{Pb_{Pb}} \longleftrightarrow \mathrm{Pb} + \mathrm{V_{Pb}^{2-}} + 2\,\mathrm{h^+}, \tag{5.3}$$

where $\mathrm{Pb_{Pb}}$ and $\mathrm{V_{Pb}^{2-}}$ are the lead atom in the lattice and the lead vacancy, respectively. When the injected free carrier density exceeds the volume-generated free carrier density (over 100 kV cm^{-1}), the main conduction mechanism is Schottky conduction associated with the free carriers trapped by the lead vacancies. The leakage current density was observed to increase rapidly above 100 kV cm^{-1}. At this electric field magnitude, sufficient injected carriers fill almost all traps generated by lead vacancies and further injected carriers exist as free carriers contributing to the leakage current.

Figure 5.5(a) shows the C–V curve of the PZT thin film at 10 kHz. When voltage is applied from −10 V to 10 V, and then from 10 V to −10 V, a butterfly-like ferroelectric capacitance variation is observed. Two polarization peaks occur that correspond to the ferroelectric measurements. $+V_{\mathrm{s}}$ and $-V_{\mathrm{s}}$ are the positive and negative switching biases corresponding to the coercive field and associated with polarization switching. These voltages describe the transition of reverse junction capacitance between top and bottom electrode with the Schottky model. The capacitance of this MFM system at $+V_{\mathrm{s}}$ and $-V_{\mathrm{s}}$ is slightly asymmetric. This may be the result of Pb vacancies

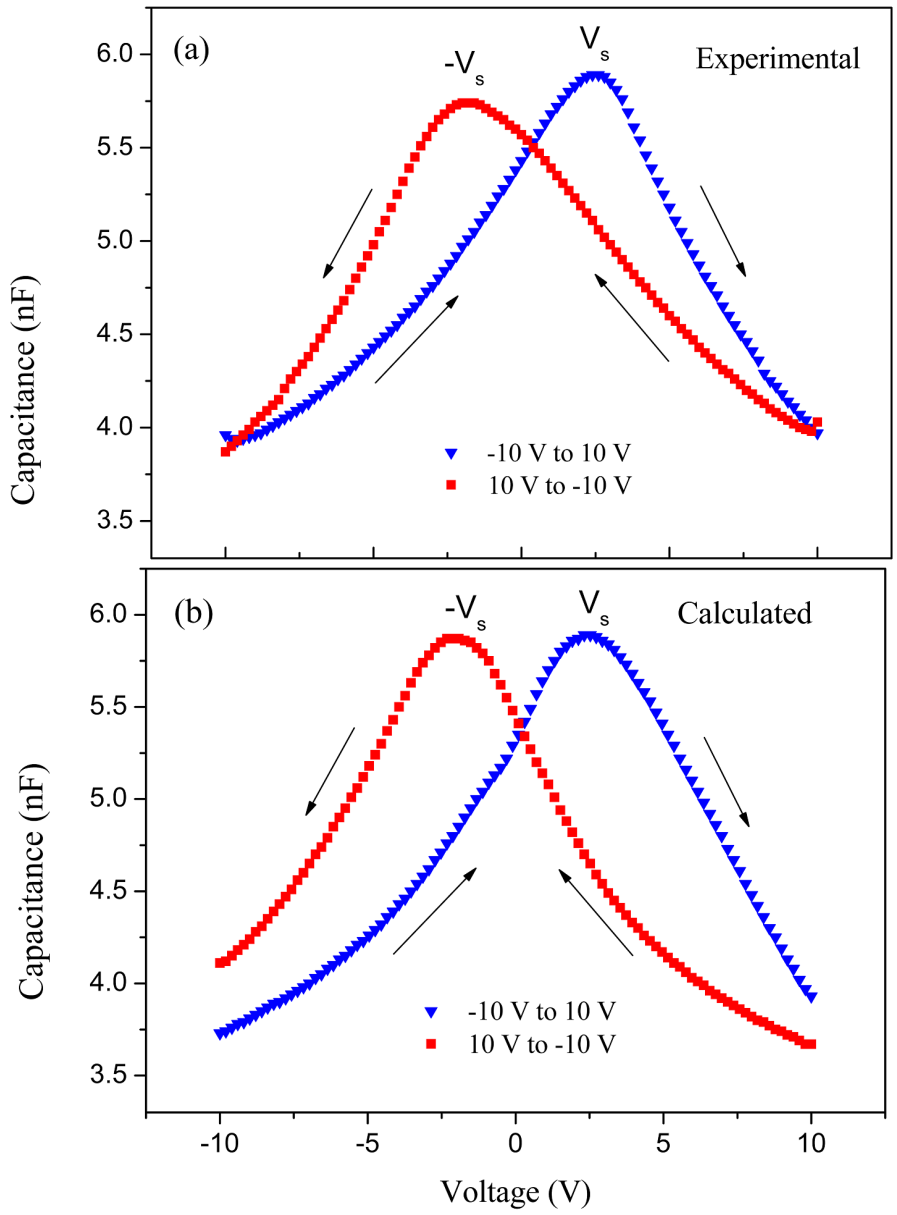

Figure 5.5: C–V curve of experimental (a) and calculated (b) PZT thin film from -10 V to 10 V.

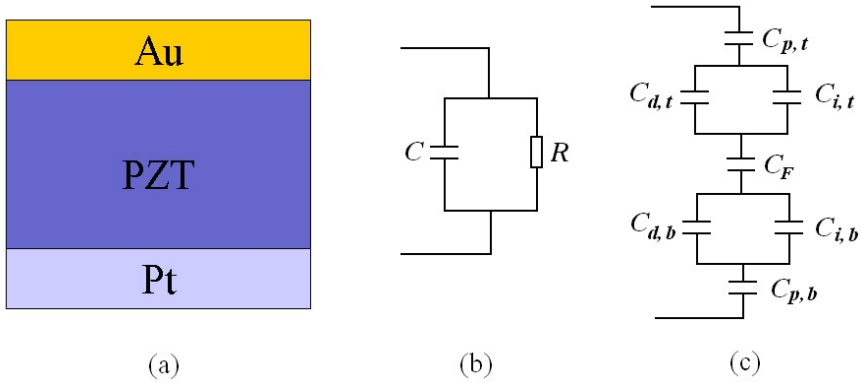

Figure 5.6: Electrical characterization model of PZT thin film. (a) Schematic drawing of MFM structure, (b) regular equivalent circuit of MFM system, (c) static capacitance model including the depletion charge (C_d), polarization charge (C_p), interface-trap charge (C_{it}), and electrical domain (C_F) capacitances. The indices t and b refer to top and bottom electrodes.

(acceptor impurities). When voltage is applied from −10 V to 10 V, injected carriers will fill the traps generated by lead vacancies, decreasing the acceptor doping density. Consequently, when voltage is applied from 10 V to −10 V, the accumulation of effective charge will decrease accordingly, leading to a slight drop of the capacitance at $-V_s$.

A modified C–V model was developed for the poled ferroelectric with voltage applied in the polarization direction based on the MFM system with Schottky contacts. Figure 5.6(a) shows a schematic drawing of the MFM system, figure 5.6(b) the equivalent circuit typically used, and figure 5.6(c) a proposed capacitance model for the PZT capacitor. For the model of the MFM structure of PZT film, the equivalent-circuit includes a capacitance in parallel with a resistance. When the leakage current is very low, the resistance approaches infinity. Consequently, the resistance produces a negligible effect on the C–V model at low voltage.

The standard equivalent circuit (figure 5.6(b)) does not model the individual effects of the metal contacting the PZT. The PZT has semiconducting characteristics. In this case, a built-in electric field (E_{bi}) will form at the metal-semiconductor contacts creating a depletion layer. In the top and bottom of the system, the directions of E_{bi} are opposite (from metal to PZT film in both cases). Based on this model, a static capacitor model was established as shown in figure 5.6(c). The

model includes the depletion charge (C_d), polarization charge (C_p), interface-trap charge (C_{it}), and electrical domain (C_F) capacitances. The electric domain contribution to dielectric permittivity has been described previously, but to our knowledge, it has not been included in a capacitance model of thin films.

The electric domain capacitance (C_F) is associated with domain walls within the PZT thin film. When a bias is applied, dipoles in the PZT thin film will reorient. Large-scale reorientation through domain wall motion requires less energy than homogeneous reorientation of the dipoles. Although the material is driven toward a single domain state by a high electric field, the single domain state is difficult or impossible to achieve in a ferroelectric polycrystalline system.[22,23] There is a characteristic width associated with domain walls that arises from the increased energy associated with polarization gradients balancing the crystal structure energy, and when the film thickness is smaller than this, width domains formation is constrained. There is also a surface effect on polarization associated a depletion zone. Charge accumulating within domain walls and a change of the dielectric permittivity associated with the highly distorted unit cells of the domain walls contribute to the total capacitance in thicker films. In ref. 11, Tayebi et al. established a C–V model for ultra thin PZT film (17 nm) without an electrical domain capacitance (C_F). The domain capacitance was not needed, because domains in ultra thin PZT film are unstable and can be easily affected by an antiparallel built-in electric field[11] because the depletion layer width is comparable with the remaining thickness of the ultra thin film. This makes the effective electrical domain capacitance difficult to form, and thus, the electrical domain capacitance can be neglected in the ultra thin film. On the contrary, in the C–V model for our 750 nm film, the built-in electric field has less influence on the domains because the depletion layer width is much smaller than that of the remaining part of the film. As a consequence, the electrical domain capacitance (C_F) needs to be taken into consideration in our PZT thin film. This suggests that there is a critical thickness above which C_F must be included.

In the Schottky metal–semiconductor contacts, the depletion layer width (W) and depletion layer capacitance (C_d) from an AC signal are defined as[12,24]

$$W = \sqrt{\frac{2\varepsilon_0\varepsilon_\mathrm{r}}{qN_\mathrm{a}}(V_\mathrm{bi} + V_\mathrm{A})} \tag{5.4}$$

and

$$C_\mathrm{d} = \frac{\varepsilon_0\varepsilon_\mathrm{r}A}{W} = \frac{\varepsilon_0\varepsilon_\mathrm{r}A}{\sqrt{\frac{2\varepsilon_0\varepsilon_\mathrm{r}}{qN_\mathrm{a}}(V_\mathrm{bi} + V_\mathrm{A})}}, \tag{5.5}$$

where ε_0, ε_r, A, N_a, V_bi, V_A, and q are the permittivity of free space, the dielectric constant of the PZT film, the electrode area, the equivalent acceptor doping density, the built-in potential of the Schottky barrier, the applied bias, and the charge, respectively. The built-in potential can be expressed as follows:[11,24]

$$V_\mathrm{bi} = \frac{\chi_\mathrm{PZT}}{q} + \left(\frac{E_\mathrm{C(PZT)} - E_\mathrm{F(PZT)}}{q}\right) - \frac{\phi_\mathrm{M}}{q}, \tag{5.6}$$

where χ_PZT, $E_\mathrm{C(PZT)}$, and $E_\mathrm{F(PZT)}$ are the affinity, conduction band, and Fermi energies of the PZT film, and ϕ_M is work function of the metal top/bottom electrode.

The interface polarization capacitance (C_p) resulting from polarization charges within an ultrathin layer from the metal electrode, referred to as the dead layer δ, is given by[11]

$$C_\mathrm{P} = \frac{\varepsilon_0\varepsilon_\mathrm{r}A}{\delta}. \tag{5.7}$$

Interfacial trap capacitance (C_it) originating from interface defects coexists in parallel with C_p. According to Gauss theory, electric domain capacitance (C_F), originating from the charge accumulation and modified polarization reorientation within domain walls, can be described by[25]

$$C_\mathrm{F} = \frac{\mathrm{d}Q}{\mathrm{d}V} = A\left(\frac{\varepsilon_0\varepsilon_\mathrm{r}}{t_\mathrm{F}} + \frac{\mathrm{d}P}{\mathrm{d}V}\right), \tag{5.8}$$

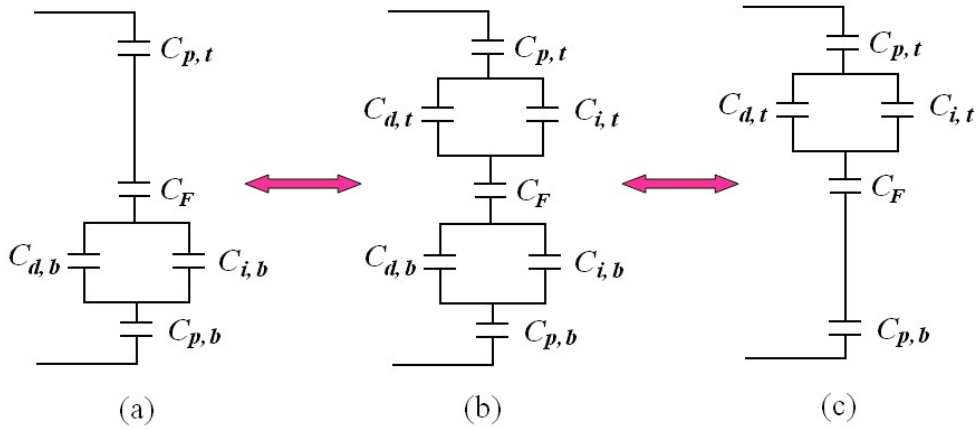

Figure 5.7: Dynamic capacitance model of PZT thin film at various bias. (a) −10 V, (b) ∼0 V, and (c) 10 V.

where t_F is effective width of electric domain capacitance, which is equal to the total thickness of PZT thin film minus the depletion layer width.

As the bias is varied, the total capacitance will be composed of reverse and forward biased junction capacitances corresponding to up and down polarizations, respectively. When the bottom electrode is grounded and −10 V is applied to the top electrode, the external electric field (E_a) is from bottom to top, which will decrease the thickness of the top depletion layer and expand that of the bottom depletion layer. When applying 10 V voltage to the top electrode, the situation will change to the opposite. So, when applying voltage from −10 V to 10 V in the C–V curve, the capacitor model of the system is dominated by the model shown in figure 5.7. With the increasing of applied voltage, the capacitor model will evolve as shown in figures 5.7(a)–5.7(c) dynamically.

Parameters were determined for the C–V model of the PZT thin film and a simulation was performed. C_d and C_p were calculated using equations 5.4–5.7. C_{it} originating from interface traps can coexist in parallel with C_d if reactive (oxidizing) metals such as Ti are used as electrodes,[11] so here, C_{it} was neglected relative to C_d. The P–V curves (down and up) of PZT thin film from both −10 V to 10 V and 10 V to −10 V were fit to determine the differential $\frac{dP}{dV}$ and obtain C_F using equation 5.8. The frequency of the C–V model parameters are in accordance with that of P–V measurement of 1 kHz, and no attempt was made to extend the model to other frequencies.

The resulting parameters are $\varepsilon_r = 428$, $A = 1 \times 10^{-6}\,\mathrm{m}^2$ (the area of Au electrode), $\delta = 12.1\,\mathrm{nm}$, $N_a = 0.34 \times 10^{20}\,\mathrm{cm}^{-3}$, $\chi_{PZT} = 3.5\,\mathrm{eV}$, $\phi_{M(Pt)} = 5.3\,\mathrm{eV}$ (bottom electrode), and $\phi_{M(Au)} = 5.1\,\mathrm{eV}$ (top electrode), $E_{C(PZT)} - E_{F(PZT)} = 2.0\,\mathrm{eV}$.[11,12,26] The results are shown in figure 5.5(b), which is similar to the experimental curve (figure 5.5(a)), indicating that the capacitor network model represents the dominant contributions to the C–V behavior of ferroelectrics with bistable polarization states.

Conclusion

In summary, dense, homogeneous, and crack-free ferroelectric PZT thin film with $\langle h00 \rangle$-preferred orientation were obtained by using the sol-gel method. The volume fraction $\alpha_{(100)}$ of $\langle h00 \rangle$-oriented grains in PZT film was approximated [$\alpha_{(100)} \approx 80\%$] from XRD results of PZT thin film and powder. The PZT thin film exhibited good ferroelectric P–E loops. With a cyclic voltage of 95 V, the $2P_r$ and $2E_c$ of PZT thin film were $28\,\mu\mathrm{C\,cm}^{-2}$ and $240\,\mathrm{kV\,cm}^{-1}$, respectively. The PZT thin film showed a low leakage current density from $10 \times 10^{-8}\,\mathrm{A\,cm}^{-2}$ to $10 \times 10^{-7}\,\mathrm{A\,cm}^{-2}$. The conductive behavior was dominated by Schottky emission with deep traps from $100\,\mathrm{kV\,cm}^{-1}$ to $250\,\mathrm{kV\,cm}^{-1}$. A dynamic capacitance model, in which an electrical domain capacitance (C_F) was taken into consideration, was established based on a MFM system with Schottky contacts. The introduction of domain capacitance (C_F) into the model is required for thicker films and not for ultrathin films. This suggests there is a critical thickness in ferroelectric film above which C_F must be included. Parameters were experimentally determined for the capacitance model and it was shown to reproduce the observed C–V behavior.

Acknowledgments

This work was supported by NSF Nanosystems Engineering Research Center for Translational Applications of Nanoscale Multiferroic Systems (TANMS) Cooperative Agreement Award No. EEC-1160504.

References

(1) Scott, J. F. *Science* **Feb. 2007**, *315*, 954–959.

(2) Maksymovych, P.; Jesse, S.; Yu, P.; Ramesh, R.; Baddorf, A. P.; Kalinin, S. V. *Science* **June 2009**, *324*, 1421–1425.

(3) Tsymbal, E. Y.; Gruverman, A. *Nature Materials* **May 2013**, *12*, 602–604.

(4) Dawber, M.; Rabe, K. M.; Scott, J. F. *Reviews of Modern Physics* **Oct. 2005**, *77*, 1083–1130.

(5) Nguyen, M. D.; Dekkers, M.; Vu, H. N.; Rijnders, G. *Sensors and Actuators A: Physical* **Sept. 2013**, *199*, 98–105.

(6) Bastani, Y.; Bassiri-Gharb, N. *Acta Materialia* **Feb. 2012**, *60*, 1346–1352.

(7) Feigl, L.; Pippel, E.; Pintilie, L.; Alexe, M.; Hesse, D. *Journal of Applied Physics* **2009**, *105*, 126103.

(8) Xu, L. H.; Jiang, D. D.; Zheng, X. J. *Journal of Applied Physics* **2012**, *112*, 043521.

(9) Bose, A.; Sreemany, M.; Bysakh, S. *Applied Surface Science* **Oct. 2013**, *282*, 202–210.

(10) Cheng, J.-R.; Zhu, W.; Li, N.; Cross, L. E. *Applied Physics Letters* **2002**, *81*, 4805.

(11) Tayebi, N.; Kim, S.; Chen, R. J.; Tran, Q.; Franklin, N.; Nishi, Y.; Ma, Q.; Rao, V. *Nano Letters* **2012**, *12*, 5455–5463.

(12) Pintilie, L.; Boerasu, I.; Gomes, M. J. M.; Zhao, T.; Ramesh, R.; Alexe, M. *Journal of Applied Physics* **2005**, *98*, 124104.

(13) Sun, S.; Kalkur, T. S. *IEEE Transactions on Ultrasonics, Ferroelectrics, and Frequency Control* **July 2004**, *51*, 786–793.

(14) Lakeman, C. D. E.; Payne, D. A. *Journal of the American Ceramic Society* **Nov. 1992**, *75*, 3091–3096.

(15) Wolf, R. A.; Trolier-McKinstry, S. *Journal of Applied Physics* **2004**, *95*, 1397.

(16) Brooks, K. G.; Reaney, I. M.; Klissurska, R.; Huang, Y.; Bursill, L.; Setter, N. *Journal of Materials Research* **Oct. 1994**, *9*, 2540–2553.

(17) Lu, C. J.; Qiao, Y.; Qi, Y. J.; Chen, X. Q.; Zhu, J. S. *Applied Physics Letters* **2005**, *87*, 222901.

(18) Bastani, Y.; Schmitz-Kempen, T.; Roelofs, A.; Bassiri-Gharb, N. *Journal of Applied Physics* **2011**, *109*, 014115.

(19) Nguyen, M. D.; Nazeer, H.; Dekkers, M.; Blank, D. H. A.; Rijnders, G. *Smart Materials and Structures* **Aug. 2013**, *22*, 085013.

(20) Sze, S. M.; Ng, K. K., *Physics of Semiconductor Devices*, 3rd Ed.; John Wiley & Sons: Hoboken, NJ, 2006.

(21) Zhang, Z.; Wu, P.; Lu, L.; Shu, C. *Applied Physics Letters* **2006**, *88*, 142902.

(22) Li, F. X.; Rajapakse, R. K. N. D. *Journal of Applied Physics* **2007**, *101*, 054110.

(23) Jones, J. L.; Hoffman, M.; Bowman, K. J. *Journal of Applied Physics* **2005**, *98*, 024115.

(24) Muller, R. S.; Kamins, T. I., *Device Electronics for Integrated Circuits*, 3rd Ed.; John Wiley & Sons: Hoboken, NJ, 2007.

(25) Zheng, C.; Ting-Ao, T. *Ferroelectrics* **June 1997**, *197*, 111–114.

(26) Apostol, N. G.; Stoflea, L. E.; Lungu, G. A.; Tanase, L. C.; Chirila, C.; Frunza, L.; Pintilie, L.; Teodorescu, C. M. *Thin Solid Films* **Oct. 2013**, *545*, 13–21.

Chapter 6

Fine tuning the magnetic properties of cobalt ferrite thin films by controlling nanoscale structure

Shauna Robbennolt, Hyeyeon Kang, Abraham N. Buditama, Paul Nordeen, Gregory P. Carman, and Sarah H. Tolbert

Abstract

Here we report the use of nanostructuring techniques to create thin films of cobalt ferrite (CFO) with room temperature coercivities ranging from 3108 Oe down to 70 Oe. This is achieved by employing two methods: block copolymer templating to create mesoporous thin films and assembling pre-synthesized nanocrystals into thin films. We find that porosity, starting material, and annealing temperature can all be successfully used and combined to create CFO thin films with a wide range of coercivities. Finally, we find that in the samples with low coercivities, X-band ferromagnetic resonance can be observed. In these cases, the observed linewidth is 39 G, which suggests that nanostructured CFO is promising for high frequency applications.

Introduction

There is great research interested in magnetic spinel ferrites (MFe$_2$O$_4$; M = Mn, Fe, Co, Ni, etc.) due to their widespread use in areas such as ferrofluids,[1–7] magnetic recording media,[8–12]

biomedical applications,[13–18] and RF devices.[19–28] In particular, cobalt ferrite ($CoFe_2O_4$, CFO) is a hard magnetic material with a bulk coercivity of more than 4000 Oe and reasonably high saturation magnetization of 500 emu g^{-1}, which has led to its use in magnetic recording media.[29,30] However, its high coercivity also limits its use in other applications, especially high frequency applications, where soft ferrites are extensively used.[23–27,31–33]

Advances in nanoscience now allow us to control a wide range of material properties through nanostructuring.[34–41] This allows us to effectively, and often selectively, tune material properties to tailor them to specific applications. Here, we apply nanostructuring techniques to the CFO material system to create a magnetically soft system, opening further use in high frequency applications. This is accomplished by controlling magnetic domain size and structure, which determines the coercivity and remanence without significantly influencing the dynamic properties, such as the ferromagnetic resonance (FMR). Here we specifically investigate two methods for controlling the domain size and dipolar coupling: introducing mesoporosity and using nanocrystals as building blocks.

Introducing mesopores has been widely explored as a method to increase surface area,[41–44] limit crystallite size,[45–47] and tune the electric,[47,48] magnetic,[20,34,46] and mechanical properties[34,42,46,49] in thin films. An open porous network can increase the surface area in a thin film by orders of magnitude,[41,42] which is useful in areas where surface reactivity is important, such as catalysis,[43,45,48,50,51] as well as areas where large interfacial areas are desired, such as pseudocapacitive energy storage.[44,49,52] Porosity can also control crystalline and magnetic domain size by breaking up the material and limiting domain size to be equal to or smaller than the wall thickness.[20,34] We have previously shown that in sol-gel derived thin films of CFO with 14 nm pores, the coercivity of the films could be tuned by changing the wall thickness, and therefore the maximum magnetic domain size. In these films, the porous structure also promoted a preference for out-of-plane magnetic orientation, which is unusual in thin films, and is thought to be due to a difference in the mechanical strain state of the system.[34] In that system as well as the work presented here, the mesoporous structure is achieved by a block copolymer templating method.

Block copolymer templating is a facile route to creating mesoporous structures in thin films.[34,45–47,53,54] In this method, an amphiphilic diblock copolymer is mixed in solution with an inorganic precursor material, such as a sol-gel solution or nanocrystals. The amphiphilic nature of the polymer induces the formation of polymer micelles such that in a polar solvent the hydrophobic block aggregates in the micelle core while the hydrophilic block interacts with the solvent keeping the micelle soluble. This mixture is then deposited onto a substrate where the polymer and inorganic material undergo evaporation induced self-assembly (EISA). This composite is then calcined to crosslink or sinter the inorganic material and thermally degrade and remove the polymer, leaving behind a robust, mesoporous film. In the case of sol-gel-derived films, the films can then be crystallized at higher temperatures. The film morphology is determined by the initial organic-inorganic composite structure and can be tuned by changing the size or composition of the polymer as well as the ratio between polymer and inorganic precursor material in solution.[34,46]

Another route to controlling domain structure in thin films is to make thin films using nanocrystals as precursor materials. Nanocrystals are attractive because they are solution-processable, highly tunable, and can be synthesized at relatively low temperatures, usually below 300 °C.[35,36,55–61] Below a critical size, each nanocrystal is a single crystalline domain as it is energetically unfavorable to form a grain boundary in such a small structure. Similarly, in magnetic materials, there is a critical size below which domain wall formation is unfavorable, so each nanocrystal is also a single magnetic domain.[55] In the case of CFO, it has been shown that nanocrystals have both a single crystallographic and magnetic domain when they are below 40 nm in diameter.[57] Therefore, the size of the magnetic domain can be controlled by changing the nanocrystal size, which is easily achieved synthetically.[35,61–63] These nanocrystals with well-defined domain structure can then be deposited into thin films with magnetic properties determined by the original nanocrystal properties.

Additionally, recent work has shown that nanocrystals can be made compatible with block copolymer templating techniques leading to mesoporous, nanocrystal-based films.[53] Traditionally,

nanocrystals were not well suited to this type of templating. This is due to the fact that they are generally synthesized with long organic ligands on the surface which serve to both keep the nanocrystals soluble and prevent aggregation.[35,36,61,62] However, while useful, these ligands also prevent the nanocrystals from sintering to form a robust network during the annealing process causing the film to collapse upon removal of the polymer template. Recently, new ligand-stripping chemistries have been developed that create bare nanocrystals with charges on the surface that stabilize them in solution.[37,38] These charge-stabilized nanocrystals can then be successfully templated using block copolyer–based methods. Templated nanocrystal films combine the advantages of nanocrystals, such as domain size control and low temperature crystallization, with the benefits of structured, porous thin films.

In this work, we present wide range tunability over the magnetic properties of cobalt ferrite thin films by tuning their nanoscale architecture. We investigate films made from sol-gel methods, as well as different sizes of nanocrystals, both mesoporous and dense, and processed over a range of annealing temperatures. We find that the room temperature coercivity is tunable from 3108 Oe for dense, sol-gel-derived films down to 70 Oe for mesoporous, nanocrystal-based films. Finally, we investigate the dynamic properties of these films by looking at the ferromagnetic resonance (FMR) in X-band and find that the FMR remains constant across all films despite drastic differences in static magnetic properties.

Experimental

Materials

Cobalt(II) acetylacetonate (> 99%) and 1-octadecanol (97%) were obtained from Alfa Aesar. Iron(III) acetylacetonate (> 99%) and benzyl ether (99%) were purchased from Alfa Aesar. Cobalt(II) nitrate hexahydrate (99.99%), iron(III) nitrate nonahydrate (99.999%) 1,2-hexadecanediol (technical grade, 50%) and 2-methoxyethanol (99.8%) were purchased from Sigma-Aldrich. Poly(styrene-*b*-N,N-

dimethylacrylamide) with M_n: PS(51000)-*b*-PDMA(8500), was obtained from Polymer Source. All chemicals were used without further purification.

Fabrication of sol-gel-derived CFO thin films

Sol-gel-derived films were fabricated a described in our previous work. $Co(NO_3)_2 \cdot 6\,H_2O$ (0.11 g) and $Fe(NO_3)_3 \cdot 9\,H_2O$ (0.11 g) were dissolved in 1 ml of 2-methoxyethanol, 1 ml of ethanol and 0.02 ml of glacial acetic acid. This solution was allowed to age for 3 d with magnetic stirring at room temperature and was always found to be clear at this point. The templating polymer used to make porous structures was poly(ethylene-*co*-propylene)-*block*-poly-(ethylene oxide), with a mass ratio of PEP(3900)-*b*-PEO(4000), a block ratio of PEP_{56}-*b*-PEO_{91}, and a PDI = 1.05. To make mesoporous films, 40 mg of PEP-PEO was dissolved in 1 ml of ethanol before being added to a 2 ml solution and stirred for 1 h. Both dense and porous films were deposited via dip coating at less than 20% humidity onto cleaned Si substrates. These films were then calcined at 180 °C for 24 h to allow for solvent removal and to crosslink the CFO to form a more rigid inorganic-organic composite. Subsequently, the films were annealed at either 500 °C or 600 °C for 5 h to both remove the polymer template and crystallize the film. Film thickness can be fine-tuned using the rate at which the substrate is pulled out of the solution. For this work films with thicknesses of ~ 100 nm were studied.

Synthesis of CFO nanocrystals

The nanocrystals were synthesized following a procedure previously published by Song *et al.* with few modifications.[35] Dibenzyl ether was used as the solvent and oxygen source, rather than phenyl ether. For the synthesis of nanocrystals with a 5 nm diameter, $Co(acac)_2$ (2 mmol, 0.5143 g), 1,2-hexadecanediol (20 mmol, 5.169 g), oleic acid (10 ml), oleylamine (10 ml) and benzyl ether (40 ml) were all heated to 140 °C under flowing Ar and rapid magnetic stirring. $Fe(acac)_3$ (4 mmol, 1.413 g) well dissolved in benzyl ether (20 ml) was then injected and the mixture was then quickly heated

to 240 °C where it was allowed to react for 30 min before being cooled down to room temperature. The product was then precipitated with ethanol via centrifugation and redispersed in hexanes three times before being redispersed in either hexanes or toluene (20 mg ml^{-1}) for storage in air.

These 5 nm nanocrystals were then used as seeds to grow nanocrystals with a diameter of 8 nm. In this synthesis, 100 mg of 5 nm nanocrystals were mixed with $Co(acac)_2$ (1 mmol, 0.257 g), $Fe(acac)_3$ (2 mmol, 0.706 g), 1-octadecanol (10 mmol, 2.7049 g), and oleic acid (5 ml), oleylamine (5 ml) under Ar flow and magnetic stirring. The mixture was heated to 240 °C and allowed to react for 30 min before being cooled to room temperature and being washed in the same manner as for the 5 nm nanocrystals.

Ligand-stripping of CFO nanocrystals

The ligands were stripped using a previously published procedure by Rosen *et al.* in which tetraethyloxonium tetrafluroborate (Meerwein's salt) is used to reactively strip the native oleic acid ligands.[38] In a typical ligand-stripping procedure, 10 mg of Meerwein's salt was dissolved in 1 ml of dry acetonitrile in a nitrogen glovebox. The solution was then removed from the glovebox and 0.2 ml of that solution was added to 2 ml of CFO nanocrystals (20 mg ml^{-1}) in a centrifuge tube. The mixture was vortexed for approximately 30 s, 5 ml of chloroform was added, and then centrifuged at 4000 RPM for 5 min. Any nanocrystals left in solution were assumed to be incompletely exchanged and the supernatant was discarded although most of the nanocrystals had precipitated. The precipitate was then dissolved in either DMF or NMP, often a 1:1 ratio with a total volume of 1 ml. The ligand-stripped nanocrystals were then stable in solution for weeks and stored in air.

Fabrication of nanocrystal-based thin films

Nanocrystal-based films were deposited by dip coating and it was found that the relative humidity did not have a large impact on film quality, so it was not strictly controlled, although most films

were pulled at humidity levels between 20% and 40%. Here, we refer to films cast without a block copolymer templating agent as dense nanocrystal films and those with a templating agent as porous films. Dense films of as-synthesized nanocrystals (with ligand) were pulled from the initial 20 mg ml^{-1} solution in hexanes and the ligand-stripped nanocrystal films were pulled from solutions in 1:1 DMF:NMP. It was found that the nanocrystals were more stable in DMF, but DMF alone does not wet substrates well making it difficult to produce quality films.

Mesoporous nanocrystal films were made using poly(styrene-*b*-N,N-dimethylacrylamide), (PS-PDMA) as the templating agent. In a typical synthesis, 20 mg of PS-PDMA was added to 1 ml of DMF and mixed on a rotary mixer at room temperature until dissolved (~ 1 h). 1 ml of the ligand-stripped nanocrystal solution was then added to the polymer solution and the mixture was sonicated for 10 min. The solution was then left gently mixing on a rotary mixer until deposited. It is worth noting that all of the films here were deposited within 5 h of initially dissolving the polymer. Films deposited over a day after the polymer was dissolved were found to be of low quality. Both dense and porous films were then annealed for 4 h at annealing temperatures from 200 °C to 600 °C. For the porous films, temperatures at or above 400 °C were required to remove the polymer template.

Characterization

A JEOL JSM-6700F field emission scanning electron microscope (FE-SEM) was used to characterize the microstructure of the films. An FEI T12 Quick CryoEM and CryoET transmission electron microscope (TEM) operating at 300 kV was used to characterize the nanocrystal size and shape. Ellipsometric porosimetry was performed on a PS-1100 instrument from Semilab using toluene as the adsorbate at room temperature. A UV-visible CCD detector adapted to a grating spectrograph analyzes the signal reflected by the sample. The light source is a 75 W Hamamatsu Xe lamp and measurements were performed in the spectral range from 1.24 eV to 4.5 eV. Data analysis was performed using the associated SEA software.

The static magnetic characterization was done using a magnetooptical Kerr effect (MOKE) spectrometer. The homebuilt system uses a 620 nm laser, a photoelastic modulator modulating the beam at 60 Hz and a lock-in detector set to that frequency. All measurements were done in transverse mode measuring in-plane magnetization. X-ray diffraction patterns were the result of 2D grazing incidence wide angle X-ray scattering experiments (GIWAXS) performed at the Stanford Synchrotron Radiation Lightsource (SSRL). These experiments were carried out using beamline 11-3. The resulting 2D images were integrated to create the 1D patterns presented here. FMR spectra were collected using a Bruker EMX X-band EPR spectrometer operating at 9.72 GHz.

Results and discussion

The effect of mesoporosity on the properties of sol-gel-derived films was investigated first. Both dense films and polymer-templated, mesoporous films were fabricated, as described above. The pore structure was investigated using top-view SEM, as seen in figure 6.1a. The pores are seen to be circular, fairly well ordered and hexagonally packed. While top-view SEM is useful for characterizing pore structure, it cannot determine whether the polymer was indeed removed and to what degree. In order to confirm that the polymer template was removed to leave an open porous network, ellipsometric porosimetry was used. In this technique, a small molecule, in this case toluene, is adsorbed into the pores and then desorbed out of the pores while the change in film thickness is measured ellipsometrically. The pore size distribution, shown in figure 6.1b, was determined by fitting the adsorption and desorption isotherms using the Kelvin equation.[64] The adsorption process is a function of the pore volume while the desorption process is limited by the neck size, or the size of the tunnel connecting two pores. Therefore, the adsorption curve was used to determine that the average pore radius is 12 nm while the average neck radius is 10 nm in this sample. This correlates well to the SEM image in figure 6.1a in which the top view of the pores shows them to be on the order of 20 nm in diameter.

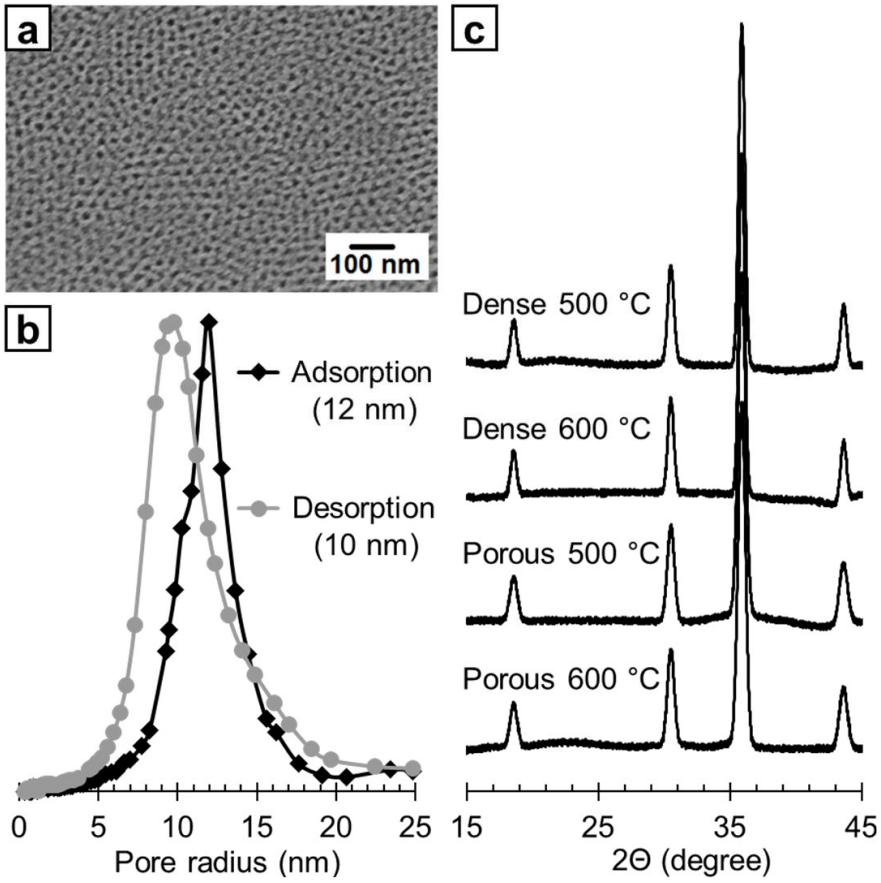

Figure 6.1: Characterization of both dense and porous sol-gel-derived cobalt ferrite (CFO) films. (a) Top-view SEM showing the pore structure of a templated, sol-gel-derived thin film annealed at 500 °C. (b) Pore radius distribution of a templated film annealed at 500 °C. The average pore size (black), calculated from the adsorption isotherm, is 12 nm while the average neck size (grey), from the desorption isotherm, is 10 nm. (c) X-ray diffractograms of dense and porous films annealed at 500 °C and 600 °C showing that all films are the desired spinel crystal structure with no observable impurities.

X-ray diffraction was used to confirm that the films had the desired spinel crystal structure. Representative diffractograms of both a dense and porous film, both crystallized at 500 °C, are shown in figure 6.1c. In both samples, the films were found to have a spinel crystal structure with no impurity phases present at measureable levels. Information about average crystallite size can also be extrapolated using the Scherrer equation:

$$\tau = \frac{K\lambda}{\beta \cos \theta}, \tag{6.1}$$

where τ is the average crystallite size, K is the shape factor, λ is the wavelength of the X-rays, β is the peak broadening, or full width at half maximum of the peak, and θ is the Bragg angle. In this work, we assume spherical domains and use a shape factor of 0.9. For the films crystallized at 500 °C, the approximate average crystalline domain size was found to be 26.2 nm for the dense film and 13.1 nm for the porous film. The estimated crystallite size in the porous film is approximately the same size as the pore walls, 10 nm, as determined by SEM. In the absence of a limiting pore structure, the crystalline domain size is determined by crystallization kinetics which is why the domains are larger in the bulk samples. This trend was found for films, regardless of crystallization temperature.

The static magnetic properties of these films was probed using two instruments: MOKE and SQUID magnetometers. These techniques measure magnetization in different ways, and on different time scales, so by comparing them, we can gain further insight into the magnetic properties of our films. In MOKE magnetometry, circularly polarized light interacts with the magnetic spins which rotates the polarization, referred to as Kerr rotation. The time constant of the measurement in this case is about 3 ms. SQUID magnetometry, on the other hand, is a measurement of the inductance caused by moving the sample through the center of the measurement coils. Its measurement time is longer than that of MOKE magnetometry, generally 1 s to 10 s. By comparing magnetic hysteresis loops for a given sample between these two methods, we can gain valuable insight into the time dependence of properties.

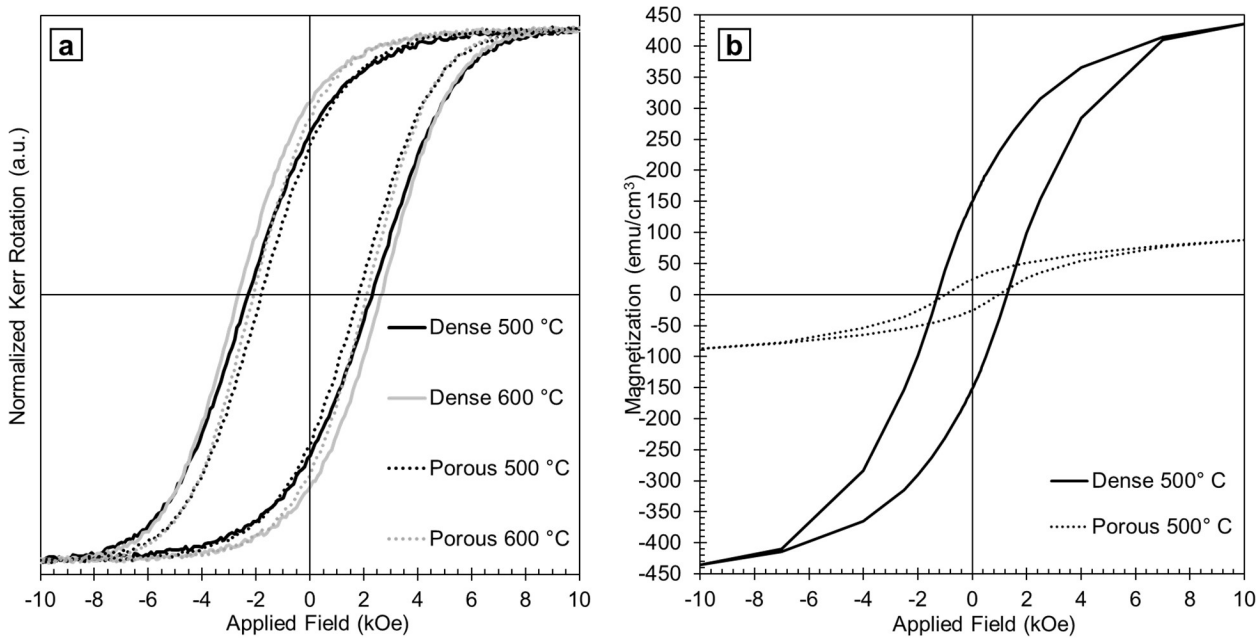

Figure 6.2: Magnetic characterization of sol-gel CFO films. (a) Magnetic hysteresis loops for dense (solid) and porous (dashed) films annealed at 500 °C and 600 °C collected on a MOKE magnetometer. The dense films have a higher coercivity than porous films and the films annealed at higher temperatures were more coercive than those annealed at lower temperatures. (b) Magnetic hysteresis loops for films annealed at 500 °C collected on a SQUID magnetometer which shows that the volume-normalized saturation magnetization is much higher for dense films. Note that the MOKE magnetometer cannot probe the saturation magnetization values which is why the SQUID magnetometer was employed here.

Figure 6.2a shows the room temperature magnetic hysteresis loops of both dense and porous sol-gel-derived CFO films crystallized at two different temperatures. The solid black and grey curves are dense films crystallized at 500 °C and 600 °C, respectively, and the corresponding dashed curves are from the respective porous films. The dense films have coercivities of 2590 Oe and 3110 Oe while the porous film show much lower coercivities of 1960 Oe and 2350 Oe for films crystallized at 500 °C and 600 °C, respectively.

The drastic lowering of the coercivity due to induced porosity is mainly attributed to the decrease in the magnetic domain size. As described above, the maximum magnetic domain size is limited by the wall thickness in porous films. The reduction in domain volume reduces the coercivity by reducing the magnetocrystalline anisotropy energy (MCA), as described in the Stoner–Wohlfarth model:[65]

$$E_{\mathrm{MCA}} = KV \sin^2 \theta, \tag{6.2}$$

where K is a material-specific magnetocrystalline anisotropy constant, V is the domain volume, and θ is the angle between an applied field and the easy axis. Coercivity is a measure of the MCA energy, so by reducing domain size (V), the MCA energy and therefore coercivity are also reduced. This is also the reason that the films crystallized at 600 °C have a higher coercivity. The higher crystallization temperature causes grain growth, leading to larger domains and therefore larger MCA and higher coercive widths. It is interesting to note that grain growth also occurs in the porous films. At elevated temperatures, the CFO structure can more freely rearrange leading to films with thicker pore walls and slightly larger pores, as discussed in our previous work.[34]

In order to more fully probe the magnetic properties, magnetic hysteresis loops measured using SQUID magnetometry were collected and are presented in figure 6.2b. Here again the coercivity is reduced from 1420 Oe in the dense film and 610 Oe in the porous film annealed at 500 °C. In both cases, the coercivities measured using SQUID magnetometry are lower than those measured using MOKE magnetometry. The longer measurement time of SQUID magnetometry allows more time for the spins to reorient due to thermal fluctuations leading to a lower observed

coercivity and remanent magnetization. Finally, whereas sample magnetization must be normalized in our MOKE measurements, SQUID magnetometry shows that there is a large difference in saturation magnetization between the samples. The dense film has a saturation magnetization of 440 emu cm^{-3}, which is approaching the bulk value of 485 emu cm^{-3}, while the porous film has a saturation magnetization of 90 emu cm^{-3}. This decrease can be attributed to the reduced density due to induced porosity.

In addition to making mesoporous films, another route to limiting domain size is to use nanocrystals as building blocks for thin films. Nanocrystals of two different sizes were synthesized and characterized using TEM. Figure 6.3 shows micrographs of the 5 nm as-synthesized (a) and 8 nm as-synthesized (b) nanocrystals. The nanocrystals are very monodisperse in size and shape and pack hexagonally which is indicative of monodispersity in spherical nanocrystals. The spacing between the nanocrystals is due to the organic ligands on the surface which cannot be seen in TEM.[61] These ligands can then be chemically removed in a manner that leaves charges on the surface, which can stabilize the nanocrystals in solution, but does not physically separate them. As expected, TEM images of the ligand-stripped nanocrystals, as shown in figure 2c–d, show that the nanocrystals are no longer spaced apart on the grid, but instead are touching. From these micrographs it can be seen that the ligand-stripping process increases the polydispersity in size somewhat, but the average size and shape are maintained. XRD shows that both sizes of nanocrystals were synthesized in the expected spinel crystal structure and that structure is preserved through the ligand-stripping process (figure 2e–f).

Thin films were made from both as-synthesized and ligand-stripped nanocrystals of each size. While the nanocrystals are crystalline as synthesized, the films were still annealed in order to sinter them together enough to make a mechanically robust film. Figure 6.4a shows representative hysteresis loops of films made from both sizes of nanocrystals, both as-synthesized and ligand-stripped, with data from a dense sol-gel film for comparison. The films annealed at 400 °C have coercivities of 140 Oe for the film of 5 nm nanocrystals and 210 Oe or the film of 8 nm nanocrystals.

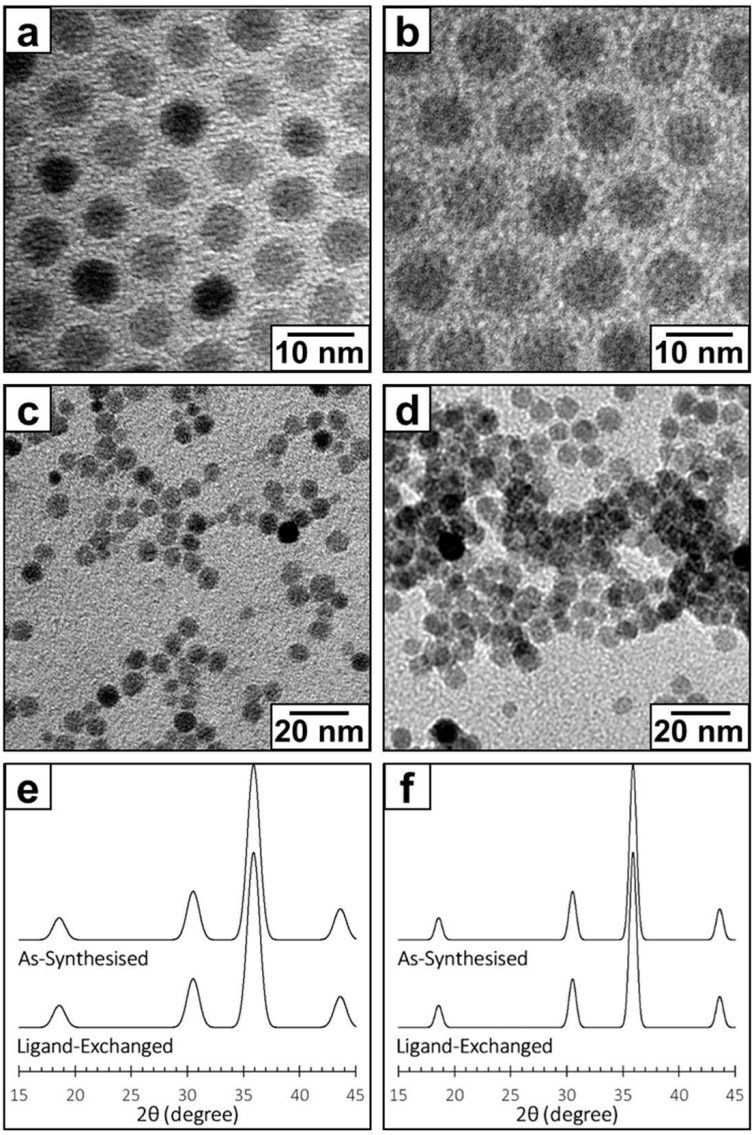

Figure 6.3: Characterization of CFO nanocrystals both as-synthesized and ligand-stripped. The ligand-stripping process is required in order to template nanocrystals into mesoporous thin films. TEM images of as-synthesized 5 nm (a) and 8 nm (b) nanocrystals and ligand-stripped 5 nm (c) and 8 nm (d) nanocrystals. The ligand-stripping process is seen to increase the size dispersion of the nanocrystals slightly, but the general size and the shape are preserved. XRD diffractograms of as-synthesized and ligand-stripped 5 nm (e) and 8 nm (f) nanocrystals showing that the desired spinel structure is present both before and after ligand-stripping.

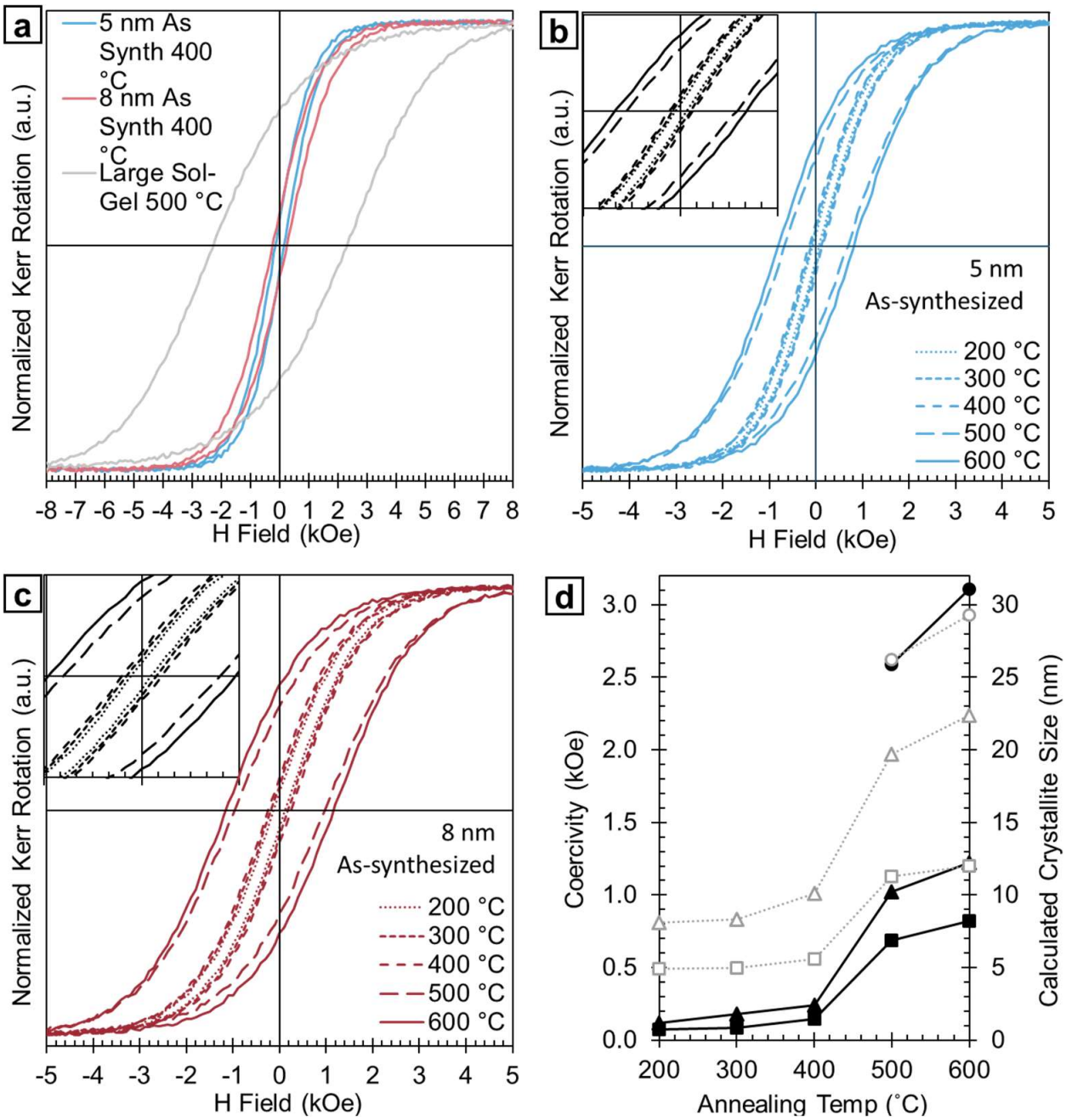

Figure 6.4: Magnetic characterization of thin films made from CFO nanocrystals. (a) Room temperature, in-plane magnetic hysteresis loops of films annealed at 400 °C made from as-synthesized 5 nm nanocrystals and 8 nm nanocrystals, including data for a dense sol-gel derived film annealed at 500 °C for comparison. The 5 nm nanocrystals have the smallest coercivity, followed closely by the 8 nm nanocrystals. In both cases, the nanocrystal-based films have significantly smaller coercivities than the sol-gel-derived films. Magnetic hysteresis loops for films made from as synthesized 5 nm (b) and 8 nm (c) nanocrystals annealed at various temperatures. Higher annealing temperature correlates to increased coercivity. (d) Measured coercivity and crystallite size calculated from the Scherrer equation as a function of annealing temperature.

For comparison, the 5 nm nanocrystal film had a coercivity of 50 Oe as measured by SQUID magnetometry.

As expected, there is very little difference between the as-synthesized and ligand-stripped nanocrystals. This suggests that despite some observed change in size dispersity as shown in figure 6.3, the ligand-stripping process has a minimal impact on the nanocrystal properties which makes it useful tool for nanocrystal processing in various situations. It also suggests that in these films, the contribution of the surface to the magnetization is minimal.

The effect of annealing temperature on the magnetic properties was also investigated and the resulting hysteresis loops are shown in figure 6.4b–c. The data shown is from the films of as-synthesized nanocrystals, however; in each case, the ligand-free analogs were also investigated and the differences between them remained minimal. The films were annealed between 200 °C and 600 °C, and for both smaller and larger nanocrystals, the coercivity increased with increasing annealing temperature. This is attributed to increased grain growth due to nanocrystal sintering at higher temperatures.

In order to characterize the effect of annealing temperature on domain size, XRD was done on all of the films and the average crystallite size was calculated using the Scherrer equation (6.1) as described above. The calculated crystallite sizes and observed coercivity are plotted in figure 6.4d as a function of annealing temperature for both sol-gel and nanocrystal-based films. For all films the calculated crystallite size and coercivity show similar trends. This is particularly noticeable in the nanocrystal-based films between 400 °C and 500 °C where there is a large jump in both values. This suggests that in that temperature range there is a point at which the nanocrystal sintering or melting occurs more rapidly. This correlation supports our conclusion that crystallite size is the primary factor in determining the coercivity.

Both inducing porosity in sol-gel-derived films and using nanocrystals to make thin films have been shown to lower the coercivity of CFO thin films. In order to further tune the magnetic properties, porous, nanocrystal-based films were fabricated. It is worth noting that ligand-stripping is required for the block copolymer templating process used here. Top-view SEM images shown in

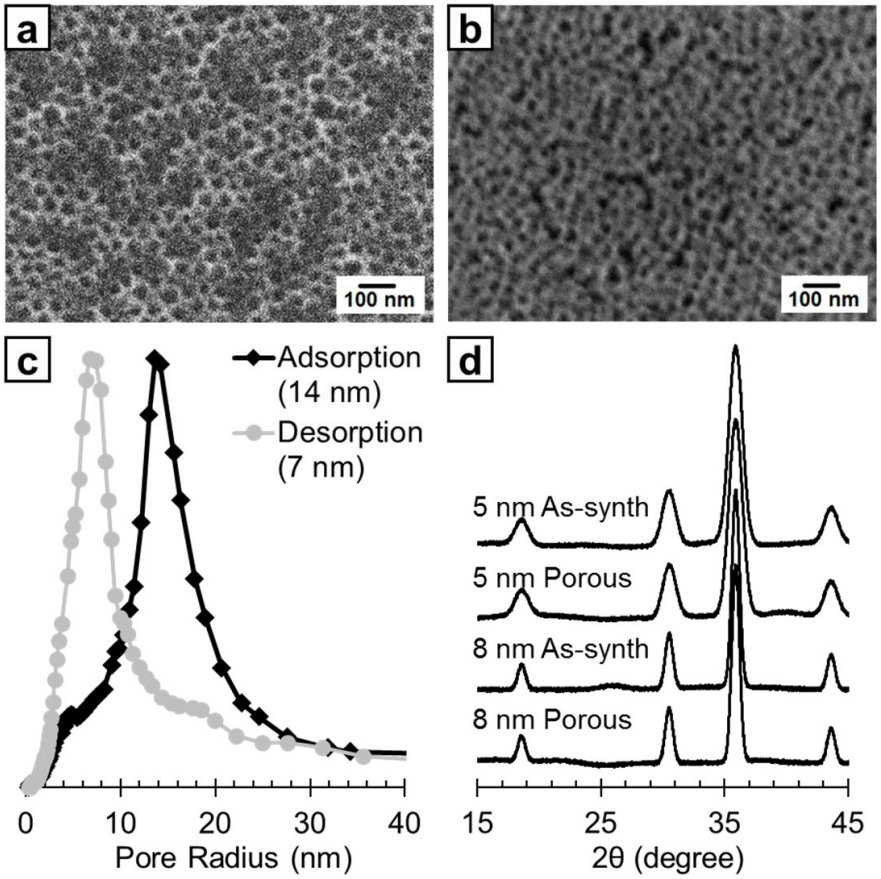

Figure 6.5: Top-view SEM images of porous CFO films made from 5 nm (a) and 8 nm (b) nanocrystals. (c) The pore radius distribution of a representative templated film made from 5 nm nanocrystals annealed at 400 °C showing a pore size of 14 nm and neck size of 7 nm. (d) X-ray diffractograms of both dense and porous nanocrystal-based films confirming the spinel structure.

figure 6.5 show the pore structure in films made from 5 nm nanocrystals (a) and 8 nm nanocrystals (b). The pores in the nanocrystal-based films are larger than their sol-gel counterparts because a different, larger block copolymer was used for the nanocrystals due to the difference in solvent requirements for the two precursors. As for the sol-gel films, the templating polymer was removed via thermal annealing, as discussed below.

To investigate the open porosity of the post-annealed films, ellipsometric porosimetry was performed and the results for an example film based on 5 nm nanocrystals and annealed at 400 °C, are presented in figure 6.5c. The porosimetry confirms that the templated nanocrystal-based films have an open pore structure with an overall porosity of 38%, an average pore radius of 14 nm and an average neck radius of 7 nm, which corresponds well to the top-view SEM images shown in figure 6.5a. XRD was again employed to determine that the spinel structure was indeed retained during the templating process, and the resulting diffractograms are in figure 6.5d.

Figure 6.6 shows magnetic hysteresis loops of both dense and porous nanocrystal-based films annealed at 400 °C. In the case of these nanocrystal-based films, dense films refer to films with no polymer template, and therefore no mesopores, but these films do have some nanoporosity due to the limitation on spherical packing of the nanocrystals. As described above, the addition of mesopores to sol-gel-derived films serves to limit the crystalline, and therefore magnetic, domain size, as does making nanocrystal-based films. However, if the coercivity were solely dependent on physical domain size, we would expect to see no change due to porosity in the nanocrystal-based samples, which is not the case. There is an observable decrease in coercivity of ~ 10 Oe due to porosity for 5 nm–nanocrystal–based films and ~ 40 Oe in 8 nm–nanocyrstal–based films. This suggests that there is a secondary mechanism by which pores decrease magnetic coercivity, which we believe is the limiting of dipolar interactions in porous films. Spins near a pore have fewer neighboring spins with which to dipole couple, which can allow them to more easily align with the external field hence lowering the observed coercivity.

In addition to characterizing the static magnetic properties, ferromagnetic resonance (FMR) measurements were used to explore the dynamic behavior. FMR is an absorptive phenomenon in

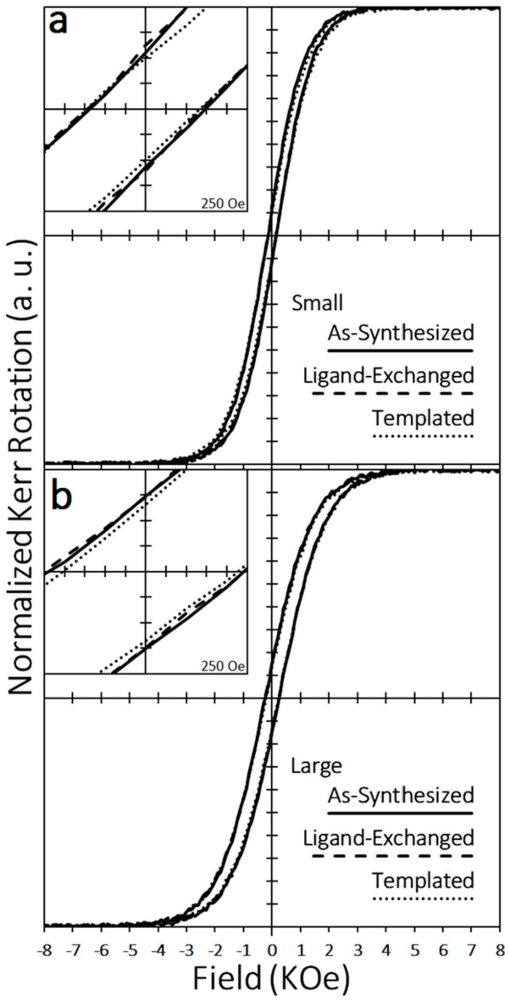

Figure 6.6: Room temperature, in-plane magnetic hysteresis loops of both dense and mesoporous thin films annealed at 400 °C from 5 nm nanocrystals (a), 8 nm nanocrystals (b).

which a magnetic material absorbs microwave radiation causing the magnetic spins to precess around the axis of an applied bias field. It is well described by the Landau–Lifshitz–Gilbert (LLG) model of precessional motion.[66] Within this model, high frequency losses are taken into account by the Gilbert damping coefficient (α). Damping is when a precessing spin stops its precession and returns to static alignment with the applied field. The peak-to-peak linewidth (ΔH_{pp}) is a common figure of merit because it is related to the Gilbert damping coefficient through the following relation:

$$\alpha = \frac{\gamma \Delta H_{\mathrm{pp}}}{4\pi f'}, \tag{6.3}$$

where γ is the gyromagnetic ratio, which is 2.8 GHz kOe^{-1}, and f' is the measurement frequency. For most applications, losses should be minimized, so low values for α, and therefore low ΔH_{pp}, are desired.

Here, despite the large range of observed coercivities, almost all of the films showed identical room temperature FMR. In these cases the ΔH_{pp} was found to be 39 G, which corresponds to $\alpha = 0.0009$ and the center field $H_0 = 3519$ G. This suggests that while the static properties such as coercivity and remanence are dependent on domain-level structure, the dynamic behavior is more a function of the material or atomic-level composition.

The only films that did not show identical FMR were the sol-gel-derived films and the 8 nm–nanocrystal–based films annealed at or above 500 °C, which showed no resonant behavior at the measurement frequency (X-band, 9.7 GHz). Those films have the highest coercivities, which is likely the cause of the lack of resonance. A requirement for FMR is that the sample is magnetically saturated such that all of the spins are aligned with the applied bias field. In the samples with high coercive fields, it is probable that the bias field at which FMR occurs in CFO at 9.7 GHz was insufficiently high to fully saturate the sample thereby eliminating the resonance. It is for this reason that CFO has not been widely investigated for microwave applications where strong FMR and low losses are desired.

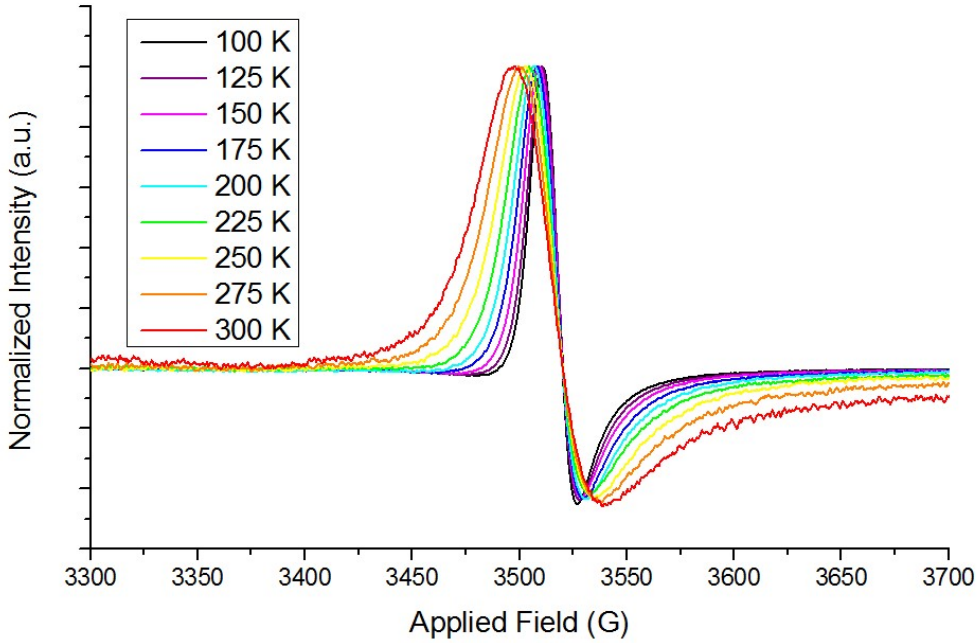

Figure 6.7: Temperature-dependent FMR spectra of a representative film made from as-synthesized 5 nm CFO nanocrystals annealed at 400 °C. The peak to peak linewidth (ΔH_{pp}) decreases with decreasing temperature, consistent with a ferromagnetic material.

However, the lower coercivities achieved in the nanocrystal-based films ensure that the spins are saturated thereby allowing FMR. Temperature-dependent FMR spectra, or the derivative of microwave power absorption spectra, of an example film made using 5 nm nanocrystals is presented in figure 6.7. The intensities were normalized for easier comparison, although the intensity decreased with increasing temperature which is why the data at higher temperatures appears noisier. At room temperature, the linewidth is 39 G and $\alpha = 0.0009$, which is fairly low for a ferrite material at such a high frequency. Commercially produced ferrites such as lithium ferrite and nickel zinc ferrite have damping coefficients of 0.008 and 0.009, respectively.[31] This suggests that nanostructured CFO is an intrinsically low-loss material which makes it promising for use in microwave applications.

The temperature dependent FMR measurements reveal that linewidth increases linearly with temperature, which is consistent with a ferromagnetic material. It has been shown that linewidths increase with increasing temperature until the blocking temperature and then decrease with

further increasing temperature in the superparamagnetic regime.[59,67,68] The asymmetry between the positive and negative peaks of the spectra is commonly found in solid magnetic materials and is due to magnetic anisotropies and dipolar interactions within the film. This also suggests that the film is ferromagnetic in this temperature range. If the sample were above the Curie temperature and in a paramagnetic state, the magnetic anisotropies would be zero and the resulting spectra would be perfectly isotropic.[69] It is also worth noting that at higher temperatures, the absorption intensity does not return to zero immediately. This is due to non-resonant microwave absorption and has been observed both in CFO and other ferrite materials.[21,28]

Conclusion

Here we have presented two methods for tuning the static magnetic properties of cobalt ferrite thin films: making mesoporous films and making nanocrystal-based films. By controlling the film precursor, porosity and annealing temperature, the coercivity was successfully tuned from 3108 Oe down to 70 Oe. We postulate that the major mechanism for reducing the coercivity in these samples was limiting crystalline and magnetic domain size through nanostructuring, while decreasing dipolar interactions played a secondary role. Furthermore, we have shown that despite the large range of attainable coercivities, the dynamic magnetic properties remain largely the same between samples suggesting that the static magnetic properties arise from domain level structure while the high frequency behavior is dominated by atomic level structure.

Acknowledgments

This work was supported by the NSF under Cooperative Agreement Award EEC-1160504. The authors acknowledge the use of instruments at the Electron Imaging Center for NanoMachines supported by NIH (1S10RR23057 to ZHZ) and CNSI at UCLA. The X-ray diffraction studies presented in this manuscript were carried out at the Stanford Synchrotron Radiation Lightsource.

Use of the Stanford Synchrotron Radiation Lightsource, SLAC National Accelerator Laboratory, is supported by the U.S. Department of Energy, Office of Science, Office of Basic Energy Sciences, under Contract DE-AC02-76SF00515. The authors would also like to thank Professor Kang Wang, Distinguished Professor and Raytheon Chair in Electrical Engineering, UCLA, for use of his MOKE spectrometer for static magnetic property characterization.

References

(1) Krishna Surendra, M.; Annapoorani, S.; Ansar, E. B.; Harikrishna Varma, P. R.; Ramachandra Rao, M. S. *Journal of Nanoparticle Research* **Dec. 2014**, *16*, 2773.

(2) Kamali, S.; Pouryazdan, M.; Ghafari, M.; Itou, M.; Rahman, M.; Stroeve, P.; Hahn, H.; Sakurai, Y. *Journal of Magnetism and Magnetic Materials* **Apr. 2016**, *404*, 143–147.

(3) Andreu, I.; Natividad, E.; Ravagli, C.; Castro, M.; Baldi, G. *RSC Advances* **July 2014**, *4*, 28968.

(4) Chand, M.; Kumar, S.; Shankar, A.; Porwal, R.; Pant, R. *Journal of Non-Crystalline Solids* **Feb. 2013**, *361*, 38–42.

(5) Lisjak, D.; Jenus, P.; Drofenik, M. *IEEE Transactions on Magnetics* **Nov. 2012**, *48*, 3303–3306.

(6) Nabeel Rashin, M.; Hemalatha, J. *Ultrasonics* **Mar. 2014**, *54*, 834–840.

(7) Lacroix, L.-M.; Malaki, R. B.; Carrey, J.; Lachaize, S.; Respaud, M.; Goya, G. F.; Chaudret, B. *Journal of Applied Physics* **2009**, *105*, 023911.

(8) Hu, W.; Zou, L.; Chen, R.; Xie, W.; Chen, X.; Qin, N.; Li, S.; Yang, G.; Bao, D. *Applied Physics Letters* **Apr. 2014**, *104*, 143502.

(9) Jiang, C.; Wu, L.; Wei, W.; Dong, C.; Yao, J. *Nanoscale Research Letters* **2014**, *9*, 584.

(10) Matzen, S.; Moussy, J.-B.; Mattana, R.; Bouzehouane, K.; Deranlot, C.; Petroff, F. *Applied Physics Letters* **2012**, *101*, 042409.

(11) Ramos, A. V.; Guittet, M.-J.; Moussy, J.-B.; Mattana, R.; Deranlot, C.; Petroff, F.; Gatel, C. *Applied Physics Letters* **July 2007**, *91*, 122107.

(12) Takahashi, Y. K.; Kasai, S.; Furubayashi, T.; Mitani, S.; Inomata, K.; Hono, K. *Applied Physics Letters* **2010**, *96*, 072512.

(13) Sanpo, N.; Berndt, C. C.; Wen, C.; Wang, J. *Acta Biomaterialia* **Mar. 2013**, *9*, 5830–5837.

(14) Amiri, S.; Shokrollahi, H. *Materials Science and Engineering: C* **Jan. 2013**, *33*, 1–8.

(15) Berensmeier, S. *Applied Microbiology and Biotechnology* **Nov. 2006**, *73*, 495–504.

(16) Joshi, H. M.; Lin, Y. P.; Aslam, M.; Prasad, P. V.; Schultz-Sikma, E. A.; Edelman, R.; Meade, T.; Dravid, V. P. *The Journal of Physical Chemistry C* **Oct. 2009**, *113*, 17761–17767.

(17) Pershina, A. G.; Sazonov, A. E.; Ogorodova, L. M. *Russian Journal of Bioorganic Chemistry* **Sept. 2009**, *35*, 607–613.

(18) Yoo, D.; Lee, J.-H.; Shin, T.-H.; Cheon, J. *Accounts of Chemical Research* **Oct. 2011**, *44*, 863–874.

(19) Hannour, A.; Vincent, D.; Kahlouche, F.; Tchangoulian, A.; Neveu, S.; Dupuis, V. *Journal of Magnetism and Magnetic Materials* **Mar. 2014**, *353*, 29–33.

(20) Li, G.-M.; Wang, L.-C.; Xu, Y. *Chinese Physics B* **Aug. 2014**, *23*, 088105.

(21) Mata-Zamora, M. E.; Montiel, H.; Alvarez, G.; Saniger, J. M.; Zamorano, R.; Valenzuela, R. *Journal of Magnetism and Magnetic Materials* **Sept. 2007**, *316*, e532–e534.

(22) Sharma, D.; Khare, N. In, 2015, p 080010.

(23) Popov, M. A.; Zavislyak, I. V.; Murthy, D. V. B.; Srinivasan, G. *Microwave and Optical Technology Letters* **Apr. 2014**, *56*, 814–818.

(24) Lagarkov, A. N.; Rozanov, K. N. *Journal of Magnetism and Magnetic Materials* **July 2009**, *321*, 2082–2092.

(25) Schloemann, E. *Journal of Magnetism and Magnetic Materials* **Feb. 2000**, *209*, 15–20.

(26) Özgür, Ü.; Alivov, Y.; Morkoç, H. *Journal of Materials Science: Materials in Electronics* **Sept. 2009**, *20*, 789–834.

(27) Popov, M. A.; Murthy, D. V. B.; Zavislyak, I. V.; Srinivasan, G. *Electronics Letters* **2012**, *48*, 98.

(28) Fannin, P. C.; Marin, C. N.; Malaescu, I.; Stefu, N.; Vlazan, P.; Novaconi, S.; Sfirloaga, P.; Popescu, S.; Couper, C. *Materials & Design* **Mar. 2011**, *32*, 1600–1604.

(29) Yin, J.; Ding, J.; Liu, B.; Miao, X.; Chen, J. *Applied Physics Letters* **2006**, *88*, 162502.

(30) Dhakal, T.; Mukherjee, D.; Hyde, R.; Mukherjee, P.; Phan, M. H.; Srikanth, H.; Witanachchi, S. *Journal of Applied Physics* **2010**, *107*, 053914.

(31) Cadieu, F. J.; Rani, R.; Mendoza, W.; Peng, B.; Shaheen, S. A.; Hurben, M. J.; Patton, C. E. *Journal of Applied Physics* **1997**, *81*, 4801.

(32) Verma, A.; Alam, M.; Chatterjee, R.; Goel, T.; Mendiratta, R. *Journal of Magnetism and Magnetic Materials* **May 2006**, *300*, 500–505.

(33) Harris, V. G.; Geiler, A.; Chen, Y.; Yoon, S. D.; Wu, M.; Yang, A.; Chen, Z.; He, P.; Parimi, P. V.; Zuo, X.; Patton, C. E.; Abe, M.; Acher, O.; Vittoria, C. *Journal of Magnetism and Magnetic Materials* **July 2009**, *321*, 2035–2047.

(34) Quickel, T. E.; Le, V. H.; Brezesinski, T.; Tolbert, S. H. *Nano letters* **Aug. 2010**, *10*, 2982–8.

(35) Song, Q.; Zhang, Z. J. *Journal of the American Chemical Society* **May 2004**, *126*, 6164–6168.

(36) Peddis, D.; Orrù, F.; Ardu, A.; Cannas, C.; Musinu, A.; Piccaluga, G. *Chemistry of Materials* **Mar. 2012**, *24*, 1062–1071.

(37) Dong, A.; Ye, X.; Chen, J.; Kang, Y.; Gordon, T.; Kikkawa, J. M.; Murray, C. B. *Journal of the American Chemical Society* **Feb. 2011**, *133*, 998–1006.

(38) Rosen, E. L.; Buonsanti, R.; Llordes, A.; Sawvel, A. M.; Milliron, D. J.; Helms, B. A. *Angewandte Chemie International Edition* **Jan. 2012**, *51*, 684–689.

(39) Jing, P.; Du, J.; Jin, C.; Wang, J.; Pan, L.; Li, J.; Liu, Q. *Journal of Materials Science* **Jan. 2016**, *51*, 885–892.

(40) Kao, J.; Bai, P.; Lucas, J. M.; Alivisatos, A. P.; Xu, T. *Journal of the American Chemical Society* **Feb. 2013**, *135*, 1680–1683.

(41) Innocenzi, P.; Malfatti, L. *Chemical Society Reviews* **2013**, *42*, 4198.

(42) Boissiere, C.; Grosso, D.; Lepoutre, S.; Nicole, L.; Bruneau, A. B.; Sanchez, C. *Langmuir* **Dec. 2005**, *21*, 12362–12371.

(43) Hamd, W.; Cobo, S.; Fize, J.; Baldinozzi, G.; Schwartz, W.; Reymermier, M.; Pereira, A.; Fontecave, M.; Artero, V.; Laberty-Robert, C.; Sanchez, C. *Physical Chemistry Chemical Physics* **2012**, *14*, 13224.

(44) Rauda, I. E.; Augustyn, V.; Dunn, B.; Tolbert, S. H. *Accounts of Chemical Research* **May 2013**, *46*, 1113–1124.

(45) Ortel, E.; Reier, T.; Strasser, P.; Kraehnert, R. *Chemistry of Materials* **July 2011**, *23*, 3201–3209.

(46) Quickel, T. E.; Schelhas, L. T.; Farrell, R. A.; Petkov, N.; Le, V. H.; Tolbert, S. H. *Nature Communications* **2015**, *6*, 6562.

(47) Fang, J.; Kang, C. B.; Huang, Y.; Tolbert, S. H.; Pilon, L. *The Journal of Physical Chemistry C* **June 2012**, *116*, 12926–12933.

(48) Hartmann, P.; Brezesinski, T.; Sann, J.; Lotnyk, A.; Eufinger, J.-P.; Kienle, L.; Janek, J. *ACS Nano* **Apr. 2013**, *7*, 2999–3013.

(49) Brezesinski, T.; Wang, J.; Tolbert, S. H.; Dunn, B. *Nature materials* **Feb. 2010**, *9*, 146–51.

(50) Detsi, E.; Cook, J. B.; Lesel, B. K.; Turner, C. L.; Liang, Y.-L.; Robbennolt, S.; Tolbert, S. H. *Energy Environ. Sci.* **2016**, *9*, 540–549.

(51) Rosen, J.; Hutchings, G. S.; Jiao, F. *Journal of the American Chemical Society* **Mar. 2013**, *135*, 4516–4521.

(52) Brezesinski, K.; Wang, J.; Haetge, J.; Reitz, C.; Steinmueller, S. O.; Tolbert, S. H.; Smarsly, B. M.; Dunn, B.; Brezesinski, T. *Journal of the American Chemical Society* **May 2010**, *132*, 6982–6990.

(53) Rauda, I. E.; Buonsanti, R.; Saldarriaga-Lopez, L. C.; Benjauthrit, K.; Schelhas, L. T.; Stefik, M.; Augustyn, V.; Ko, J.; Dunn, B.; Wiesner, U.; Milliron, D. J.; Tolbert, S. H. *ACS Nano* **2012**, *6*, 6386–6399.

(54) Hsueh, H.-Y.; Yao, C.-T.; Ho, R.-M. *Chem. Soc. Rev.* **2015**, *44*, 1974–2018.

(55) Chen, C.-C.; Herhold, A. B.; Johnson, C. S.; Alivisatos, A. P. *Science* **Apr. 1997**, *276*, 398–401.

(56) Shafi, K. V. P. M.; Gedanken, A.; Prozorov, R.; Balogh, J. *Chemistry of Materials* **Nov. 1998**, *10*, 3445–3450.

(57) Chinnasamy, C. N.; Jeyadevan, B.; Shinoda, K.; Tohji, K.; Djayaprawira, D. J.; Takahashi, M.; Joseyphus, R. J.; Narayanasamy, A. *Applied Physics Letters* **2003**, *83*, 2862.

(58) Yin, Y.; Alivisatos, A. P. *Nature* **Sept. 2005**, *437*, 664–670.

(59) Cao, X.; Gu, L. *Nanotechnology* **Feb. 2005**, *16*, 180–185.

(60) Lee, D. C.; Smith, D. K.; Heitsch, A. T.; Korgel, B. A. *Annual Reports Section "C" (Physical Chemistry)* **2007**, *103*, 351.

(61) Verma, S.; Pravarthana, D. *Langmuir* **Nov. 2011**, *27*, 13189–13197.

(62) López-Ortega, A.; Lottini, E.; de Julián Fernández, C.; Sangregorio, C.; Fernández, C. d. J.; Sangregorio, C.; de Julián Fernández, C.; Sangregorio, C.; Fernández, C. d. J.; Sangregorio, C. *Chemistry of Materials* **June 2015**, *27*, 150506115500009.

(63) Geng, B.; Ma, Y.; Xu, S.; Xu, Y.; Sun, X.; Dai, Z.; Zheng, G. *Ceramics International* **Jan. 2016**, *42*, 317–324.

(64) Haynes, J. M. *Matériaux et Constructions* **May 1973**, *6*, 209–213.

(65) Stoner, E. C.; Wohlfarth, E. P. *Philosophical Transactions of the Royal Society A: Mathematical, Physical and Engineering Sciences* **May 1948**, *240*, 599–642.

(66) Gilbert, T. *IEEE Transactions on Magnetics* **Nov. 2004**, *40*, 3443–3449.

(67) Hochepied, J.; Pileni, M. *Journal of Magnetism and Magnetic Materials* **May 2001**, *231*, 45–52.

(68) Singh, J. P.; Dixit, G.; Srivastava, R. C.; Kumar, H.; Agrawal, H. M.; Chand, P. *Bulletin of Materials Science* **Aug. 2013**, *36*, 751–754.

(69) Flores-Arias, Y.; Vázquez-Victorio, G.; Ortega-Zempoalteca, R.; Acevedo-Salas, U.; Ammar, S.; Valenzuela, R. *Journal of Applied Physics* **May 2015**, *117*, 17A503.

Chapter 7

Conclusion

Here we have explored the synthesis, properties, and applications of solution-processed PZT and CFO. As multiferroic materials, each of these materials have strain that is coupled to their respective electric or magnetic polarizations. Solution processing and nanostructuring have aided in our understanding of these materials and even improved their properties.

In chapter 6, we have shown that control over nanoarchitecture strongly influences static magnetic properties of CFO. The magnetic domain size is limited by the grain size, and as the grain size is decreased, either by incorporating mesopores into the thin film or by limiting the size of nanocrystals, the coercivity of the CFO film correspondingly decreases. Control over these static properties come with no loss to the dynamic magnetic properties, as the films all maintained comparable frequency-dependent magnetic responses.

In chapter 5, another size-dependent effect is explored. As PZT film thicknesses increase to the order of 10^{-7} m, rotations and reorientations of ferroelectric domains become more likely. A new model of PZT films was developed, one that accounts for the energy loss through domain reorientation. A sufficiently thick PZT film was produced by solution processing to confirm the predictions of this model.

The synthesis of PZT films using sol-gel processing is more thoroughly explored in chapter 4. A number of parameters is accessible to alter the atom-scale and the nanoscale structure of PZT thin films. Films of arbitrary thickness may be attained by using an iterative spin coating method,

which is used with quick, relatively high-temperature heating process and tends to produce ⟨100⟩-oriented films. Films with tunable nanoarchitecture are fabricated by a block copolymer templated solution, which requires a long heating process at relatively low temperatures and tends to produce ⟨111⟩-oriented films. These films feature an interconnected network of pores and are ideal for use in strain-coupled magnetoelectric composites.

Finally, CFO and PZT are combined in chapters 2 and 3. A mesoporous CFO framework is conformally filled by PZT using ALD, creating a three-dimensional interconnected network of both materials that are intimately coupled to each other. By controlling the thickness of the deposited PZT film, we can tune the final porosity of the composite film. An external electric field was then applied to the composite, which strained the PZT layer. The films with the greatest porosity also saw the greatest strain transfer from the PZT to the CFO, which highlighted the role of pore flexion in accommodating strains in the material. The CFO strains led to a change in the overall saturation magnetization of the films, leaving us with a new control parameter—porosity—in the fabrication of strain-coupled multiferroics.

Thus we see that sol-gel processing, in addition to being a cost-effective and scalable method to produce multiferroic thin film oxides, also allows us to control the strain and the electromagnetic properties of these films.

Appendix A

Supplementary Material

Synthetic methods

Cobalt ferrite synthesis

A typical CFO solution stoichiometrically contains 0.09 g of CFO. The ideal solution is composed of 0.3099 g of $Fe(NO_3)_3 \cdot 9\,H_2O$ and 0.1116 g of $Co(NO_3)_3 \cdot 6\,H_2O$ dissolved in 1 ml of 2-methoxyethanol, 1 ml of ethanol, and 0.02 ml of glacial acetic acid. Mesoporous CFO is ideally templated by 35 mg of PBd-*b*-PEO or 40 mg of PEP-PEO, dissolved in 1 ml of ethanol.

CFO may be crystallized at a range of temperatures varying from 500 °C to 700 °C, but films are typically crystallized at 550 °C. In all cases, the temperature is ramped at a rate of 10 °C min^{-1}. The films should soak for no more than 5 min to minimize unwanted grain growth.

Other details have been given previously.[1–3]

Lead zirconate titanate

Detailed information for PZT syntheses have been given in chapter 4.

Electrical Poling

Before proceeding, read, sign, and observe all safety regulations given in the "Electrical Poling System" SOP of the Tolbert lab.

1. Make sure that both the voltage source and the amplifier are both off and unplugged.

2. Place the sample inside the poling chamber. In the case of particularly leaky samples, use a polyvinylidene chloride spacer to prevent shorting. The actual field applied to the sample may be calculated by treating the sample and the spacer as two capacitors in series.

3. Make connections from the voltage source to the amplifier and to the voltmeter. Do not leave any exposed contacts. If the connection is outside the instrument casing, cover the connection with heat shrink tubing or another insulating shield.

4. Turn on the voltage source, then the amplifier. Set instrument at the minimal voltage (less than 0.01 V). Then connect the amplifier to the poling chamber. This is necessary because the act of turning on the instrument introduces undesirable voltage spikes to the sample if already connected.

5. Slowly increase voltage until the desired field is achieved.

6. Reverse all the steps when poling is finished.

Analysis of X-ray diffraction by PeakFit

XRD peaks were fit using PeakFit v4.11. PeakFit offers three methods to automatically fit peaks. However, since much of the data obtained from SSRL beamline 7-2 contain either only one peak or convoluted peaks, those three methods are largely irrelevant. PeakFit also offers a baseline subtraction function, but the "AutoFit and Subtract Baseline" button will not take this baseline fitting into account when trying to fit the peaks. Therefore, it is recommended to use baseline

fitting only to determine which method of baseline subtraction to choose. The actual baseline subtraction should be performed as part of one of the AutoFit functions.

A Gaussian profile reflects a relatively sharp distribution, whereas a Lorentzian profile reflects homogeneous broadening. Because XRD has both well-defined Bragg conditions and a number of various scattering functions, both Gaussian and Lorentzian functions should be used to fit XRD peaks. PeakFit offers both Voigt (a convolution of both the Gaussian and Lorentzian profiles) and pseudo-Voigt (a linear combination of both profiles, labeled "Gauss+Lor") functions. Of particular recommendation is the "Gauss+Lor Area" function, which allows specific control over the full-width at half maximum as parameter a_2, useful to fit peaks from samples of a known crystallite size. Additionally, the "Set Common Parameters" button allows the widths of peaks from the same sample to be constrained. Alternately, right-clicking on each peak allows both sharing and constraining of parameters between individual peaks.

Note that the cursor often fails to detect the individual peak parameter window. To be able to click on this window, move the cursor away from the graph areas, then back onto the window.

It is recommended to maximize the number of iterations in "Modify Peak Fit Preferences" to obtain the best fits. Furthermore, running the fit more than once helps to get increasingly better fits. When reporting the fitted data, it is useful to note both the r^2 coefficient of the fit, as well as the standard error of the peak position.

References

(1) Quickel, T. E.; Le, V. H.; Brezesinski, T.; Tolbert, S. H. *Nano letters* **Aug. 2010**, *10*, 2982–8.

(2) Schelhas, L. T. Using Solution Phase Self-Assembly to Control the Properties of Magnetic and Magnetoelectric Nanostructures., Ph.D. Thesis, University of California, Los Angeles, 2013.

(3) Chien, D.; Buditama, A. N.; Schelhas, L. T.; Kang, H. Y.; Robbennolt, S.; Chang, J. P.; Tolbert, S. H. *Applied Physics Letters* **2016**, *109*, 112904.